# Evaluation of Gritting Strategies for High Angle of Attack Using Wind Tunnel and Flight Test Data for the F/A-18

Robert M. Hall, Gary E. Erickson, and Charles H. Fox, Jr.
Langley Research Center, Hampton, Virginia

Daniel W. Banks and David F. Fisher
Dryden Flight Research Center, Edwards, California

May 1998

Summary

A subsonic study of high-angle-of-attack gritting strategies was undertaken with a 0.06-scale model of the F/A-18, which was assumed to be typical of airplanes with smooth-sided forebodies. This study was conducted in the Langley 7- by 10-Foot High-Speed Tunnel and was intended to more accurately simulate flight boundary layer characteristics on the model in the wind tunnel than would be possible by using classical, low-angle-of-attack gritting on the fuselage. Six-component force and moment data were taken with an internally mounted strain-gauge balance, while pressure data were acquired by using electronically scanned pressure transducers. Data were taken at zero sideslip over an angle-of-attack range from 0° to 40° and, at selected angles of attack, over sideslip angles from −10° to 10°. Free-stream Mach number was fixed at 0.30, which resulted in a Reynolds number, based on mean aerodynamic chord, of 1.4×10^6. Pressure data measured over the forebody and leading-edge extensions are compared to similar pressure data taken by a related NASA flight research program by using a specially instrumented F/A-18, the High-Alpha Research Vehicle (HARV). Preliminary guidelines for high-angle-of-attack gritting strategies are given.

Introduction

During aircraft development programs, it is not always possible to do complementary studies to understand the subtleties of the high-angle-of-attack flow physics or to address test technique questions. Consequently, an integral aspect of NASA's High-Angle-of-Attack Technology Program (HATP) has been to increase understanding of the flow physics and to develop testing techniques. Another important component of HATP has been the inclusion of a highly instrumented flight vehicle, the High-Alpha Research Vehicle (HARV). Having flight data available provides benchmark information for evaluating either wind tunnel data or computational data.

The present test of a 0.06-scale model of the F/A-18 was part of the HATP program and was intended to further evaluate a testing technique, first described in reference 1, which uses high-angle-of-attack forebody gritting patterns. This type of gritting is designed to more accurately simulate in conventional wind tunnels the boundary layer characteristics and, thus, the pressure distributions associated with high Reynolds number flight conditions. This test was a cooperative effort involving the U.S. Navy, the McDonnell Douglas Corporation, and the National Aeronautics and Space Administration (NASA).

The data from the model test are interpreted in light of an earlier test at Ames Research Center conducted by Peter Lamont and reported in reference 2. This test used a generic, highly pressure-instrumented, 2.0-diameter ogive-cylinder model that was tested over a broad range of Reynolds numbers and to high angles of attack. By virtue of its similar planform to the F/A-18 forebody, these data are used to show probable Reynolds number trends for the F/A-18.

Symbols and Abbreviations

The longitudinal data are referred to the stability-axis system, and the lateral-directional data are referred to the body-axis system (fig. 1). The data are normalized by the usual quantities such as planform area, wingspan, and the wing mean aerodynamic chord. The moment reference center was located at 0.25 mean aerodynamic chord, which corresponds to fuselage station 458.6 in. at full scale and 27.51 in. for the 0.06-scale model. While dimensions will generally be given for the full-scale aircraft, the 0.06-scale dimensions are sometimes added in parentheses behind the full-scale values. Symbols used for the data of Lamont will be identified as such.

B	confined bubble region resulting from laminar separation
b	reference wing span, 37.42 ft
C_A	body-axis axial force coefficient, $\dfrac{\text{Axial force}}{q_\infty S}$
C_D	stability-axis drag coefficient, $\dfrac{\text{Drag}}{q_\infty S}$
C_L	stability-axis lift coefficient, $\dfrac{\text{Lift}}{q_\infty S}$
C_l	body-axis rolling-moment coefficient, $\dfrac{\text{Rolling moment}}{q_\infty S b}$
C_m	body-axis pitching-moment coefficient, $\dfrac{\text{Pitching moment}}{q_\infty S \bar{c}}$
C_N	body-axis normal force coefficient, $\dfrac{\text{Normal force}}{q_\infty S}$
$C_{N_{3.5D}}$	normal force coefficient for Lamont 2.0-diameter ogive cylinder as integrated from pressures from nose tip to 3.5 body diameters aft of tip
C_n	body-axis yawing-moment coefficient, $\dfrac{\text{Yawing moment}}{q_\infty S b}$
C_p	static pressure coefficient, $\dfrac{p - p_\infty}{q_\infty}$

C_Y	body-axis side force coefficient, $\dfrac{\text{Side force}}{q_\infty S}$
c.g.	center of gravity
$\bar{c}$	wing mean aerodynamic chord, 11.52 ft
D	diameter of base of ogive or effective diameter of F/A-18 forebody at FS 184, 4.11 ft
FS	fuselage station, in. (full scale)
HARV	High-Alpha Research Vehicle
HATP	High-Angle-of-Attack Technology Program
LEX	wing leading-edge extension
LP	laminar separation pattern
LS	position of laminar separation
l	streamwise distance, ft
M_∞	free-stream Mach number
NASA	National Aeronautics and Space Administration
p	local static pressure, lb/ft^2
p_∞	free-stream static pressure, lb/ft^2
q_∞	free-stream dynamic pressure, lb/ft^2
R	position of flow reattachment
$\text{Re}_{\bar{c}}$	Reynolds number based on $\bar{c}$
Re_D	Reynolds number based on D
Re_l	Reynolds number based on streamwise run length before reaching grit
S	reference wing area, 400 ft^2
SS	position of secondary separation
s	local semispan distance from LEX fuselage junction to leading edge, ft
TP	turbulent pattern
TRP	transitional separation pattern
TS	position of turbulent separation
x	distance along fuselage, ft
y	distance along LEX local semispan, ft
α	angle of attack, deg
β	angle of sideslip, deg
Δ	differences in variable between data sets
Δ_b	uncertainty in variable as determined during balance calibration
Δ_M	uncertainty in variable as stated by manufacturer
Δ_r	uncertainty in variable due to repeatability
δ	variable differenced from an average
θ	forebody cross-section angular location (0° is bottom dead center; positive is clockwise as seen from pilot's view), deg
7 × 10 HST	Langley 7- by 10-Foot High-Speed Tunnel (HST)

Hardware, Procedures, and Data Repeatability

Tunnel Description

The tests were conducted in the Langley 7- by 10-Foot High-Speed Tunnel (HST). This facility is a closed-circuit, subsonic atmospheric wind tunnel with a test section approximately 7 ft high by 10 ft wide. A complete description of the facility is given in reference 3. The forces and moments acting on the model were measured by using an internally mounted strain-gauge balance. The measured forces and moments, in turn, were used to determine corrections to α and β due to sting bending. Jet boundary and blockage corrections were also applied to the data based on references 4 and 5.

During the test, the angle-of-attack instrument, which was located aft of the model sting, was physically shifted during other instrumentation work. This unintentional shift changed the value of α at which many of the β-polars were taken. Consequently, a linear interpolation procedure has been applied, when appropriate, to facilitate both pressure and force and moment comparisons. This interpolation procedure will be discussed further in the section entitled "Angle-of-Attack Interpolation Procedure and Data Repeatability for Wind Tunnel."

A high-α, pitch-roll mechanism was used to take data at $\beta = 0°$ for $0° < \alpha \leq 40°$ and, at selected values of α, for $-10° \leq \beta \leq 10°$. The free-stream Mach number was fixed at 0.30 for the investigation reported herein, which resulted in a Reynolds number, based on mean aerodynamic chord, of 1.4×10^6.

Wind Tunnel Model Description

The geometry of the full-scale F/A-18 is illustrated in figure 2. An installation photograph of a 0.06-scale model in the 7- by 10-Foot HST is shown in figure 3. The model was tested with a Langley-manufactured, pressure-instrumented forward fuselage. The extent of this forward fuselage, which includes the forebody and the wing leading-edge extensions (LEX's), is highlighted in the figure by its black paint. A schematic showing the active pressure instrumentation for the present test is shown in figure 4 and illustrates the four active pressure rings on the forebody and the three pressure rows on the LEX's. The model was tested with 34° leading-edge-flap

2

deflections (leading edge down), 0° trailing-edge-flap deflections, −12° horizontal-tail deflection (leading edge down), 0° rudder deflection, single-place canopy, and wing-tip mounted missiles.

The internally mounted strain-gauge balance in the 0.06-scale model was an Mk XXIIIB Able balance, whose characteristics are shown in the following table:

Component	Load limit	Uncertainty in coefficient
Normal force	1200 lb	±0.019
Axial force	100 lb	±.0018
Pitching moment	3600 in-lb	±.0041
Rolling moment	800 in-lb	±.00031
Yawing moment	1500 in-lb	±.00065
Side force	600 lb	±.0090

These uncertainty values have been determined by using the value of S, the wing reference area, for the 0.06-scale model, the value of q_∞ for $M_\infty = 0.30$, and the balance uncertainty values for 95 percent confidence level, as established by a NASA calibration. No rigorous error analysis was performed during this experiment.

The uncertainty in the pressure coefficients due to the electronically scanned pressure transducers can be estimated from the stated manufacturer's value of uncertainty, which is 0.1 percent of full scale. The ranges of the electronically scanned pressure transducers varied from 5-lb modules for the forebody pressures to 15-lb modules for the LEX pressures. The only exception was that some of the pressures in the most aft forebody pressure row at FS 184 were routed to a 15-lb module. Based on the flow conditions of this experiment and the manufacturer's value of uncertainty, $\Delta_M C_p \sim \pm 0.006$ for most of the forebody pressures and $\Delta_M C_p \sim \pm 0.017$ for part of the forebody row at FS 184 and all of the LEX pressures. For the wind tunnel test, the values of pressure coefficients were averaged from 20 samples of pressures taken during 2 sec.

Angle-of-Attack Interpolation Procedure and Data Repeatability for Wind Tunnel

As mentioned, the angle-of-attack instrument, which was located aft of the model sting, was unintentionally shifted during the test. This incident changed the value of α at which most of the β-polars were taken. While interpolating data for the α-polars at zero sideslip is not a problem because data were typically taken every 2.0°, interpolating the sideslip data taken at discrete values of α was more problematic. For example, β-polar data were taken for the first nose-ring-only configuration at the expected nominal angles of attack of 28°, 32°, 36°, and 40°. However, with the shift in the instrument, all data

for the baseline, twin strip gritting pattern were taken with $\alpha = 29.4°$, 33.4°, 37.3°, and 41.3°. The other alternative, high-α gritting patterns, as well as a repeat run with the nose-ring-only data, were tested in sideslip at only two angles of attack due to time constraints. Those values of α were 37.3° and 41.3° because of the shift in α.

Another issue that required interpolation of both sets of wind tunnel data was that the data from the High-Alpha Research Vehicle (HARV) were generally available only at 5° intervals. Because the HARV data had the largest increments in α, the most accurate interpolation procedure was to interpolate all wind tunnel data to match the flight data.

To illustrate both tunnel repeatability and the interpolation procedure, data from the initial nose-ring-only configuration will be compared to the repeat nose-ring-only data. The first α-polar at $\beta = 0°$ comparison is shown in figure 5. The agreement between the two runs is indicative of repeatability after several days of running and after a number of grit pattern changes. The offset in α caused by the shift of ~1.4° in the instrument is apparent in the plot of C_L versus α.

The second comparison employs the interpolation procedure for the repeat data. This comparison is shown in figure 6. As intended, the values of α are now identical between the two data sets, and the differences due to repeatability are clearer. The interpolation procedure itself, as would be expected, causes some misleading differences for the predicted points at $\alpha = 0°$ and 20°. The misleading difference occurs because both these points are isolated, and an interpolation between close, neighboring points is not possible. That is, the predicted points for $\alpha = 0°$ and 20° are calculated from actual data at $\alpha = 1.2°$ and 21.4°. To get predicted data at $\alpha = 0°$, the actual data at $\alpha = 1.2°$ is extrapolated by using the slope between the actual data at $\alpha = 1.2°$ and 21.4°, which does not represent the actual slope in the neighborhood of $\alpha = 1.2°$ for C_D and C_m. Similarly, to get predicted data at $\alpha = 20.0°$, the slope between the actual data at $\alpha = 1.2°$ and 21.4° is again used with the same shortcoming, that does not represent the actual slope in the neighborhood of $\alpha = 20°$. Apart from these isolated points, the interpolation procedure appears adequate, and the repeatability between runs appears to be on the order of $\Delta_r C_L \sim \pm 0.02$, which is comparable to the nominal balance uncertainty of $\Delta_b C_L \sim \pm 0.016$. The other differences in C_D and C_m against C_L are all comparably small and may actually be due to the differences in C_L.

Repeatability for lateral-directional properties in sideslip are highlighted in figure 7 for the original and repeat nose-ring-only data without any interpolation. The difference in α between the two sets of data averages

about 0.9°. The comparison is refined in figure 8 by interpolating the repeat data β-polars at $\alpha = 37.4°$ and the just shown data at $\alpha = 41.3°$ to the original value of $\alpha = 40.4°$. Bringing the values of α into agreement by interpolation does improve the agreement, and the differences shown in figure 8 are representative of the repeatability when retesting a given gritting pattern.

The comparable repeatability in pressure coefficients between the original grit ring data and the interpolated values of the repeat grit ring are summarized in figure 9 for the forebody pressures and in figure 10 for the LEX pressure stations. The angles shown for the comparison are those for the original grit ring data, $\alpha = 20.2°$, $30.3°$, $35.4°$, $40.3°$ and at $\alpha \sim 40.3°$ for values of $\beta = 4°$ and $\beta = 8°$. It is also important to note that the interpolated repeat run data for C_p appear to be acceptable at $\alpha = 20.2°$. In fact, an alternative extrapolation method of linearly extrapolating to $\alpha = 20.2°$ from existing data at $\alpha = 21.4°$ and $25.4°$ gave virtually identical results. Consequently, the paper will present pressure comparisons between both wind tunnel sets of data and flight data at $\alpha = 20°$ because of the acceptable repeatability of these data in figures 9 and 10.

As shown in figure 9, the repeatability in the values of forebody C_p appears to be on the order of $\Delta_r C_p \sim \pm 0.05$ for most of the conditions and pressure ports. For the most extreme conditions displayed, that of $\alpha = 40°$ and $\beta = 8°$ (fig. 9(f)), however, there are larger differences at FS 184 in the leeward region $180° < \theta < 240°$, where differences become as large as $\Delta_r C_p \sim \pm 0.2$. The LEX pressure data in figure 10 suggest that differences are generally less than $\Delta_r C_p \sim \pm 0.1$.

Description of the HARV Flight Vehicle

The flight tests were conducted at Dryden Flight Research Center by using the F-18 HARV, as reported in references 6 and 7. The HARV, which is shown in figure 11, is a highly instrumented preproduction single-place F/A-18 airplane that was modified from the Navy preproduction spin test airplane. Its wing has both leading- and trailing-edge flaps that are scheduled with α and M_∞. At values of $\alpha \geq 26°$ and $M_\infty \leq 0.76$, the leading-edge-flap deflection angle goes to a maximum value of 34°, and the trailing-edge-flap deflection angle goes to 0°. The HARV was flown without stores and the wing-tip missile rails have been modified to carry camera pods and wing-tip air data probes. The data to be reported herein have been acquired since thrust vectoring was added to the airplane.

The pressure data were acquired by using onboard electronically scanned pressure transducers, and the data were transmitted to a ground station. The sample rate of

the pressure data acquisition was 10 samples/sec, and 10 samples were averaged to create the data point. Reference 7 contains additional details. The data reported herein were taken with the thrust-vectoring system installed on the aircraft.

Data Repeatability for Flight

The flight data itself will be expected to have some uncertainty due to repeatability. The first series of comparisons is for nominal values of $\alpha = 30°$, $35°$, and $40°$. While flight data for repeat points are not available for positive values of β and $\alpha = 40°$, they are available for negative values of β. Figure 12 illustrates the flight data repeatability comparisons for the four forebody stations, while figure 13 illustrates the comparable differences for the LEX pressure rows.

As shown in figure 12, the forebody comparisons for $\alpha = 30°$ display reasonable repeatability with $\Delta_r C_p \sim \pm 0.05$. While some of the points used to establish flight repeatability have differences in values of $Re_{\bar{c}}$, these differences are not expected to impact the assessment of repeatability for the following reasons. First, the values of $Re_{\bar{c}}$ are large. Second, comparable forebody data of Lamont, discussed in the next section, show no sensitivity to comparable changes in $Re_{\bar{c}}$. The data for $Re_{\bar{c}} = 10.3 \times 10^6$ at station FS 184 include only values for $\theta < 180°$ because of a malfunctioning pressure module. At a nominal value of $\alpha = 35°$, the differences in C_p are generally on the same order as for $\alpha = 30°$. For the forebody pressure coefficients at $\alpha = 40°$, $\Delta_r C_p \sim \pm 0.1$ in the attached flow regions near the sides of the body, where $\theta = 105°$ and $255°$ at FS 85, and in regions of the vortex suction peaks for FS 85. Similar differences are seen in the regions of vortex suction peaks $\theta = 160°$ and $200°$ at FS 142. The examples for sideslip conditions show differences generally on the order of half a symbol width, or ± 0.05.

A similar comparison sequence is found for the LEX pressures shown in figure 13. In this case, however, $\Delta_r C_p \sim \pm 0.1$ at $\alpha = 30°$. At higher values of α and for the nonzero values of β, differences in C_p for the rearward two pressure stations are as high as $\Delta_r C_p \sim \pm 0.2$.

Reynolds Number Effects on Smooth-Sided Forebodies

The value of Reynolds number at which a smooth body is tested determines, to a large extent, the strength of the vortices shed and, consequently, the magnitude of direct forces acting on the forebody (refs. 8 through 12). However, because of the potential of nonlinear vortical interactions between the forebody and subsequent vortices formed over the LEX's or main wings, Reynolds

4

number effects over the forebody may have significant impact on the longitudinal and lateral-directional stability of a full configuration (ref. 13).

As a first look at Reynolds number effects on smooth-sided forebodies, it is useful to review a work by Keener (ref. 14). This report contains oil flow, Schlieren, sublimation, and vapor screen photographs concerning various forebody shapes that were tested at Ames Research Center. One of the shapes most frequently tested was a tangent ogive mounted on a sting. The tangent ogive had a length-to-diameter ratio of 3.5 and is designated a "3.5-diameter" tangent ogive. An example of the type of oil flow information reported is shown in figure 14, where $\alpha = 40°$ and $\text{Re}_D = 0.80 \times 10^6$. The two views shown are 135° and 180° from the windward plane of symmetry.

As seen in figure 14, the oil flow pattern is quite complicated, and as explained by Keener, highlights three basic flow patterns in cross section—a laminar pattern (LP), a transitional pattern (TRP), and a turbulent pattern (TP). In figure 15 are three cross-sectional sketches that Keener used to present his model for the flow patterns associated with LP, TRP, and TP regimes. All three patterns illustrate flow reattachment (R) near the leeward plane of symmetry and subsequent secondary separation (SS). The TRP pattern is the most complicated. Primary laminar separation (LS) occurs, but the separated shear layer becomes turbulent and reattaches to the body, forming a confined bubble region (B). The flow subsequently undergoes turbulent separation (TS). Near the end of the ogive, where the local diameter is greatest, the effective Reynolds number is high enough for the boundary layer to have a transition before laminar separation can occur, which results in the TP pattern. Thus, no separation bubble forms, and the flow separates in a TS manner.

As will be developed, each of these flow topologies—LP, TRP, and TP—involve different separation locations and vortex strength progression in the streamwise direction. For this particular example, the length of the laminar region is very similar to that of the transitional region. All three regions are present and important in high-α flight of the full-scale vehicle.

During the late 1970's, Dr. Peter Lamont tested a pressure-instrumented, 2.0-diameter ogive-cylinder model in the Ames 12-Foot Pressure Wind Tunnel. Data from this entry were summarized in reference 2, as are details about model installation and instrumentation. However, the bulk of these pressure data has never been published. Some additional data from Lamont are presented in this paper, courtesy of Jerry Malcolm and Lewis Schiff, who shared the original data files with Langley Research Center.

Figure 16 compares the planform of the model used by Lamont to the forebody planform of the F/A-18. As seen in the figure, the planforms of these two bodies are similar, and one might expect their behavior to be related, given the success that researchers have had in correlating forebody planform and the onset of vortical flows (ref. 15) and vortex asymmetries (refs. 12 and 15). With regard to general trends, figure 17 displays the normal force coefficient $C_{N_{3.5D}}$, calculated by using the integrated pressure over the first 3.5 diameters of the Lamont body.

As seen in figure 17, the magnitude of the normal force, as expected, depends on both α and on the value of Reynolds number based on diameter Re_D. For $\text{Re}_D \sim 0.2 \times 10^6$, in which the basic flow topology is LP, separation occurs in such a fashion as to result in strong vortices. These strong vortices result in the large values of $C_{N_{3.5D}}$. In the intermediate range of Re_D from 0.4×10^6 to 1.2×10^6, the shedding along the aft portion of the body has ceased to be laminar, and the flow topology becomes TRP in nature. That is, over the aft portion of the body, laminar separation is followed by turbulent reattachment and subsequent turbulent separation. The strength of the vorticity being shed in these "transitional" regions is reduced and results in weaker vortices and reduced values of $C_{N_{3.5D}}$. As the Reynolds number continues to increase, the LP and TRP regions compress toward the nose, and the third TP (turbulent) topology appears and begins to increase its extent and influence. Because the resulting vorticity shed in the TP region is stronger than that in the TRP region, once again the values of $C_{N_{3.5D}}$ increase.

It is instructive to look at some of the individual pressure distributions of Lamont to better understand the details of the Reynolds number effects. For the current F/A-18 wind tunnel data, the value of Reynolds number based on mean aerodynamic chord $\text{Re}_{\bar{c}}$ is typically 1.4×10^6, and an effective forebody Reynolds number Re_D can be calculated based on vertical height of the fuselage at FS 184, which is 2.96 in. for the 0.06-scale model. Therefore, if $\text{Re}_{\bar{c}} = 1.4 \times 10^6$, a value of Re_D appropriate for the forebody is 0.5×10^6. The most similar Lamont data are for $\text{Re}_D = 0.4 \times 10^6$, and the level of normal force grows as Re_D increases from that value. The upper value of Re_D can be based on a typical flight value of $\text{Re}_{\bar{c}} = 10 \times 10^6$, which yields $\text{Re}_D \sim 3.6 \times 10^6$ and is similar to Lamont data at $\text{Re}_D = 3.9 \times 10^6$. Consequently, for the present illustration, Lamont's pressure data that will be shown are for $\text{Re}_D = 0.4 \times 10^6$, 3.0×10^6, and 3.9×10^6 at $\alpha = 20°$, 30°, and 40°.

One difference between the data at the various values of Re_D in figure 18 is in the values of M_∞. For the

lowest Reynolds number data, $M_\infty = 0.11$, and for the higher Reynolds number data, $M_\infty \leq 0.28$. Nevertheless, these different values of M_∞ are all sufficiently low enough that the normal component of Mach number relative to the body ≤ 0.18, where Polhamus (ref. 16) determined that compressibility effects begin for two-dimensional cylinders in cross flow.

Figure 18 plots these data of Lamont at pressure row locations that correspond most closely to the F/A-18 pressure rows based on figure 16. The only exception is that Lamont's most similar station to FS 184 would be the row at $x/D = 3.5$; however, for these conditions, Lamont data were apparently lost due to a malfunctioning pressure transducer. Consequently, data taken at the next pressure station at $x/D = 4.0$ will be shown instead.

The Lamont data for $\alpha = 20°$ are presented in figure 18(a) and illustrate that for the first two stations, 0.75 and 1.25, there are not any noticeable Reynolds number effects. Nevertheless, at the last two stations, 2.50 and 4.00, it is clear that both the data with $\text{Re}_D = 3.0 \times 10^6$ and 3.9×10^6 have stronger forebody vortex suction footprints near azimuthal locations $\theta = 160°$ and $\theta = 200°$ than do the data for $\text{Re}_D = 0.4 \times 10^6$. The vortex suction footprints at station 4.00 clearly are stronger than those at station 2.50.

For $\alpha = 30°$ (fig. 18(b)), differences appear in the attached flow suction peaks at $\theta = 100°$ and $260°$ at stations 0.75 and 1.25. These differences in the attached flow region are in the expected direction because the higher Reynolds number boundary layer is expected to be thinner. This thinner boundary layer would result in less growth in the boundary layer displacement thickness and would lead to an "effective" radius of curvature in the cross-flow direction closer to the value of the circular geometry. This smaller effective radius of curvature would result in the higher attached flow velocities, and consequently, in the more negative values of C_p. Noticeable differences also appear at Lamont station 1.25 with the larger Reynolds number data showing slightly more suction for $150° < \theta < 210°$. At Lamont station 2.50, very significant differences appear with increasing vortex suction peaks for the two higher values of Re_D. For Lamont station 4.0, there are significant differences between the data for $\text{Re}_D = 0.4 \times 10^6$ and the higher Re_D data, both for the attached flow suction peaks at $\theta = 80°$ and $280°$ and for the leeward vortex suction peaks. The two data sets at the higher values of Re_D are virtually identical. In contrast to the data for higher values of Re_D at $\alpha = 20°$, the magnitude of the vortex suction peaks at $\theta = 160°$ and $200°$ at station 4.00 is not as large as those at station 2.50. Given that the boundary layer character is not changing at the higher values of Re_D between stations 2.50 and 4.00, this reduction in vortex suction down

the body is attributed to vortex shedding between these two stations and the subsequent movement of the vortices away from the body. A similar character will be seen in the F/A-18 data described later in the paper.

The final data comparison for $\alpha = 40°$ (fig. 18(c)) shows the most dramatic differences. At this higher angle of attack, the $\text{Re}_D = 0.4 \times 10^6$ data are behaving as though their effective Reynolds number were decreasing. (See ref. 16 for the effect of α on effective Reynolds number.) This trend of more laminar flow indicates that the larger vortex suction peaks at stations 0.75 and 1.25 are remnants of stronger vortex shedding that occurred in the laminar region upstream of these stations. These suction peaks are actually more pronounced than the turbulent high Reynolds number peaks seen for the higher values of Re_D. The vortex suction peaks in figure 18(c) are again smaller in magnitude at station 4.00 than at station 2.50 for the two higher values of Re_D. The two data sets at the higher values of Re_D are again nearly identical.

The data of Lamont can be helpful in understanding the flow progression that may occur over the F/A-18 forebody when the Reynolds values change from conventional wind tunnel Reynolds numbers to flight Reynolds numbers. However, there are some differences in geometry between the Lamont model and the F/A-18 forebody. First, as shown in figure 4, the cross sections of the F/A-18 forebody are not circular at FS 142 and FS 184. Second, in the F/A-18 full configuration, the forebody is canted down $5.6°$ to provide the pilot with increased visibility.

If the F/A-18 generally follows the Lamont trends, with the above limitations in mind, the following might be expected when Reynolds number values change from the wind tunnel value of $\text{Re}_{\bar{c}} = 1.4 \times 10^6$ ($\text{Re}_D \sim 0.4 \times 10^6$) to the flight-like values of $\text{Re}_{\bar{c}} = 10.0 \times 10^6$ ($\text{Re}_D \sim 3.6 \times 10^6$). Effects at FS 85 and FS 107 should consist of modest differences in the leeward region between $150° < \theta < 210°$ and differences in the attached flow regions near $\theta = 100°$ and $260°$. The differences at FS 142 should be the most dramatic of the forebody stations and should illustrate large differences in the forebody vortex suction footprints near $\theta = 160°$ and $200°$. The differences at FS 184 should be more subdued than those at FS 142 and should consist of more negative values of C_p in the leeward region between $120° < \theta < 240°$ and differences in the attached flow peaks near $\theta = 90°$ and $270°$.

Of course, these expected differences underscore concerns about testing in conventional wind tunnels where the values of Re_D are not close to those of flight. For low-speed testing of large (~1/6 scale) models, values of Re_D for the forebodies are typically in the

neighborhood of 0.3×10^6 and 0.4×10^6—that is, on the slope toward decreasing values of measured side force. The typical "higher" Reynolds number tests associated with high subsonic and transonic Mach numbers with smaller models (~1/15 scale) usually fall very near the 0.8×10^6 minimum. Consequently, instead of predicting the stronger vortex influences that are typically seen at the higher values of Re_D (~4×10^6) associated with flight at high-α, ground tests may be expected to underpredict the forebody normal forces. Therefore, implementing a successful gritting procedure for high-α testing is important.

That the forebody pressure data for $Re_D = 3.0 \times 10^6$ and 3.9×10^6 gave virtually identical pressure distributions suggests that as the value of Reynolds number becomes large, the magnitude of Reynolds number effects may become small. During the presentation of the flight repeatability data, two repeat points had values of $Re_{\bar{c}}$ of 7.6×10^6 and 10.3×10^6. These values of $Re_{\bar{c}}$ correspond to values of $Re_D = 2.7 \times 10^6$ and 3.7×10^6, which are very similar to the two highest values of Re_D tested by Lamont, $Re_D = 3.0 \times 10^6$ and 3.9×10^6. Thus, on the basis of good agreement of these two high Reynolds number data sets by Lamont pressure distributions, the forebody flight data are expected to be insensitive to differences in values of $Re_{\bar{c}}$ in this range of approximately 8×10^6 to 10×10^6.

High-Angle-of-Attack Gritting Strategies

Wind Tunnel Model

Since most aircraft development programs do not have ready access to facilities that test at full-scale Reynolds numbers early in the program, the challenge for experimental test techniques is to simulate the higher Reynolds number flow during testing in conventional tunnels. Classic gritting procedures (refs. 17 and 18) were developed with the assumptions of attached flow and led to the development of the standard nose ring, which is sized and located to cause transition in the laminar boundary layer flow in the longitudinal direction.

However, when slender bodies are at moderate-to-high values of α, the flow about the bodies becomes more aligned to the cross-flow direction than to the longitudinal direction (ref. 14), and flow patterns in the cross-flow direction will be similar to those of figure 15. In the wind tunnel, with its lower values of Reynolds number, the laminar and transitional topologies will extend over more of the wind tunnel model than will be the case for flight. Consequently, to simulate the more turbulent flow typically seen in flight, it is necessary to have a transition of the flow in the cross-flow direction

between the windward plane of symmetry and the possible laminar separation position, which is usually 70° to 120° around the body from the windward plane of symmetry, depending on geometry M_∞ and Reynolds number.

In terms of where to position the grit azimuthally between the windward plane of symmetry and the possible laminar separation location, there are a number of issues to consider. First, there must be sufficient run length along the streamwise direction between the line of attachment and the position of the grit so that the Reynolds number based on this run length Re_l is greater than 0.1×10^6. This criterion is necessary for the grit to be effective according to Braslow, Harris, and Hicks (ref. 18). At a typical value of $M_\infty = 0.3$ for an atmospheric tunnel, the unit Reynolds number per foot is on the order of 1.8×10^6. A value of $Re_l = 0.1 \times 10^6$ would consequently correspond to an effective streamline distance of 0.7 in. Because the streamlines moving away from the line of windward attachment will have components in both the longitudinal and cross-flow directions, a conservative placement guideline would be to place the grit at least 0.7 in. in the azimuthal direction from the expected windward line of attachment.

The second issue to be considered is whether or not the model will be tested in sideslip. If sideslip is required, the azimuthal location of the grit should be pushed even farther from the windward plane of symmetry. The concern is that in sideslip, the line of windward attachment could migrate close enough to the grit on one side so that the value of Re_l is no longer greater than 0.1×10^6 and could lead to the grit being ineffective on that side and effective on the other, a situation to avoid.

A final issue is that reported in reference 19 for two-dimensional cylinders in cross flow. Patterns that place grit in high-velocity regions near the maximum half-width of a body $\theta \sim 90°$ can result in excessive loss of boundary layer momentum and can lead to premature boundary layer separation. This last issue constrains one not to place the grit too far from the windward plane of symmetry because of this potential excessive "grit drag" when the grit is placed too close to the attached-flow, maximum velocity region. Excessive "grit drag" would manifest itself as too much normal load on the forebody. Data confirming excessive "grit drag" due to a global grit pattern that had grit throughout the regions of maximum velocity are illustrated in reference 20 for an ogive-cylinder test.

Consequently, to optimally place grit along a smooth-sided forebody to better simulate high Reynolds number, high-α flows requires trading off two conflicting goals. The first is to push the grit outward, away from the windward plane of symmetry, to give the grit the best

chance of tripping the flow and to reduce the sensitivity of the grit to shifts in the line of flow attachments due to sideslip variations. The second goal is to keep the grit away from the regions of maximum flow velocity, where the momentum losses in the boundary layer would be more detrimental.

The most successful high-α gritting pattern of related Langley research (refs. 1 and 20) uses "twin strips," in which one strip of grit is placed longitudinally along each side, in addition to the standard nose ring of grit. This twin-strip pattern is called the "baseline" pattern in the current study and is illustrated in figure 19(a) for the 0.06-scale model. The values of the azimuthal angle of the strips θ, which is measured from the windward plane of symmetry, change from 72° near the nose to 58° aft near the longitudinal position where the LEX's begin. Near the nose at FS 85, the center of each twin strip is about 0.75 in. along the surface in the azimuthal direction from the windward plane of symmetry, which is just beyond the 0.70-in. criterion for the present test conditions. At FS 107, 142, and 184, the twin strips are respectively 1.0, 1.4, and 1.5 in. from the windward plane of symmetry.

The standard nose ring is retained to cause a flow transition in the longitudinal direction at low angles of attack whereas the twin strips cause a flow transition in the cross-flow direction at higher angles of attack. The baseline, high-α pattern uses No. 180 (0.0035-in. nominal size) grit for the twin strips, which are approximately 0.25 in. wide, except close to the nose where they narrow, and No. 90 (0.0070-in. nominal size) grit for the nose ring, which is about 0.12 in. wide and is 1 in. back from the nose tip (along the surface). Figure 19(b) illustrates the baseline gritting pattern. The No. 90 grit in the nose ring was sized on the basis of reference 18, and the No. 180 grit in the twin strips was determined, on the basis of the changed character of the pressure distributions, to be sufficiently large to cause a transition in the flow for $M_\infty = 0.3$, even though No. 90 grit would be a more usual choice, based on reference 18.

Several alternatives to the baseline, high-α pattern were also explored. The first alternative, shown in figure 19(c), was the baseline pattern plus No. 180 grit forward of the nose ring. For this pattern, a 0.0625-in. gap was left between the nose ring and the forward grit. The additional grit pattern extended forward to within 0.12 in. from the nose tip. Another 0.0625-in. gap in this forward grit addition occurred at FS 70, where there is another pressure row in the forebody, which was not active for the current test because of a limited number of pressure modules in the model. The purpose of this "frontal" addition was to locate the transition of the boundary layer as far toward the nose tip as possible.

A second alternative, shown in figure 19(d), was to retain the baseline pattern and add No. 80 (0.0083-in. nominal size) grit to the maximum half-width region of the forebody. Because the pressure rows could not be covered, the additional grit pattern was placed in four blocks on each side of the forebody. One block was located between the nose ring and the pressures at FS 85, the second block was located between the pressures at FS 85 and FS 107, the third block spanned FS 107 and FS 142, and the last block was located between FS 142 and FS 185. A 0.0625-in. gap was left between the existing twin strips and the four blocks, and the longitudinal separation between the blocks was 0.35 in. to keep the grit a distance from the pressure rings. The location of the top of the blocks was determined by running a line from the forward tip of the LEX to the nose ring along a constant azimuthal location. The intention of this "side" pattern was to assess "overgritting" the forebody.

A third alternative, illustrated in figure 19(e), was to modify the twin strips of the baseline pattern with narrower twin strips at the same azimuthal location. The baseline pattern was approximately 0.25 in. wide, whereas the narrower strip was approximately 0.13 in. wide. The purpose of this gritting alternative was to determine whether the data were sensitive to the strip width.

A fourth alternative pattern evaluated, shown in figure 19(f), was with the nose ring only. This pattern was actually run twice—before and after the high-α gritting patterns. These data were also used to assess repeatability for the experiment.

Flight Vehicle

A unique opportunity to gain further insight into the effects of high-α gritting occurred when a high-α gritting pattern was applied to the HARV vehicle during the course of the flight test program (ref. 21). The grit pattern was similar to the "twin strip" portion of the baseline pattern used for the 0.06-scale model. For flight, however, the twin strips were located 80° above the windward plane of symmetry, as shown in figure 20. The grit was No. 36 (0.0232-in. nominal size), and the longitudinal strips were only 0.13 in. wide. The strips extended from 1 in. back from the nose tip to just below the LEX apex.

Discussion of Results

The order of data presentation will be as follows. First, the effects of gritting on pressures in flight will be summarized to highlight the effects that gritting might have in the wind tunnel. Second, wind tunnel pressure data with baseline high-α gritting and with the nose-ring-only pattern will be compared to ungritted flight pressure data. Next, comparisons will be made for the baseline

8

pattern plus frontal gritting, the baseline pattern plus side panels of grit, and the baseline pattern using narrower twin strips.

Summary of Gritting Effects in Flight

Even though the flight data are at high Reynolds numbers, forcing transition to be within inches of the forebody tip by gritting showed a definite impact on the forebody surface pressures. As pointed out by Fisher, Del Frate, and Richwine in reference 6, the reason for this impact is that, even in flight, there is evidence of laminar separation bubbles and turbulent reattachment nearly as far aft as FS 107 at high values of α. Consequently, when gritting is applied to cause transition of the boundary layer flow close to the tip, which is at FS 60, the flow topology over the first 40 or 50 in. of the airplane can be altered.

The comparisons of grit-free and gritted-flight forebody and LEX pressures are shown in figures 21 and 22. The flight data with grit were not taken for the full range of angles of attack. For comparison to the wind tunnel data, the two closest values of angles of attack are $\alpha = 35°$ and 45°. The forebody pressure comparisons are summarized in figure 21 at these two values of α. The agreement between grit on and grit off is quite good for $\alpha = 35°$, with the exception of the vortex suction peaks at FS 107, figure 21(a), which occur at $\theta = 165°$ and 195° and at FS 142, which occur at $\theta = 160°$ and 200°. For the more forward location, the vortex suction peaks are stronger for the grit-on case, while the reverse is true at FS 142. The stronger vortex suction at FS 107 would be expected on the basis of general Reynolds number arguments; however, the reduction in the suction at FS 142 may result from the stronger vortices at FS 107 shedding earlier from the body. Interestingly, vortex shedding from the model of Lamont also appears to be occurring between the comparable stations 2.50 and 4.00.

Data for $\alpha = 45°$ are shown in figures 21(b) and (c) and indicate similar results for both no sideslip and sideslip. At this value of α, however, the stronger forebody vortices with gritting are now apparent even for the FS 85 station, where the vortices footprints are larger, as evidenced by the increased suction pressures on the lee side near $\theta = 160°$ and 200°. At FS 107, the contrast in the suction pressures between the gritted data and the ungritted data is even larger than at $\alpha = 35°$. There is still a reduction in suction peak at FS 142. The data at FS 184 seem to be rather insensitive to the presence of the grit. The same trends hold for $\alpha = 45°$ and $\beta = 4°$, as shown in figure 21(c).

The LEX pressure distributions are illustrated in figure 22 and contain some differences between the no-grit and twin strip flight data. However, there is no definite trend for these differences. Furthermore, the magnitude of these differences in C_p at all three stations is on the same order as the repeatability data of figure 13, $\Delta_r C_p \sim \pm 0.2$.

To summarize, the effect of a high-α gritting pattern in flight is to increase the strength of the forebody vortices at FS 85 and 107. However, the strength at FS 142 is reduced, possibly due to vortex shedding. The pressure distribution at FS 184 seems to be insensitive to the presence of gritting. There is no consistent trend in the LEX pressures resulting from the gritting.

Baseline Pattern Compared to Nose-Ring-Only Pattern and Flight Data

The first pressure comparisons are for the wind tunnel data using the baseline gritting pattern compared to the nose-ring-only data and to the flight data. The forebody pressure comparisons are shown in figure 23. For $\alpha = 20°$ (fig. 23(a)), the gritted and ungritted data for the wind tunnel (the solid and dotted lines) fall very close to each other. The wind tunnel data, however, appear to have differences with the flight data in the attached flow regions $90° \leq \theta \leq 120°$ and $240° \leq \theta \leq 300°$ for both FS 85 and FS 107. In these regions the flight pressure coefficients data are more negative than the tunnel values. The flight data at FS 142 contain pressure spikes due to the presence of antenna covers on the flight forebody (ref. 7) in the vicinity of $\theta = 95°$ and 265°. These flight pressure perturbations in these regions of θ will be apparent at all values of α and β. The presence of the gun bay vents for the flight vehicle (ref. 7) at FS 184 is the reason that there are no flight pressure data for $0° \leq \theta \leq 48°$ and $312° \leq \theta \leq 360°$ and may be the reason that there are differences in the pressures between flight and tunnel data for the regions $48° \leq \theta \leq 90°$ and $270° \leq \theta \leq 312°$ at some of the higher values of α.

For $\alpha = 30°$ (fig. 23(b)), differences between flight and tunnel data continue to be apparent in the attached flow pressure regions near $\theta = 105°$ and 255° at FS 85 and FS 107. A discontinuity appears in the baseline data at $\theta = 72°$ at FS 107 and at $\theta = 90°$ at FS 142, which are apparently bad pressure ports for the baseline pattern runs. For both figures 23(a) and (b), the flight data appear to have had more highly accelerated flow about these pressure minimums than do the tunnel data. These differences could be due to the higher Reynolds number of flight, as was expected on the basis of the Lamont data, or they could be due to repeatability differences in the data. Unfortunately, there is not enough statistical information for either the flight or wind tunnel data sets to more properly quantify what the error bars should be.

At FS 142, the utility of the baseline grit pattern is already apparent in that the grit-ring-only data show no evidence of vortex suction peaks on the leeward side near $\theta = 160°$ or $200°$, while the baseline pattern clearly simulates the presence of the suction peaks, even though their strengths are underpredicted. At FS 184, the nose-ring-only data are more negative than the baseline data and match the flight data better. These differences at FS 184 between the wind tunnel data, however, are within the level of repeatability established for the forebody, $\Delta_r C_p \sim \pm 0.05$.

A similar situation is seen for $\alpha = 35°$ (fig. 23(c)). Again, differences are seen between the flight and wind tunnel data for the attached flow pressure minimums near $\theta = 105°$ and $255°$ at FS 85 and FS 107. The vortex suction peaks at FS 142 are again better represented by the baseline data than by the nose-ring-only data. While the wind tunnel baseline gritted pattern underpredicts the ungritted, flight vortex suction peaks, the baseline gritted peaks are nearly identical to those shown in figure 21(a) for the gritted flight data at FS 142 for $\alpha = 35°$. At FS 184, it is not clear which pattern matches flight better. The nose-ring-only data seem to agree better with the flight data for $0° < \theta < 180°$, while the baseline pattern data agree better for $180° < \theta < 360°$. In general, all differences are within the uncertainty seen in the respective tunnel or flight data except for the vortex suction peaks at FS 142. Clearly, the baseline twin strip pattern is doing a better job of simulating the flight pressures for these very prominent features than is the nose-ring-only pattern.

The data for $\alpha = 40°$ and $\beta = 0°$, $4°$, and $8°$ are highlighted in figures 23(d) to (f) and substantiate the benefits of the baseline gritting pattern. Apart from the known bad orifices at FS 107 and $\theta = 72°$ and at FS 142 and $\theta = 90°$, the baseline pattern more accurately simulates both the suction peak magnitudes and leeward side pressure gradients for FS 142 and FS 184. A significant difference between the two wind tunnel data sets is seen for $\beta = -8°$ (fig. 23(f)) at the attached flow pressure peak near $\theta = 240°$. The nose-ring-only pattern clearly overpredicts this suction peak, compared to the baseline pattern or to the flight data.

The corresponding data for the LEX pressures are shown in figure 24. Interpreting the LEX pressure data for the F/A-18 can be more difficult than the forebody pressures because of asymmetries in the pressures between the left and right LEX's. These asymmetries, which will appear in both the flight and wind tunnel data, probably arise from geometric asymmetries, left to right, over either the forebody, the LEX's, or both. When interpreting the data, it is also important to remember that the pressure coefficients over the LEX's generally had somewhat larger values of uncertainty due to repeatability

than did the forebody pressures. These values were $\Delta_r C_p \sim \pm 0.1$ for the wind tunnel and $\Delta_r C_p \sim \pm 0.2$ for the flight data.

Figure 24(a) compares the two tunnel data sets to flight data for $\alpha = 20°$ and $\beta = 0°$. In this figure the nose-ring-only data and the baseline data are virtually identical, as was the case for the forebody pressures. Both sets of data, however, display values of C_p that correspond to less suction underneath the LEX vortices than do the flight data. The level of mismatch, $\Delta C_p \sim \pm 0.2$, could be reduced at FS 253 if the wind tunnel data were simply switched from left to right sides. Such a switch could be justified on the basis that these LEX pressure asymmetries, which are assumed to be the result of random geometric differences left to right, could have been just as easily in the opposite sense for either the HARV or the 0.06-scale model.

The behavior for $\alpha = 30°$ (fig. 24(b)) is similar to that for $\alpha = 20°$. Here the utility of switching the flight data left to right is even a little clearer as the agreement would be improved at both FS 253 and FS 357. At FS 357, both tunnel data sets show comparable suction underneath the LEX vortices in comparison to the flight data.

At $\alpha = 35°$ (fig. 24(c)), the tunnel data begin to consistently approach the levels of suction found in flight at all fuselage stations and, again, would agree better if the wind tunnel data were switched left to right. As mentioned earlier, the flight data and the wind tunnel data are expected to have respective uncertainty due to repeatability of ± 0.2 and ± 0.1 in their values of C_p.

The comparisons for $\alpha = 40°$ and $\beta = 0°$, $4°$, and $8°$ (figs. 24(d) to (f)) show that both sets of wind tunnel data generally follow the trends from flight. Sometimes the high-α gritting data appear to match flight data better, and sometimes the grit-ring-only data appear to match flight data better. While the differences at some orifice locations between the tunnel data are sometimes larger than $\Delta_r C_p \sim \pm 0.1$, there are no systematic trends favoring one pattern over the other.

Force and moment comparisons for the wind tunnel data with the baseline grit pattern and the nose-ring-only pattern are given in figures 25 and 26. The longitudinal properties (fig. 25) show very little difference between the two configurations. In fact, the only noticeable differences occur with an apparent pitch-up tendency for the nose-ring-only pattern. This "trend," however, may simply be variation in the data due to the balance and will be discussed in more detail in the section entitled "A Closer Look at Longitudinal Forces and Moments."

The lateral-directional comparisons for $\alpha = 30°$, $35°$, and $40°$ (fig. 26) illustrate that the differences between the baseline gritting data and the nose-ring-only data are sensitive to α. For example, in figure 26(a) for $\alpha = 30°$, differences are small and are on the order of the repeatability differences previously shown in figure 8, where data were available only for $\alpha = 40°$. At $\alpha = 35°$, however, some significant differences are beginning to appear in the values of C_l, with the baseline data being more linear and exhibiting more lateral stability, where lateral stability is defined as a negative slope of C_l with β. At $\alpha = 40°$, these differences are even more pronounced with the baseline grit data being more stable and linear than the grit-ring-only data for values of $|\beta| > 2°$.

Comparing Baseline to Baseline Plus Frontal Grit Pattern

The first alternative grit pattern comparisons will be for the baseline pattern with additional No. 180 grit ahead of the nose ring, or what is called the "baseline plus frontal" grit pattern. On the basis of the effects of earlier transition to fully turbulent flow seen in flight for $\alpha = 35°$ and $45°$, one might expect to see stronger vortex footprints at FS 85 and FS 107, with possibly weaker vortex footprints at FS 142. For the present wind tunnel data at $\alpha = 20°$ (fig. 27(a)), the baseline-plus-frontal and baseline data sets agree within the repeatability of the data, which was illustrated in figure 9. Apparently there is not enough forebody vortical flow at this low value of α to be influenced by the presence or absence of the frontal grit. At values of $\alpha = 30°$ and $35°$ (figs. 27(b) and (c)), grit in front of the grit ring does, as expected, a more effective job of causing transition in the flow upstream of the ring, as evidenced by larger vortical suction peaks in the first forebody pressure ring at FS 85. There is no clear impact at FS 107; therefore, this is a difference over what would be expected based on the flight data with gritting. Interestingly, as shown in figure 27(d) for $\alpha = 40°$, the same decrease in forebody suction footprint occurs at FS 142 as was the case for the flight data with gritting. In general, there is better agreement between the baseline gritting pattern and flight data without grit than between the baseline plus the frontal grit and the flight data without grit.

The corresponding comparisons for the LEX pressures are highlighted in figure 28. Here, however, differences between the baseline plus frontal grit and the baseline pattern are not as obvious as with the forebody pressures. Furthermore, the differences between the two gritting patterns are well within the wind tunnel repeatability uncertainty of $\Delta_r C_p \sim \pm 0.1$ for nearly all the α and β combinations. The differences for the data corresponding to $\alpha = 40°$ and $\beta = 8°$ at FS 296 and $y/s = 0.6$ (fig. 28(f)) are outside this uncertainty level and are on

the same order as the uncertainty in the flight data, $\Delta_r C_p \sim \pm 0.2$, at these more severe conditions. Neither pattern is consistently closer to the flight data than the other for all the α and β combinations shown in figure 28.

The force and moment data for this comparison are shown in figures 29 and 30. The only noticeable differences in the longitudinal properties occur in C_m. Again, these differences will be discussed in more detail in the section entitled "A Closer Look at Longitudinal Forces and Moments." The only significant differences for lateral-directional properties are for C_l, where a nonlinearity in the baseline pattern between $\beta = 0°$ and $\beta = -2°$ is eliminated by the addition of the frontal pattern.

Comparing Baseline to Baseline Plus Side Panel Grit Pattern

The next alternative grit pattern was to add grit onto the side of the forebody above the position of the usual twin strips (fig. 19(d)). This "side" pattern was intended to simulate having grit in the region of maximum attached flow velocity along the sides of the forebody. This pattern is an opportunity to determine whether having excessive grit ("overgritting") in the areas of maximum flow velocity leads to the detrimental effects found by Nakamura and Tomonari in reference 19. The forebody pressure data are summarized in figure 31. In this case, there are minimal differences between the grit patterns for $\alpha = 20°$ and $30°$, and these differences are within the scatter of the sample repeatability data (fig. 9). At $\alpha = 35°$, however, the vortex suction peaks for the side panel data at FS 142 begin to show more negative suction peaks than do the baseline peaks and agree better with the flight data. At FS 184, however, there is a little degradation of the agreement in the region about $\theta = 120°$ with the side grit. At $\alpha = 40°$ and $\beta = 0°$, the data with side panel grit overpredict the vortex suction strength at FS 107 and FS 142 and continue to deviate from the flight data at FS 184. For the sideslip data at $\alpha = 40°$, the differences with the baseline data increase, as does the mismatch with flight data. As expected on the basis of the Nakamura and Tomonari paper, modest decreases in the magnitude of C_p in the attached flow regions are beginning to occur at $\theta = 70°$ and $240°$ for FS 142 and at $\theta = 120°$ and $240°$ at FS 184.

The corresponding LEX pressure data are shown in figure 32. Wind tunnel differences less than the nominal $\Delta_r C_p \sim \pm 0.1$ are seen until the case of $\alpha = 40°$ and $\beta = 8°$. At this condition (fig. 32(f)), some consistent differences on the windward, or right LEX side, occur between the side panel gritting pattern and the baseline gritting pattern and the flight data. The data with side

11

panel grit show stronger vortex suction on the windward side at all three stations. Whether this difference is due to variations in the flow state at this extreme condition or to the grit pattern is not clear. In either event, the baseline data do agree more closely with the flight data.

The force and moment information is shown in figures 33 and 34. The longitudinal data in figure 33 show very little differences except for a pitch-up tendency at high-α that will be examined more in a later section. For the lateral-directional characteristics, the rolling-moment data suggest more lateral stability with the side panel grit and its associated stronger forebody vortices in the range of $|\beta| < 4°$. The yawing-moment data, already directionally unstable because of its negative slope, exhibit only a modest increase in the magnitude of instability.

Comparing Baseline to Narrower Twin Strips Pattern

In order to determine whether there was an impact due to the width of the twin strips themselves, an alternative pattern was selected with 0.13-in. wide strips in contrast to the 0.25-in. wide baseline pattern (fig. 19(e)). An examination of the forebody pressure data in figure 35 reveals few differences and is essentially within the bounds of repeatability shown in figure 9. The same result seems to be the case for the LEX pressure data seen in figure 36. The data fall within the deduced repeatability band for the LEX's, $\Delta_r C_p \sim \pm 0.1$. The agreement in the force and moment data (figs. 37 and 38) is acceptable, even though the pitching-moment data show some differences, which will be discussed further in the next section.

A Closer Look at Longitudinal Forces and Moments

Because of the differences seen in the longitudinal force and moment data when plotted to the scales shown before, further data analysis was necessary. First, instead of plotting C_L versus C_D or C_L versus C_m, it is more straightforward to graph both C_m and C_D as functions of α, which was estimated to be repeatable to within $\pm 0.02°$. Second, instead of plotting the full values of C_L, C_D, and C_m, the data trends become clearer when δ's for each of these variables were analyzed because, in this manner, the scales can be magnified.

These modifications to the longitudinal force and moment coefficients were accomplished by taking the following steps. First, all data were linearly interpolated to one set of values for α, which began at $\alpha = 22.5°$ and increased by increments of 2.5° until α reached a maximum of 40°. This range of α ensured that all data sets would have close neighboring points for the interpolation process throughout the α range. Second, once all data

sets were interpolated to have identical values of α, averages and differences could be calculated.

The average calculated was for the baseline grit pattern and the grit pattern with narrower strips. Because these two patterns gave very similar results in pressure data, it was concluded previously that the two patterns were both indicative of how the baseline grit pattern performs. Next, these averaged values of the baseline pattern were subtracted from all six gritting patterns—the baseline pattern, the baseline pattern plus the frontal grit, the baseline pattern plus the side grit, the baseline pattern with narrower twin strips, and the two applications of the nose-ring-only data. The resulting differential longitudinal properties, denoted by δC_L, δC_D, and δC_m, are presented in figure 39.

The respective uncertainties in these components can be calculated by using the Langley calibration of the balance and the trigonometric relations between C_N, C_A and C_L, C_D. This simple process results in the following values as a function of α:

α, deg	$\Delta_b C_L$	$\Delta_b C_D$	$\Delta_b C_m$
20	0.0179	0.0067	0.0041
30	.0165	.0096	.0041
40	.0146	.0122	.0041

Generally, the repeatability of the balance is expected to be better than its total uncertainty. While the plots for δC_L and δC_D indeed show less variation than the uncertainty bands, which are shown by the heavy lines in figure 39, the variation in the data for δC_m seems to be as large or larger than the uncertainty bands. Some variation is assumed to be due to the balance itself or to the operating procedures in the tunnel. For example, the data from the baseline pattern and the baseline pattern with narrower strips exhibit differences in δC_m on the order of 0.01 at $\alpha = 30°$. These two patterns give virtually identical pressure data and should be considered effectively as repeat runs. On the other hand, some of the differences in δC_m are believed to be systematic.

To help identify systematic trends and to reduce the scatter within figure 39, the data were condensed further. For this next representation, the two data sets representing the baseline pattern—the baseline data itself and the baseline with the narrower strips—are averaged. The two repeat runs with the nose-ring-only data are also averaged. Finally, as representing additional grit, the data representing the baseline plus frontal grit and the baseline plus side grit are averaged. The resulting comparisons are shown in figure 40.

The differences in the plots of δC_L versus α and δC_D versus α are well within the uncertainty lines. However, in the plot of δC_m versus α, trends appear that are still larger than the uncertainty expectations but that are consistent with gritting expectations. First, by virtue of the differencing imposed to calculate the values of δ's, the average of the baseline data and the baseline data with narrower strips is zero over the entire range of α. Second, the data from the extra gritting, added to the baseline pattern, result in more positive values of δC_m starting at about $\alpha = 25°$ and reach a plateau near $\alpha = 30°$. The more positive values of δC_m would be consistent with more grit drag or with the stronger forebody vortices evident with the additional grit. Third, while showing more positive values of δC_m up to $\alpha = 32.5°$, which is attributed to random variation in the data, the nose-ring-only data show significant negative increments beyond that value of α. These negative increments at higher values of α are attributed to the lack of effectiveness of the nose-ring-only pattern in causing transition to the turbulent flow topology. Consequently, the nose-ring-only pattern not only does not simulate the stronger vortical flow seen in flight, as evidenced by the previously presented pressures, but also does not simulate the slightly greater pitching-moment values associated with the baseline gritting pattern.

Summary Remarks on Gritting Results

Referring to the discussion of Reynolds number effects on the smooth-sided forebodies of Lamont, it was expected that as Reynolds number increased, small effects would be seen at the FS 85 station, effects would be larger at FS 107, effects would be dramatic at FS 142, and effects would be minimal at FS 184. Also, the attached flow suction peaks forward on the forebody would also be expected to increase on the basis of the Lamont data.

The performance of the high-α grit patterns sometimes emulated the Lamont data and sometimes did not. For example, virtually no effects were seen at FS 85 at all with the baseline, high-α grit pattern. By adding frontal grit to the baseline grit pattern, differences at FS 85 were created, but they seemed to show vortex suction peaks that were stronger than those in ungritted flight data and even stronger than those in the gritted flight data. The larger differences at FS 107 between the nose-ring-only wind tunnel data and the flight data were actually best reduced with the baseline pattern. The dramatic differences at FS 142 between the nose-ring-only data and flight were also reduced best with the baseline pattern. The frontal grit data suggest that with its stronger vortex suction forward on the forebody, vortex shedding occurs between the FS 107 and FS 142 and that this shedding reduces the suction peaks at FS 142. This reduction at

FS 142 would be similar to what appears in the Lamont data and in the gritted versus ungritted flight data. The baseline pattern plus side grit was expected to have some negative impact on the comparisons. At the values of $\alpha = 40°$, the vortex suction peak magnitudes were over-predicted with the side grit added.

The attached flow suction peaks did not become more negative with high-α gritting patterns as would occur with a true increase in Reynolds number. The presence of the grit in the cross-flow direction can change the boundary layer character to fully turbulent, but it cannot replicate the higher energy and thinner boundary layer that occur for flow at high Reynolds number. While a low Reynolds number test with grit can do a better job of simulating higher Reynolds number flow than ungritted data, it remains an approximation to the actual high Reynolds number flow seen in flight.

Knowing where to place the high-α grit longitudinally could improve the agreement with flight data. However, the present research program did not pursue this additional degree of freedom for a practical reason. The longitudinal position along the flight vehicle where the fully turbulent flow topology begins will be a function of angle of attack with the farthest aft cases corresponding to the highest angles of attack. Consequently, trying to optimize longitudinal location would require changes to the grit pattern for different angles of attack. These changes were not considered desirable because of the time required to change the grit pattern. The recommendation of the current work is to generally start the twin strips at the usual location in which the nose grit ring would be placed.

While differences in the LEX pressure data were sometimes larger than the expected differences based on repeatability, no systematic differences were determined between the gritting patterns. Consequently, with regard to the flow about the LEX's, it is not possible to reach any conclusions concerning the use of one grit pattern over another or even the usefulness of employing a high-α grit pattern at all.

Conclusions

The present investigation has explored using new types of high-α gritting patterns to better simulate the high Reynolds number boundary layers associated with flight in a conventional wind tunnel test with a 0.06-scale model of an F/A-18. To this end, wind tunnel data with the forebody and wing leading-edge extension (LEX) pressures resulting from high-α gritting patterns are compared to those resulting from a traditional nose ring and to flight data taken with the High-Alpha Research Vehicle (HARV). The need for this technology arises from the sensitivity of smooth-sided forebodies to

changes in Reynolds numbers and from the observation that during most conventional wind tunnel test programs for this configuration, the effective Reynolds number of the forebody will result in simulating values of normal force on the model forebody that are less than what would be seen in flight. The significant conclusions of the report include the following:

1. Based on the generic ogive-cylinder data of Lamont, it is crucial to develop an effective gritting pattern in order to more closely simulate normal force on the forebody and to simulate flight-like Reynolds number character in the pressure distributions.

2. The baseline high-α gritting pattern of this study, which is composed of both twin strips arranged longitudinally along each side of the body and a traditional nose ring, improves the pressure agreement between wind tunnel and flight data. This agreement is particularly enhanced at F/A-18 fuselage stations FS 142 and FS 184.

3. Adding additional grit to the front on the baseline high-α gritting pattern changed the C_p distribution at FS 85 and FS 142. These differences were similar to what is seen when the transition to turbulence was moved forward on the flight vehicle with twin strips. However, the general agreement of this wind tunnel gritting pattern with the ungritted flight data was not as good as that with the baseline pattern.

4. Adding side panels of grit to the baseline gritting pattern on the 0.06-scale model was an attempt to simulate the presence of excessive grit. This overgritting, in general, results in very modest losses in the suction values of C_p in the regions of maximum attached flow velocity for sideslip conditions at $\alpha = 40°$. This loss is attributed to the artificial thickening of the boundary layer from the excessive grit, which, in turn, softens the effective radius of curvature of the body in the cross-flow plane. More importantly, the vortex suction peaks at FS 142 with the side grit are actually too large when compared to the flight data. Again, this gritting pattern did not agree as well with the ungritted flight data as did the baseline pattern.

5. Replacing the twin strips with strips one-half their width resulted in no change in the pressure distributions or force and moment plots beyond what would be expected for data repeatability. This result would suggest that the data are not sensitive to the width of the twin strips.

6. While the pressure data over the forebody with the baseline high-α gritting pattern do demonstrate stronger vortical activity, changes in the longitudinal forces and moments are apparently confined to minor changes in pitching moment.

7. This same stronger forebody vortical activity with the baseline high-α gritting pattern resulted in higher levels of lateral stability. In fact, the even stronger levels of vortical flow seen with the baseline pattern plus the side panels led to yet higher values of lateral stability. Thus, it appears that there is a correlation with this F/A-18 configuration between strengths of the forebody vortices and the level of lateral stability.

8. Testing future configurations with smooth-sided forebodies with and without high-α gritting patterns is strongly recommended. The differences between the two sets of data will alert the researcher to the possible increments in pressures and forces and moments that may occur when going from the lower Reynolds numbers associated with conventional wind tunnels to the higher values of Reynolds number associated with flight. The suggested high-α gritting pattern is to add twin, longitudinal strips to a nose ring about the forebody to be certain that the transition in the boundary layer has occurred at low, moderate, and high angles of attack. The azimuthal locations of the twin strips, as discussed earlier, must be (1) far enough from the windward plane of symmetry to ensure that the Reynolds number based on run length is high enough that the grit will cause transition in the boundary layer, (2) far enough from the windward plane of symmetry to reduce the sensitivity of the grit to sideslip, but (3) not so far from the plane of symmetry that it approaches the region of maximum attached flow velocity, where the losses due to the grit can adversely impact the data. For the Langley applications, a good range of azimuthal locations is between 72° and 54° from the windward plane of symmetry.

References

1. Hall, Robert M.; Erickson, Gary E.; Banks, Daniel W.; and Fisher, David F.: *Advances in High-Alpha Experimental Aerodynamics—Ground Test and Flight. High-Angle-of-Attack Technology*, Joseph R. Chambers, William P. Gilbert, and Luat T. Nguyen, eds., NASA CP-3149, Vol. 1, Pt. 1, 1992, pp. 69–115.

2. Lamont, P. J.: Pressures Around an Inclined Ogive Cylinder With Laminar, Transitional, or Turbulent Separation. *AIAA J.*, vol. 20, no. 11, Nov. 1982, pp. 1492–1499.

3. Peñaranda, F. E.; and Freda, M. S., compl.: *Aeronautical Facilities Catalogue—Volume 1: Wind Tunnels*. NASA RP-1132, 1985.

4. Gillis, C. L.; Polhamus, E. C.; and Gray, J. L., Jr.: *Charts for Determining Jet-Boundary Corrections for Complete Models in 7- by 10-Foot Closed Rectangular Wind Tunnels*. NASA WR L-123, 1945. (Formerly NACA AAR L5G31.)

5. Herriott, John G.: *Blockage Corrections for Three-Dimensional-Flow Closed-Throat Wind Tunnels, With Consideration of the Effect of Compressibility*. NACA Rep. 995, 1950. (Supersedes NACA RM A7B28.)

6. Fisher, David F.; Del Frate, John H.; and Richwine, David M.: *In-Flight Flow Visualization Characteristics of the NASA F-18 High Alpha Research Vehicle at High Angles of Attack*. NASA TM-4193, 1991.

7. Fisher, David F.; Banks, Daniel W.; and Richwine, David M.: *F-18 High Alpha Research Vehicle Surface Pressures—Initial In-Flight Results and Correlation With Flow Visualization and Wind-Tunnel Data*. NASA TM-101724, 1990.

8. Keener, E. R.; Chapman, G. T.; Cohen, L.; and Taleghani, J.: *Side Forces on a Tangent Ogive Forebody With a Fineness Ratio of 3.5 at High Angles of Attack and Mach Numbers From 0.1 to 0.7*. NASA TM-X-3437, 1977.

9. Lamont, P. J.: The Complex Asymmetric Flow Over a 3.5D Ogive Nose and Cylindrical Afterbody at High Angles of Attack. AIAA-82-0053, Jan. 1982.

10. Lamont, P. J.: The Effect of Reynolds Number on Normal and Side Forces on Ogive-Cylinders at High Incidence. AIAA-85-1799, Aug. 1985.

11. Hall, Robert M.: Influence of Reynolds Number on Forebody Side Forces for 3.5-Diameter Tangent-Ogive Bodies. AIAA-87-2274, Aug. 1987.

12. Hunt, B. L.: Asymmetric Vortex Forces and Wakes on Slender Bodies. AIAA-82-1336, Aug. 1982.

13. Chambers, J. R.: High-Angle-of-Attack Aerodynamics—Lessons Learned. AIAA-86-1774, June 1986.

14. Keener, Earl R.: *Flow-Separation Patterns on Symmetric Forebodies*. NASA TM-86016, 1986.

15. Ericsson, L. E.; and Reding, J. P.: Asymmetric Flow Separation and Vortex Shedding of Bodies of Revolution. *Tactical Missile Aerodynamics—General Topics*. AIAA, 1992, pp. 391–452.

16. Polhamus, E. C.: *A Review of Some Reynolds Number Effects Related to Bodies at High Angles of Attack*. NASA CR-3809, 1984.

17. Braslow, A. L.; and Knox, E. C.: *Simplified Method for Determination of Critical Height of Distributed Roughness Particles for Boundary Layer Transition at Mach Numbers From 0 to 5*. NACA TN 4363, 1958.

18. Braslow, A. L.; Harris, R. V., Jr.; and Hicks, R. M.: *Use of Grit-Type Boundary-Layer Transition Strips on Wind-Tunnel Models*. NASA TN D-3579, 1966.

19. Nakamura, Y.; and Tomonari, Y.: The Effects of Surface Roughness on the Flow Past Circular Cylinders at High Reynolds Numbers. *J. Fluid Mech.*, vol. 123, Oct. 1982, pp. 363–378.

20. Hall, R. M.; and Banks, D. W.: Progress in Developing Gritting Techniques for High Angle of Attack Flows. AIAA-94-0169, Jan. 1994.

21. Fisher, David F.; and Cobleigh, Brent R.: *Controlling Forebody Asymmetries in Flight: Experience With Boundary Layer Transition Strips*. NASA TM-4595, 1994.
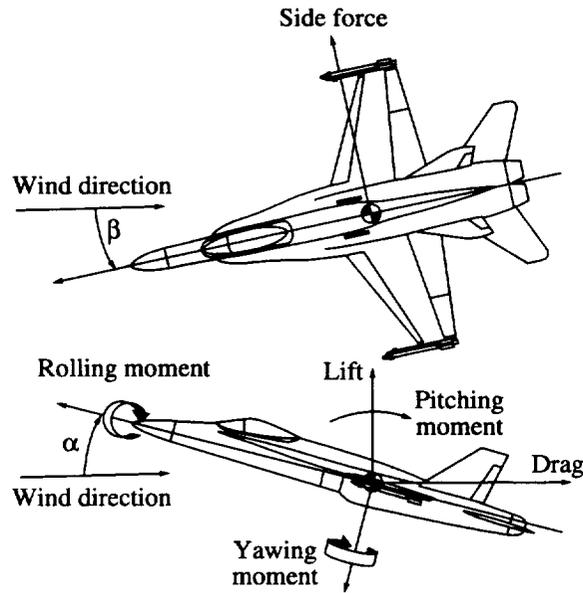
Figure 1. System of axes with positive directions of forces, moments, velocities, and angles.

Reference dimensions
$S = 400 \text{ ft}^2 (1.440 \text{ ft}^2)$
$b = 37.417 \text{ ft} (2.245 \text{ ft})$
$\bar{c} = 11.517 \text{ ft} (0.691 \text{ ft})$
c.g. = 25% $\bar{c}$

37.417 ft (2.245 ft)   56.00 ft (3.36 ft)
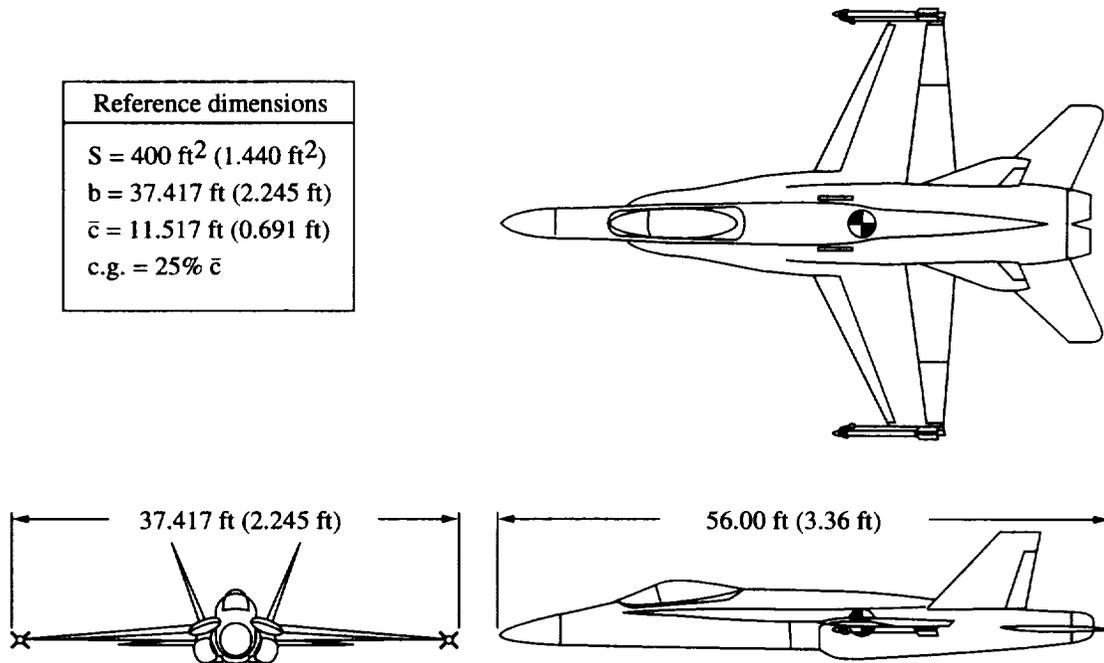
Figure 2. F/A-18 geometry details. Dimensions are in feet full scale (0.06 scale).
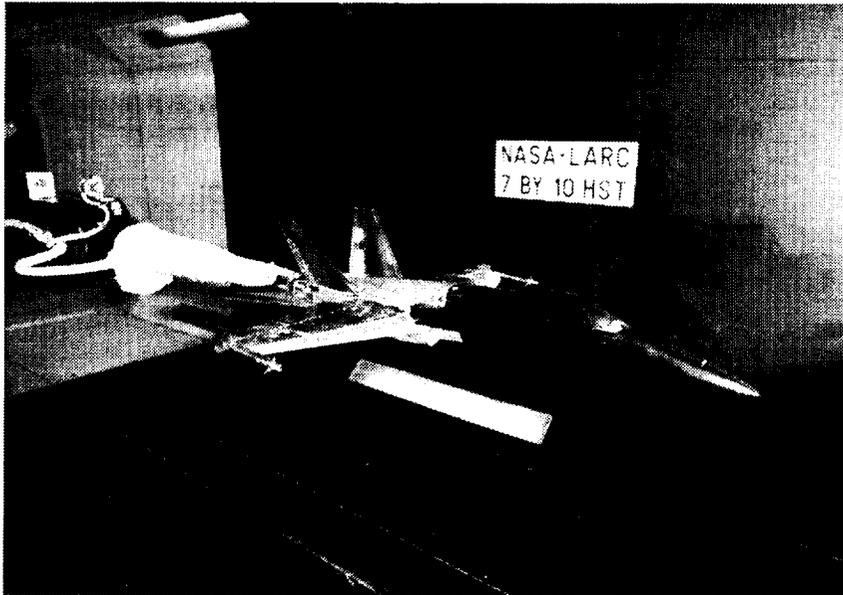
Figure 3. The 0.06-scale F/A-18 model installed in tunnel with pressure-instrumented forward fuselage shown in black.
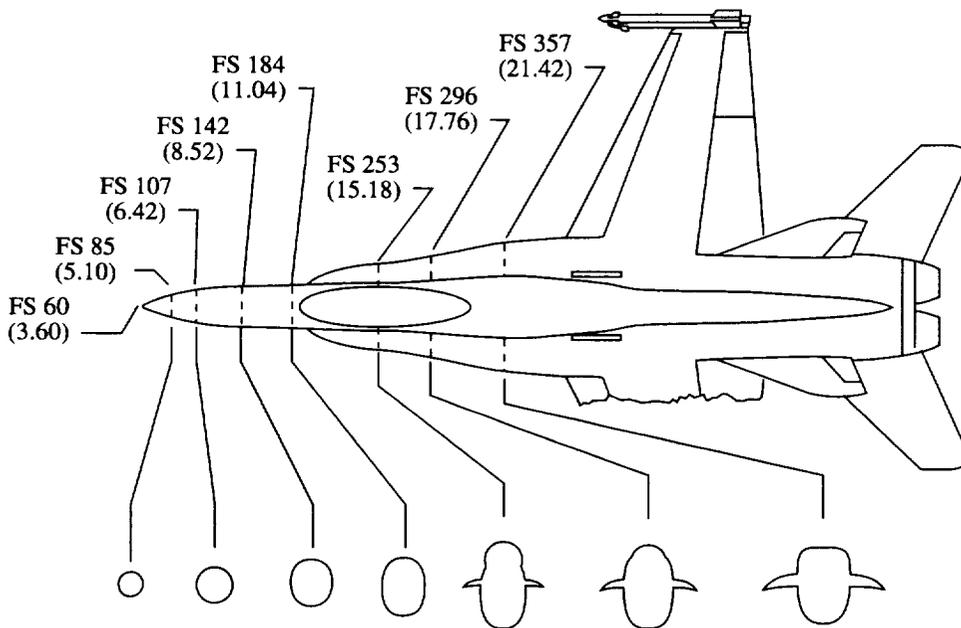
Figure 4. Forebody and LEX pressure stations used for this study for both flight and wind tunnel. Dimensions are in inches full scale (0.06 scale).

Figure 5. Repeatability assessed for longitudinal properties. No interpolation.

Test	M_∞	$Re_{\bar{c}}$	Grit	Interpolated
7×10	0.301	1.37×10^6	Nose ring	No
7×10	0.300	1.35×10^6	Nose ring	Yes
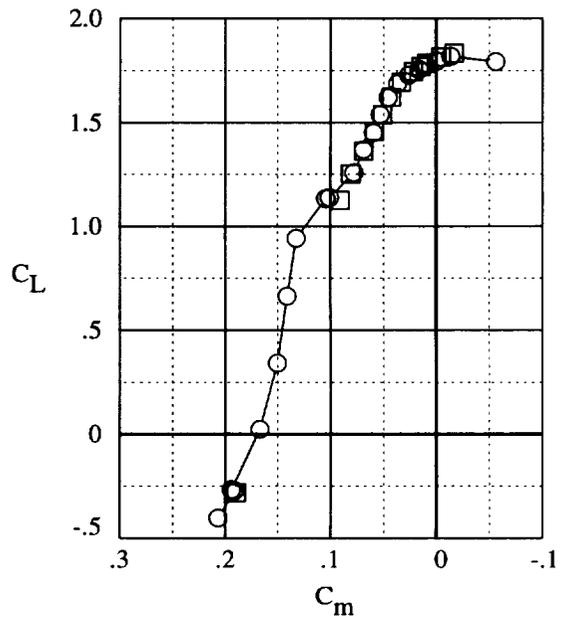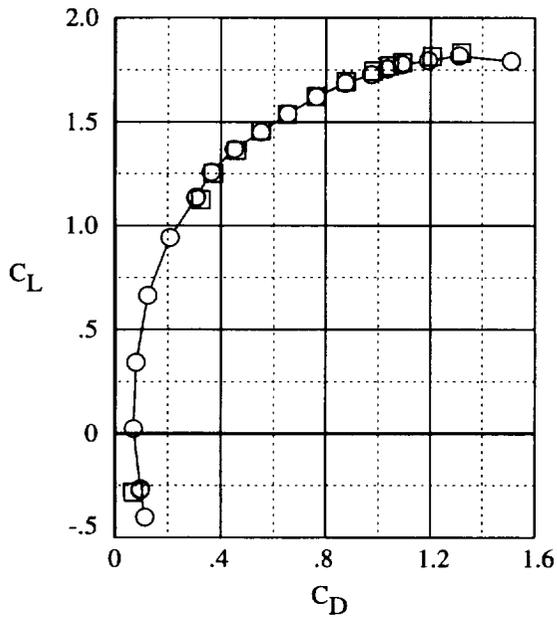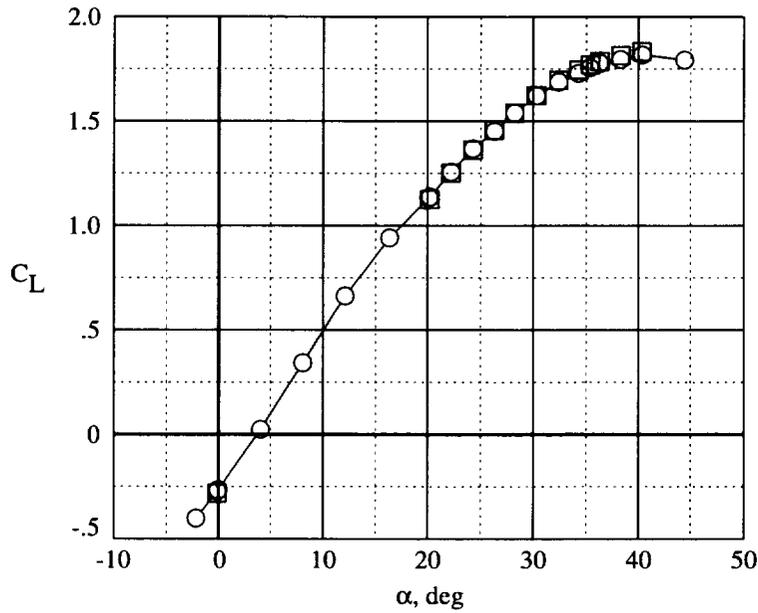
Figure 6. Repeatability assessed for longitudinal properties. Second data set interpolated to match α.

	Test	M_∞	α, deg	$Re_{\bar{c}}$	Grit	Interpolated
○———	7 × 10	0.303	40.4	1.36×10^6	Nose ring	No
□	7 × 10	0.302	41.3	1.35×10^6	Nose ring	No
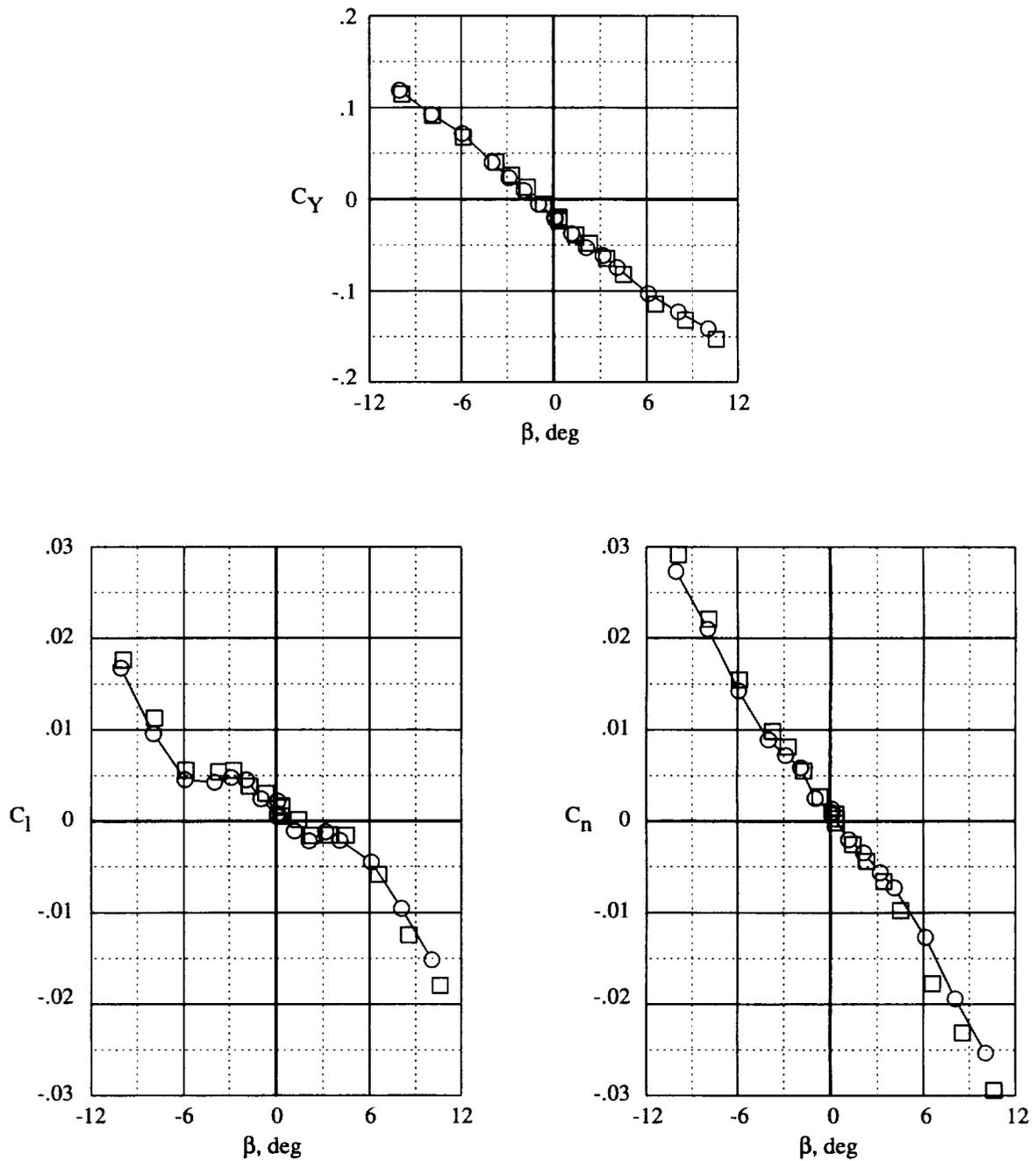
Figure 7. Repeatability assessed for lateral properties. No correction for α.

20

	Test	M_∞	α, deg	$Re_{\bar{c}}$	Grit	Interpolated
○——	7×10	0.303	40.4	1.36×10^6	Nose ring	No
□	7×10	0.303	40.4	1.35×10^6	Nose ring	Yes
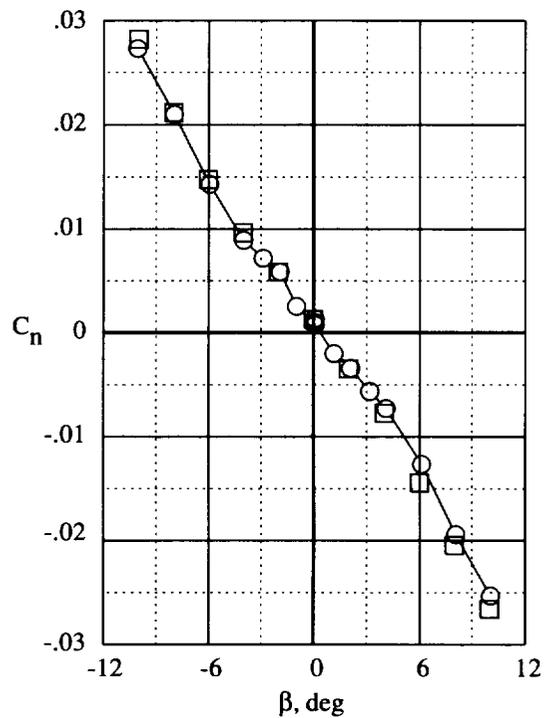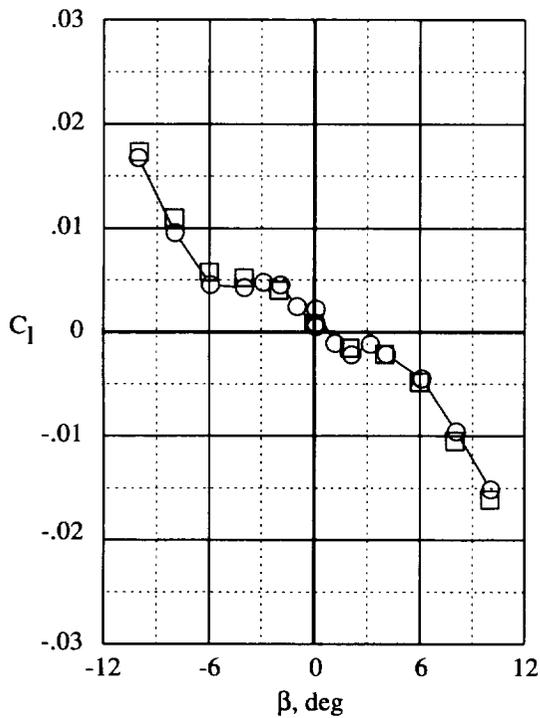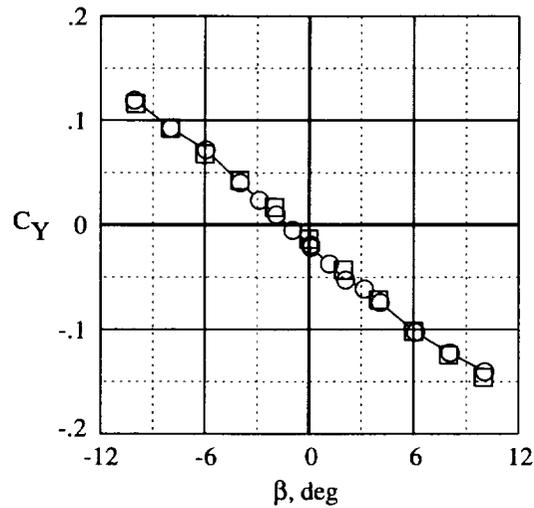
Figure 8. Repeatability assessed for lateral properties. Second data set interpolated to match α.

21

Test	M_∞	α, deg	β, deg	$Re_{\bar{c}}$	Grit	Interpolated
————	7×10	0.30	20.2	0.0	1.37×10^6	Nose ring	No
O	7×10	0.30	20.2	0.2	1.35×10^6	Nose ring	Yes

FS 85

FS 107

FS 142

FS 184
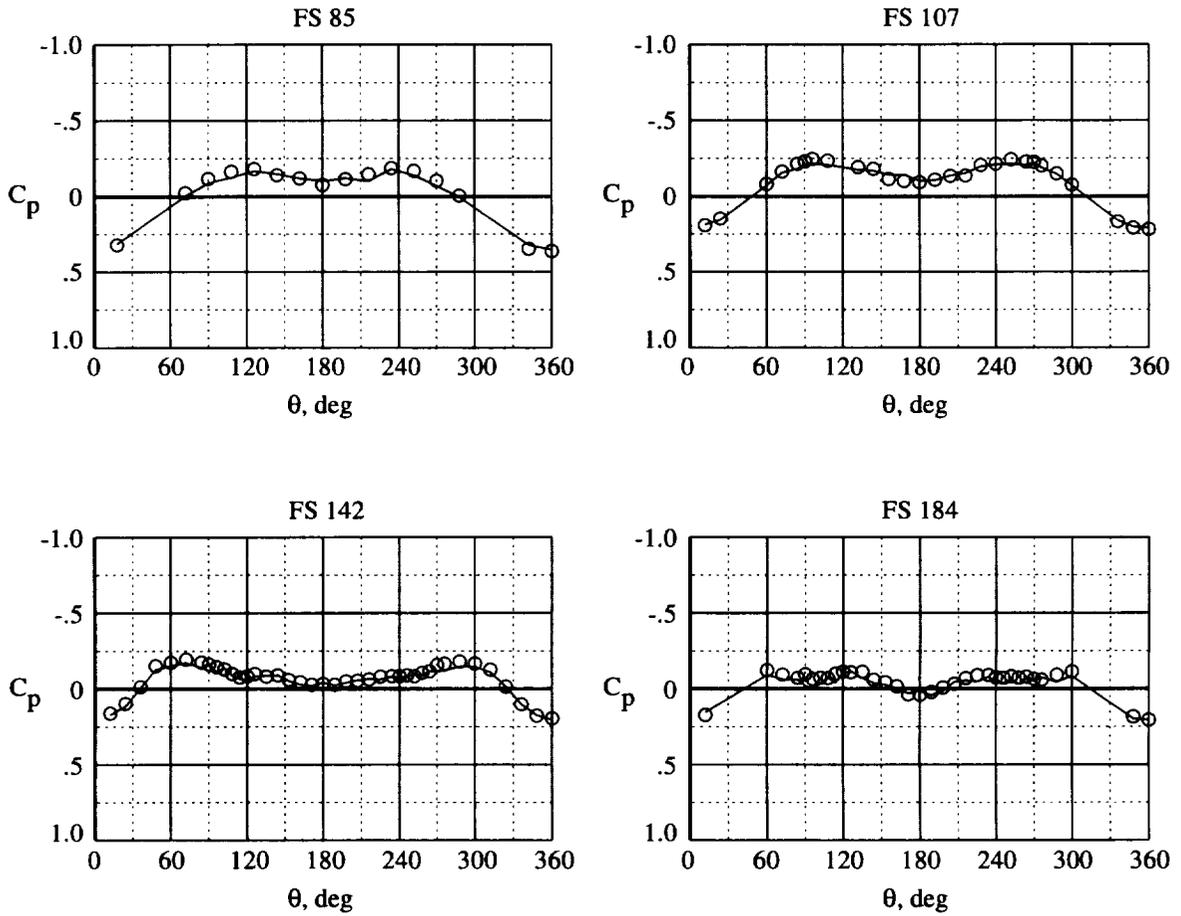
(a) $\alpha = 20.2°$; $\beta = 0°$.

Figure 9. Repeatability using interpolation routine for forebody pressure distributions. Second data set interpolated to match α.

	Test	M_∞	α, deg	β, deg	$Re_{\overline{c}}$	Grit	Interpolated
——————	7×10	0.30	30.3	0.0	1.37×10^6	Nose ring	No
o	7×10	0.30	30.3	0.3	1.35×10^6	Nose ring	Yes
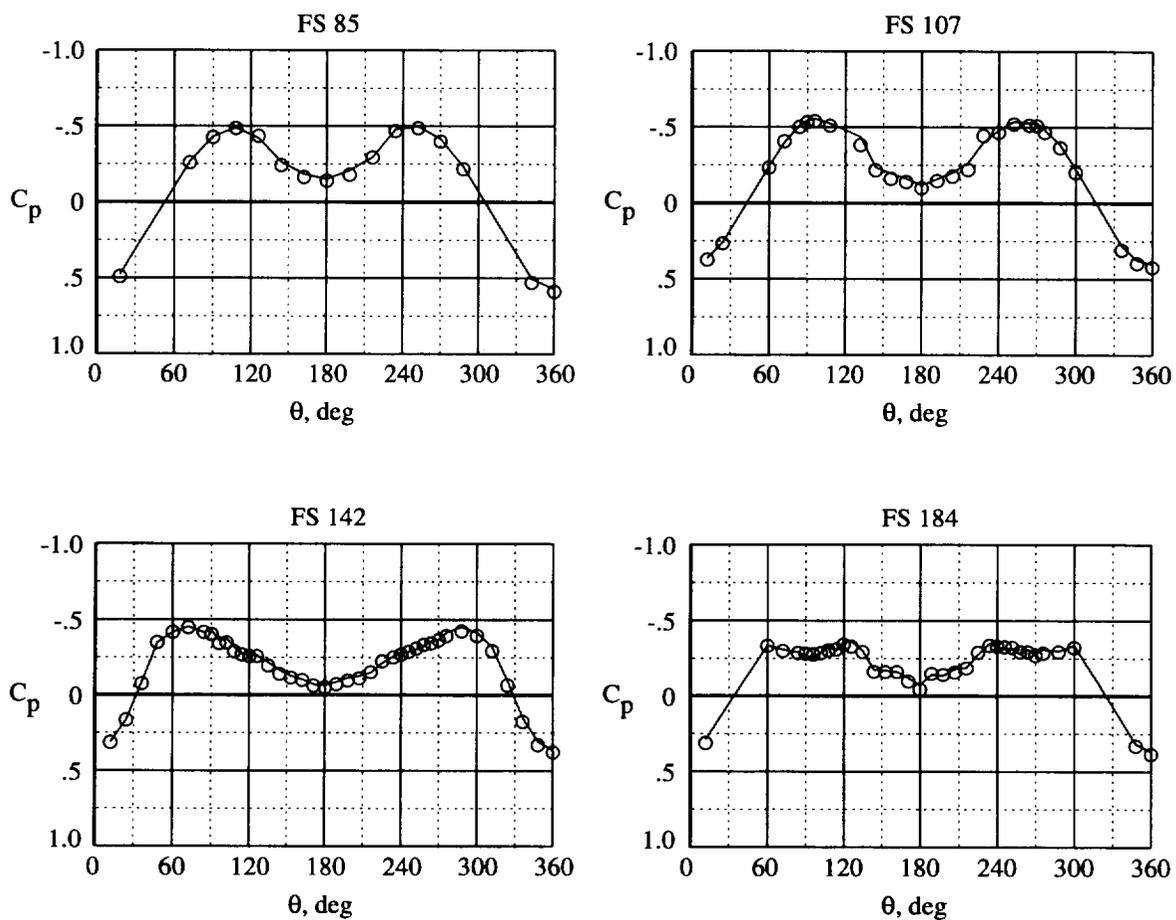
(b) $\alpha = 30.3°$; $\beta = 0°$.

Figure 9. Continued.

Test	M_∞	α, deg	β, deg	$Re_{\bar{c}}$	Grit	Interpolated
————	7 × 10	0.30	35.4	0.0	1.37×10^6	Nose ring	No
○	7 × 10	0.30	35.4	0.3	1.36×10^6	Nose ring	Yes
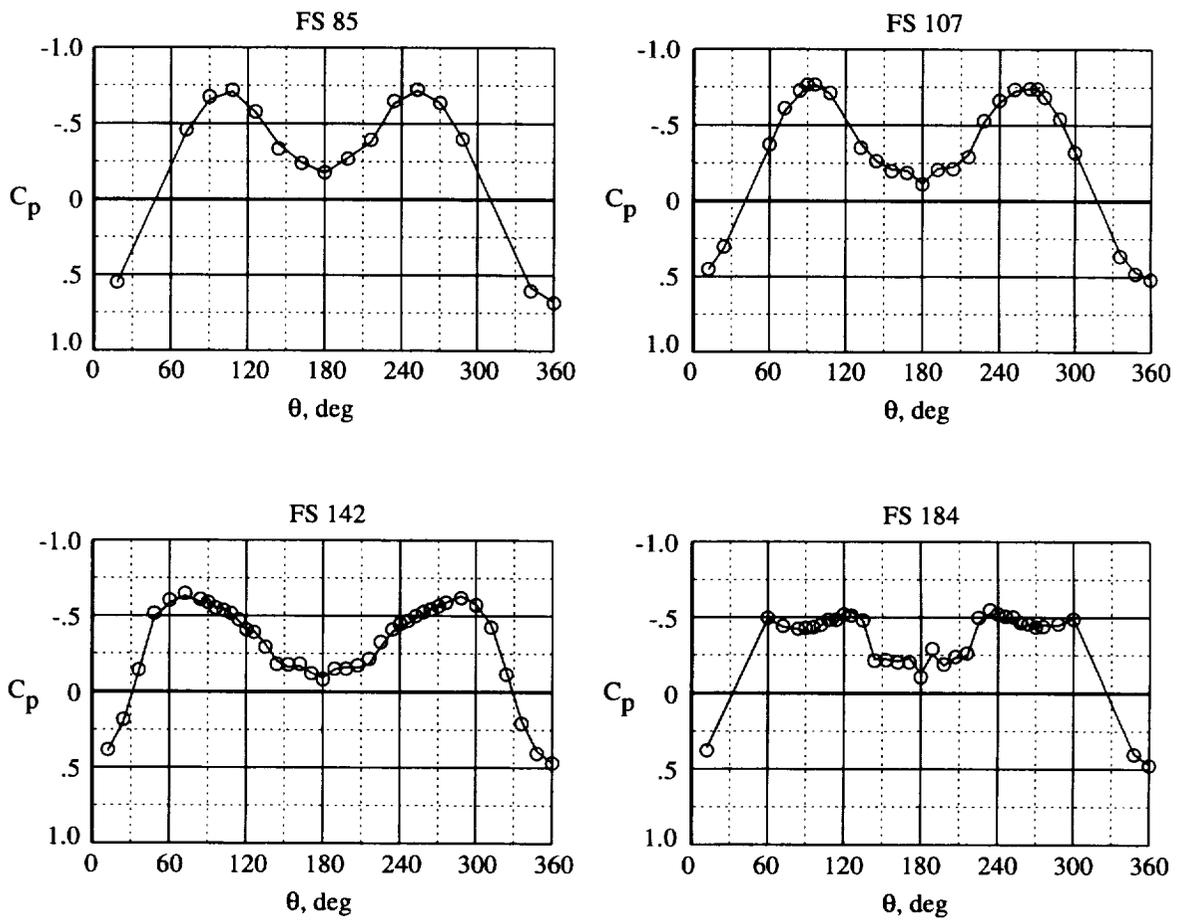
(c) $\alpha = 35.4°$; $\beta = 0°$.

Figure 9. Continued.

24

Test	M_∞	α, deg	β, deg	$Re_{\bar{c}}$	Grit	Interpolated
———	7×10	0.30	40.3	0.0	1.36×10^6	Nose ring	No
○	7×10	0.30	40.3	0.3	1.34×10^6	Nose ring	Yes

FS 85

FS 107

FS 142

FS 184
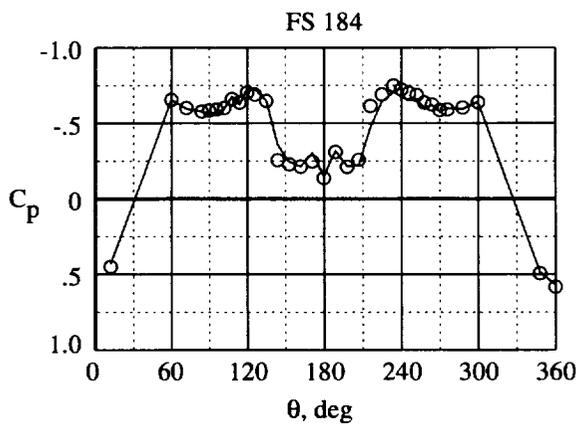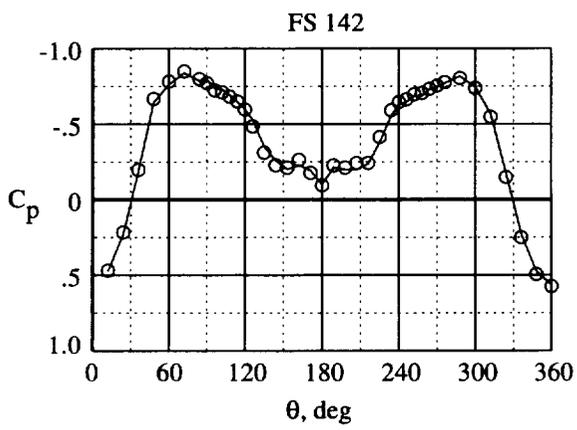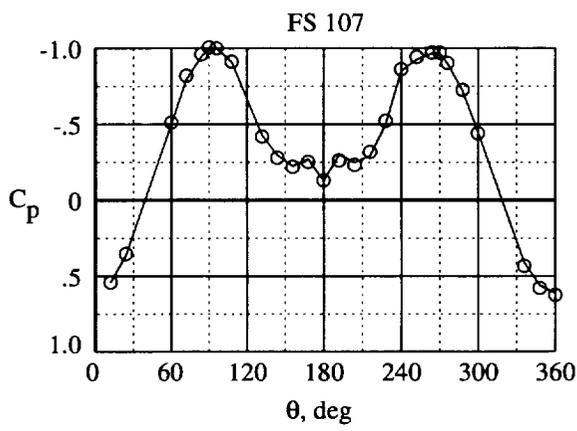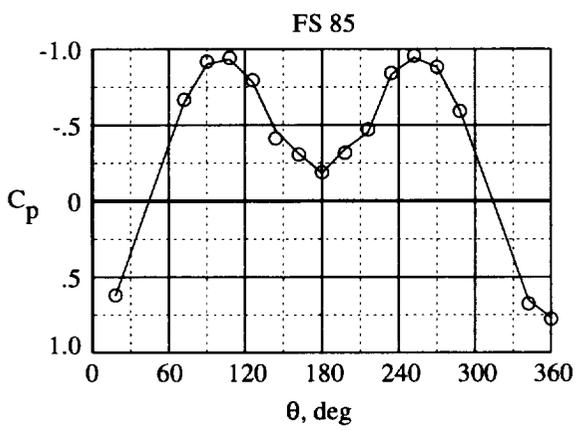
(d) $\alpha = 40.3°$; $\beta = 0°$.

Figure 9. Continued.

Test	M_∞	α, deg	β, deg	$Re_{\bar{c}}$	Grit	Interpolated
————	7×10	0.30	40.3	4.1	1.36×10^6	Nose ring	No
o	7×10	0.30	40.4	4.0	1.35×10^6	Nose ring	Yes
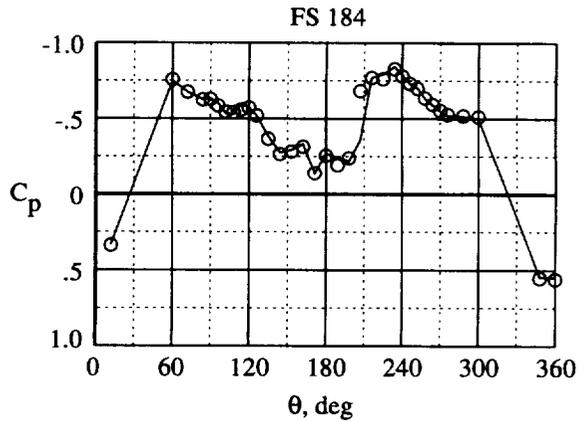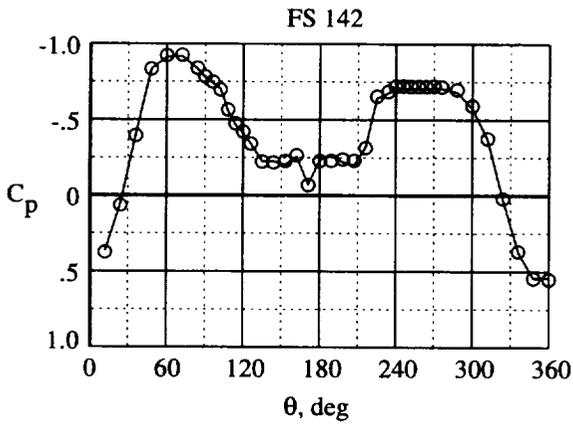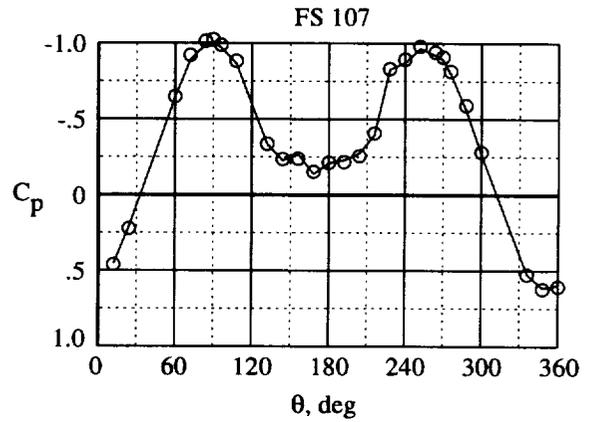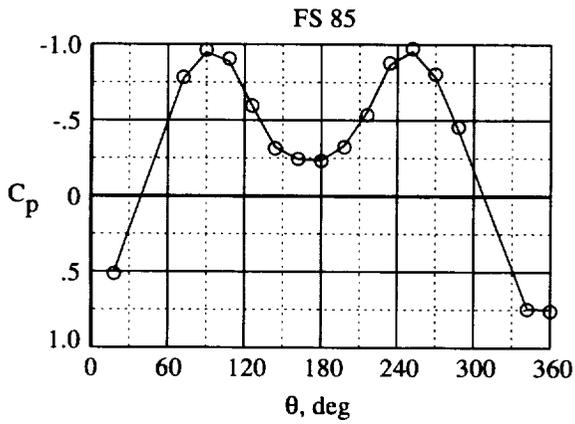
(e) $\alpha = 40.3°$; $\beta = 4.0°$.

Figure 9. Continued.

Test	M_∞	α, deg	β, deg	$Re_{\bar{c}}$	Grit	Interpolated
———	7 × 10	0.30	40.3	8.1	1.36×10^6	Nose ring	No
○	7 × 10	0.30	40.4	8.0	1.35×10^6	Nose ring	Yes
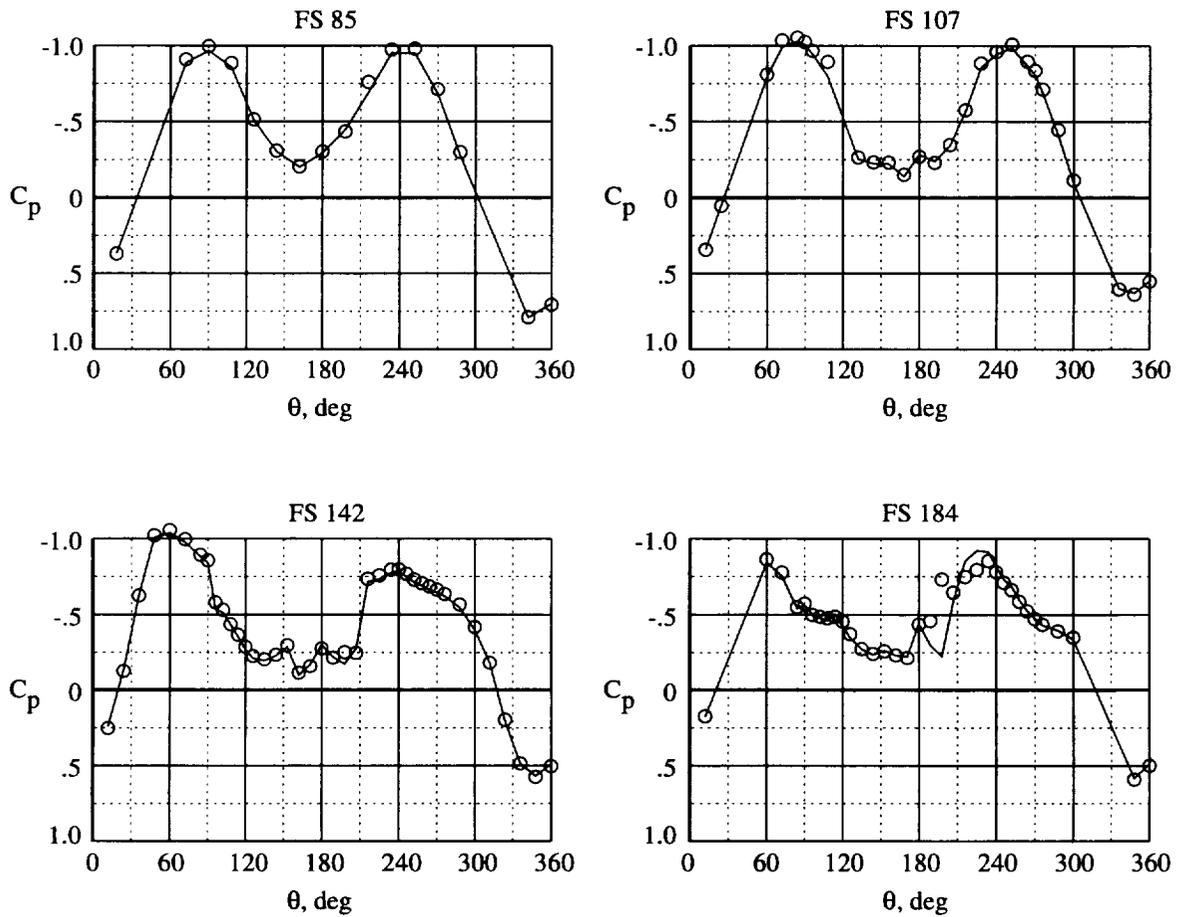
(f) α = 40.3°; β = 8.0°.

Figure 9. Concluded.

27

Test	M_∞	α, deg	β, deg	$Re_{\bar{c}}$	Grit	Interpolated
————	7×10	0.30	20.2	0.0	1.37×10^6	Nose ring	No
O	7×10	0.30	20.2	0.2	1.35×10^6	Nose ring	Yes

FS 253

FS 296

FS 357
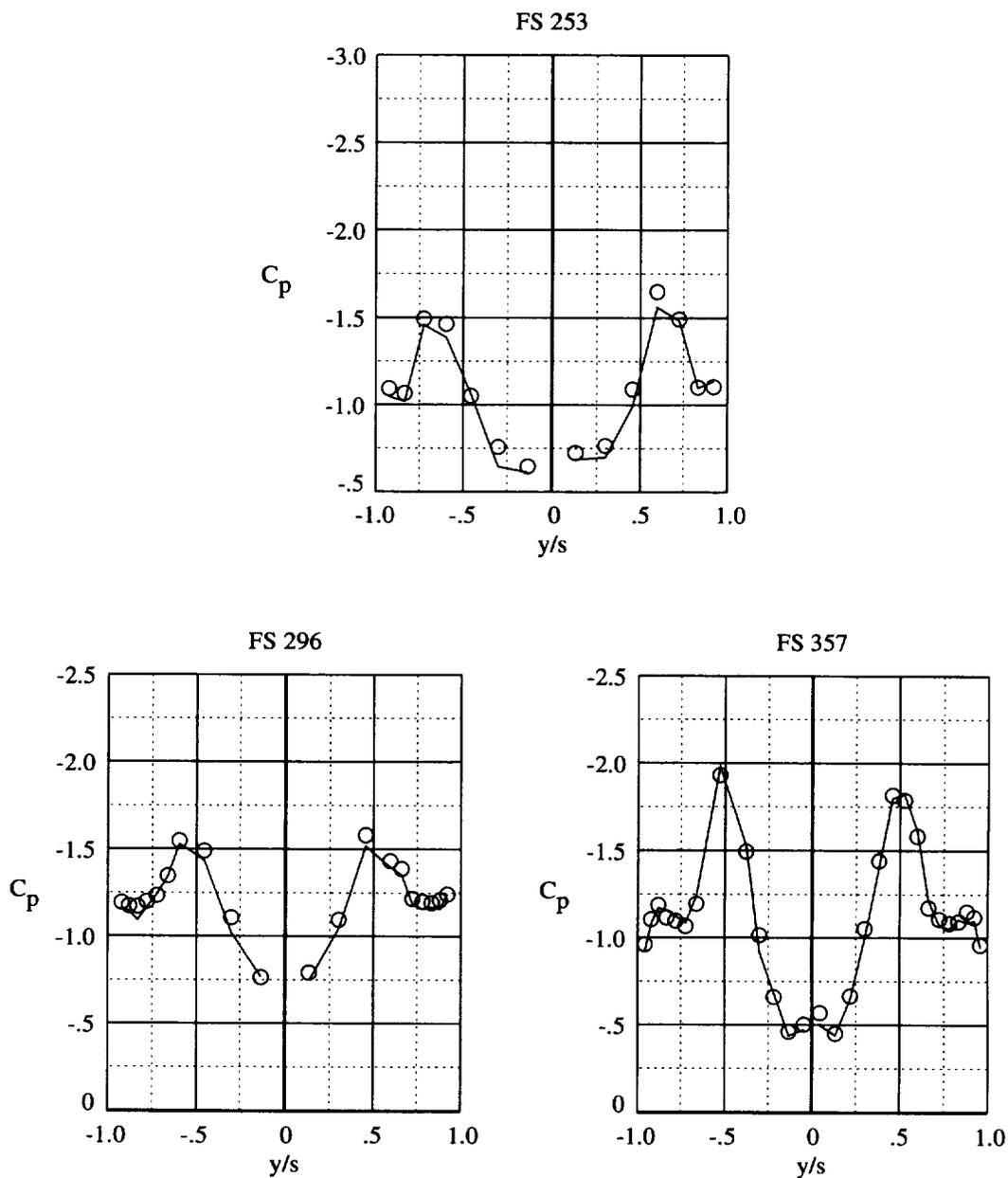
(a) $\alpha = 20.2°$; $\beta = 0°$.

Figure 10. Repeatability using interpolation routine for LEX pressure distributions. Second data set interpolated to match α.

Test	M_∞	α, deg	β, deg	$Re_{\bar{c}}$	Grit	Interpolated
————	7×10	0.30	30.3	0.0	1.37×10^6	Nose ring	No
O	7×10	0.30	30.3	0.3	1.35×10^6	Nose ring	Yes

FS 253

FS 296

FS 357

(b) $\alpha = 30.3°$; $\beta = 0°$.

Figure 10. Continued.

29

	Test	M_∞	α, deg	β, deg	$Re_{\bar{c}}$	Grit	Interpolated
———	7 × 10	0.30	35.4	0.0	1.37×10^6	Nose ring	No
O	7 × 10	0.30	35.4	0.3	1.36×10^6	Nose ring	Yes

FS 253

FS 296

FS 357

(c) $\alpha = 35.4°$; $\beta = 0°$.

Figure 10. Continued.

	Test	M_∞	α, deg	β, deg	$Re_{\bar{c}}$	Grit	Interpolated
———	7×10	0.30	40.3	0.0	1.36×10^6	Nose ring	No
O	7×10	0.30	40.3	0.3	1.34×10^6	Nose ring	Yes

(d) $\alpha = 40.3°$; $\beta = 0°$.

Figure 10. Continued.

Test	M_∞	α, deg	β, deg	$Re_{\bar{c}}$	Grit	Interpolated
————	7×10	0.30	40.3	4.1	1.36×10^6	Nose ring	No
O	7×10	0.30	40.4	4.0	1.35×10^6	Nose ring	Yes

FS 253

FS 296

FS 357

(e) $\alpha = 40.3°$; $\beta = 4.0°$.

Figure 10. Continued.

FS 253

FS 296

FS 357

(f) $\alpha = 40.3°$; $\beta = 8.0°$.

Figure 10. Concluded.

Figure 11. NASA F-18 HARV in flight.

Test	M_∞	α, deg	β, deg	$Re_{\bar{c}}$	Grit	Interpolated
———————	Flight	0.27	30.2	0.2	10.30×10^6	No grit	No
o	Flight	0.30	29.9	-0.2	7.60×10^6	No grit	No

FS 85

FS 107

FS 142

FS 184

(a) $\alpha = 30°$; $\beta = 0°$.

Figure 12. Repeatability for flight forebody pressure data.

35

	Test	M_∞	α, deg	β, deg	$Re_{\bar{c}}$	Grit	Interpolated
——	Flight	0.24	35.1	-0.5	8.88×10^6	No grit	No
o	Flight	0.32	35.5	0.0	8.66×10^6	No grit	No

FS 85

FS 107

FS 142

FS 184
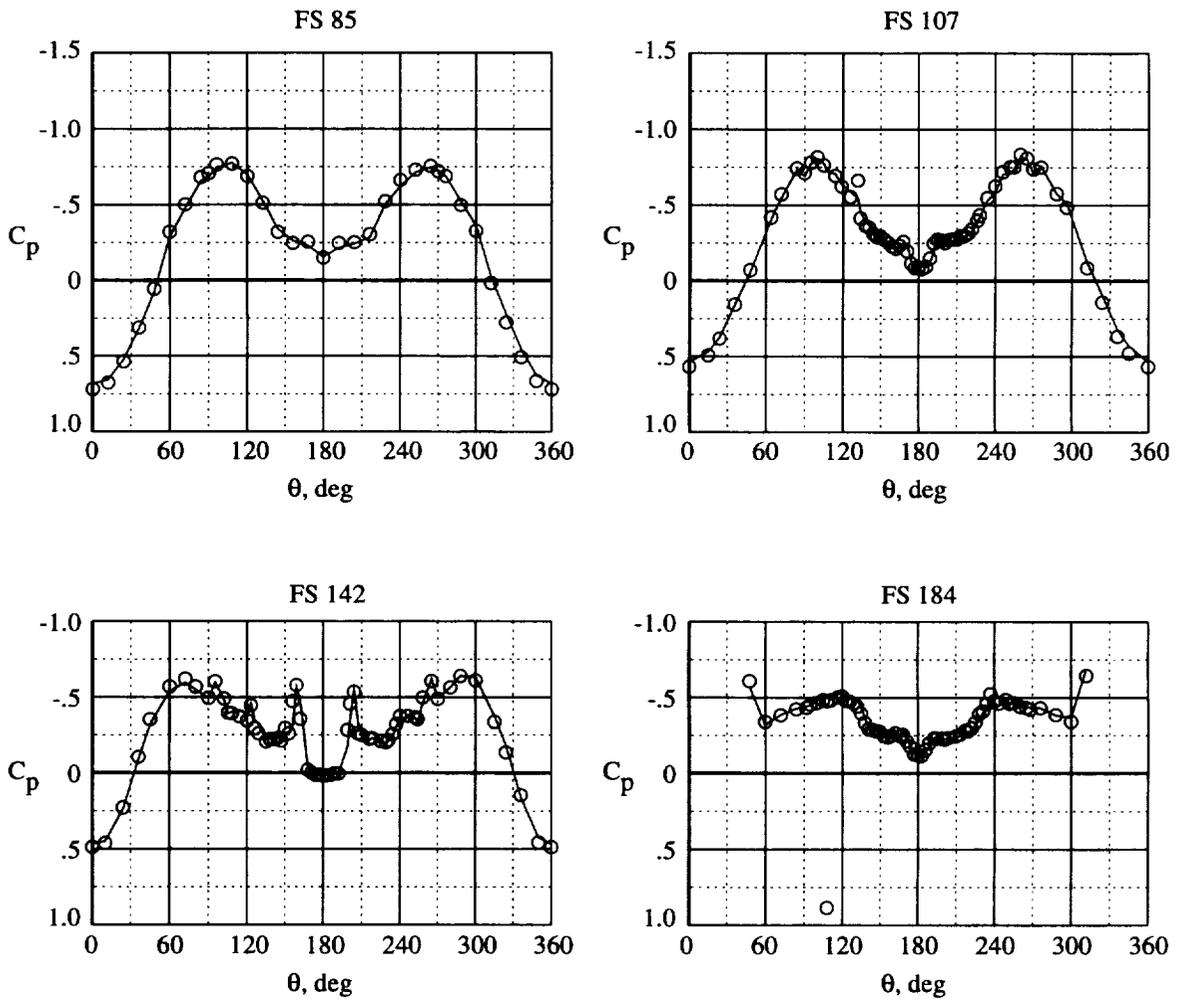
(b) $\alpha = 35°$; $\beta = 0°$.

Figure 12. Continued.

36

Test	M_∞	α, deg	β, deg	$Re_{\bar{c}}$	Grit	Interpolated
——————	Flight	0.25	39.7	-0.3	9.57×10^6	No grit	No
o	Flight	0.29	40.2	-0.2	7.87×10^6	No grit	No

(c) $\alpha = 40°$; $\beta = 0°$.

Figure 12. Continued.

37

	Test	M_∞	α, deg	β, deg	$Re_{\bar{c}}$	Grit	Interpolated
———	Flight	0.25	39.9	-4.4	8.84×10^6	No grit	No
o	Flight	0.30	39.3	-4.3	8.33×10^6	No grit	No

FS 85

FS 107

FS 142

FS 184
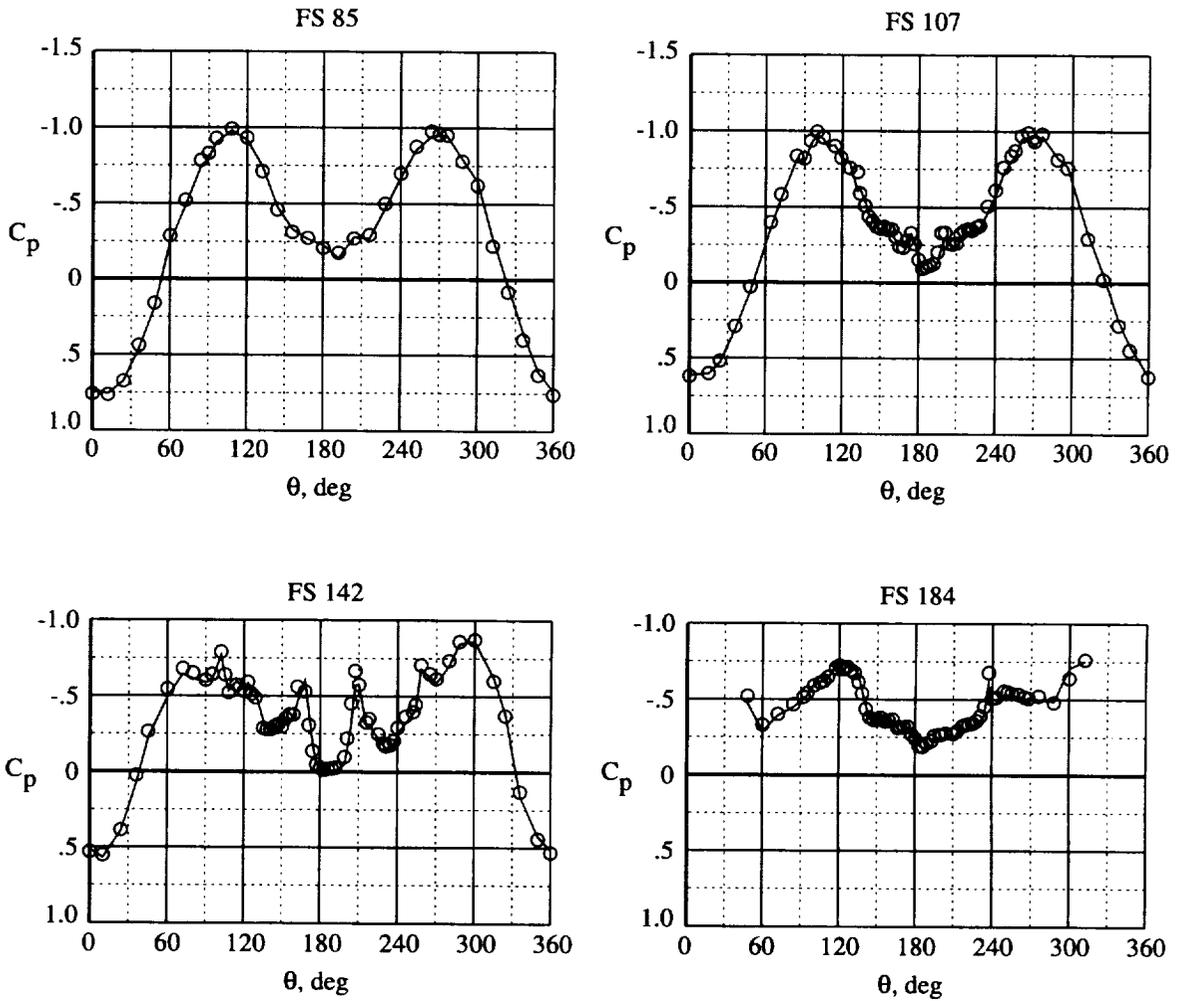
(d) $\alpha = 40°$; $\beta = -4°$.

Figure 12. Continued.

Test		M_∞	α, deg	β, deg	$Re_{\bar{c}}$	Grit	Interpolated
——————	Flight	0.24	39.4	-8.1	9.56×10^6	No grit	No
o	Flight	0.30	39.5	-8.6	8.46×10^6	No grit	No

(e) $\alpha = 40°$; $\beta = -8°$.

Figure 12. Concluded.

Test	M_∞	α, deg	β, deg	$Re_{\bar{c}}$	Grit	Interpolated
———	Flight 0.27	30.2	0.2	10.30×10^6	No grit	No
○	Flight 0.30	29.9	-0.2	7.60×10^6	No grit	No

FS 253

FS 296

FS 357

(a) $\alpha = 30°$; $\beta = 0°$.
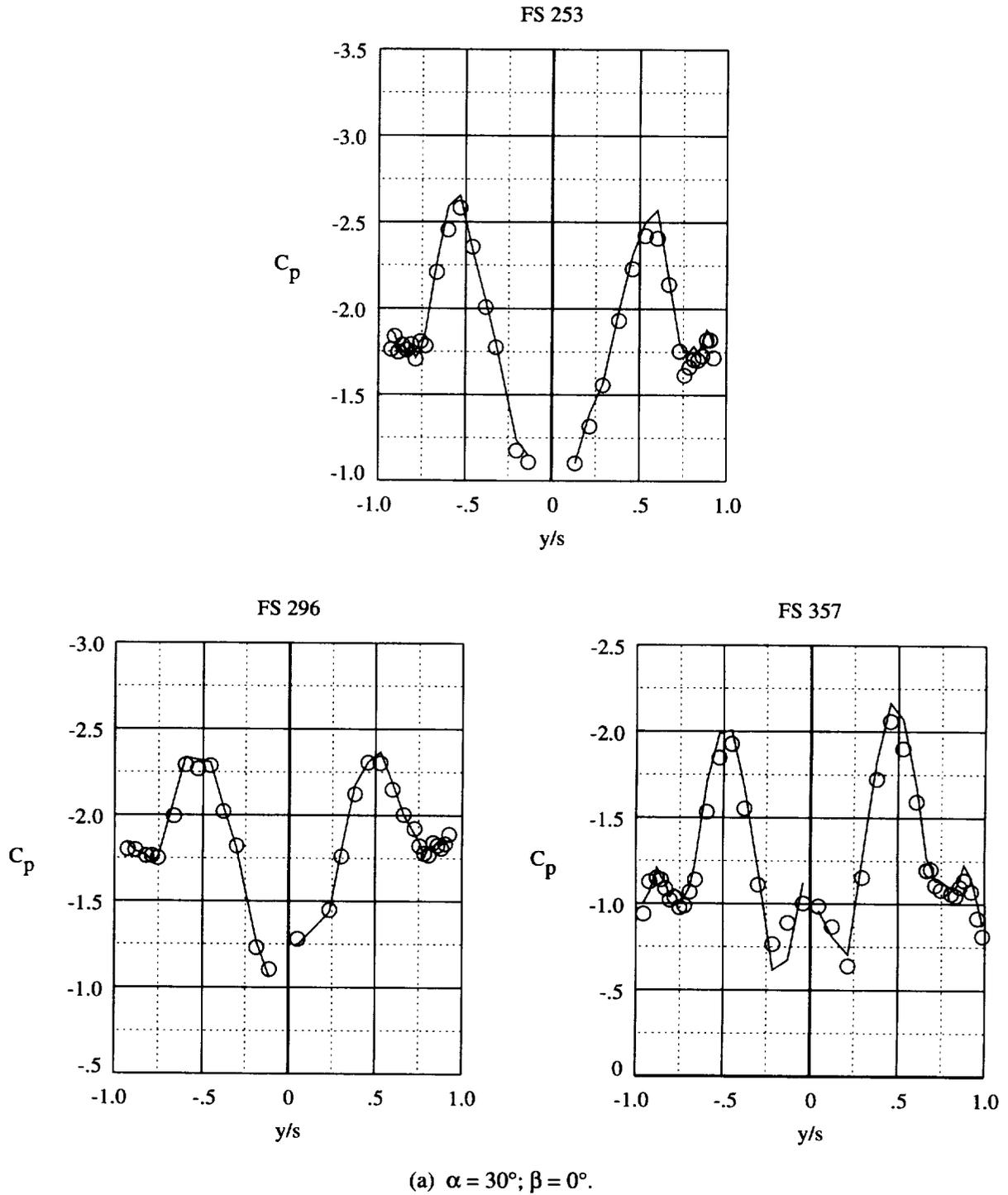
Figure 13. Repeatability for flight LEX pressure data.

Test	M_∞	α, deg	β, deg	$Re_{\bar{c}}$	Grit	Interpolated
——————	Flight	0.24	35.1	-0.5	8.88×10^6	No grit	No
O	Flight	0.32	35.5	0.0	8.66×10^6	No grit	No

FS 253
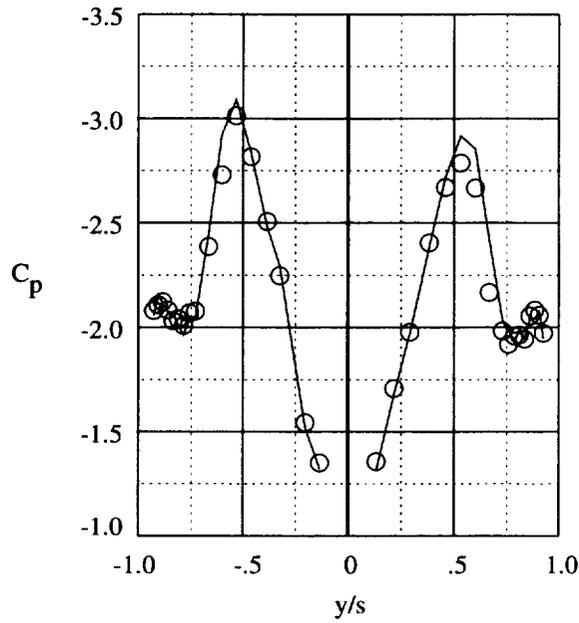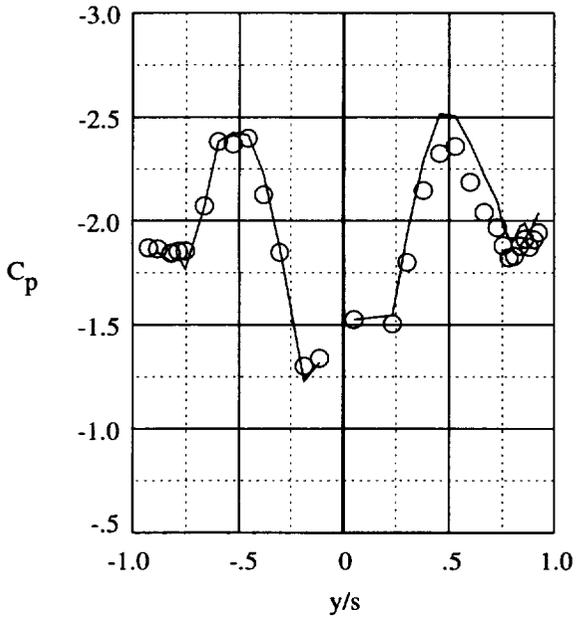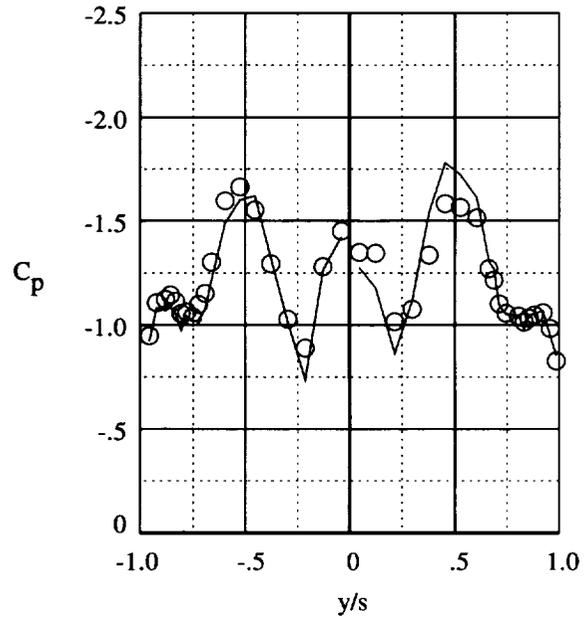
FS 296

FS 357

(b) $\alpha = 35°$; $\beta = 0°$.

Figure 13. Continued.

	Test	M_∞	α, deg	β, deg	$Re_{\bar{c}}$	Grit	Interpolated
————	Flight	0.25	39.7	-0.3	9.57×10^6	No grit	No
o	Flight	0.29	40.2	-0.2	7.87×10^6	No grit	No

FS 253
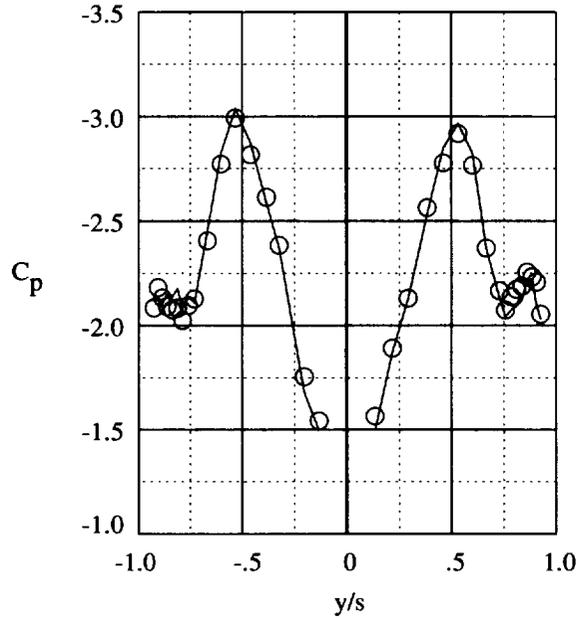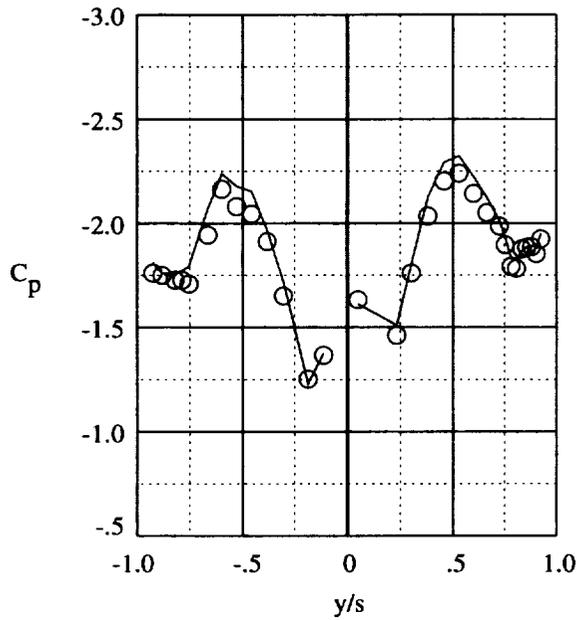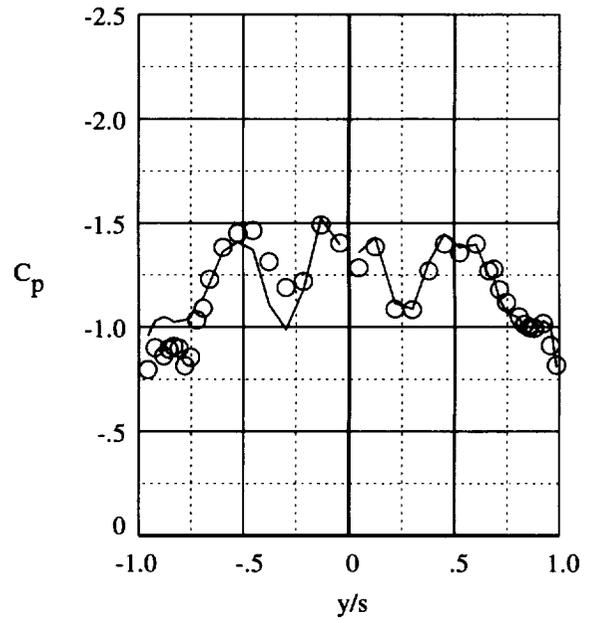
FS 296

FS 357

(c) $\alpha = 40°$; $\beta = 0°$.

Figure 13. Continued.

Test	M_∞	α, deg	β, deg	$Re_{\bar{c}}$	Grit	Interpolated
————	Flight	0.25	39.9	-4.4	8.84×10^6	No grit	No
o	Flight	0.30	39.3	-4.3	8.33×10^6	No grit	No

FS 253
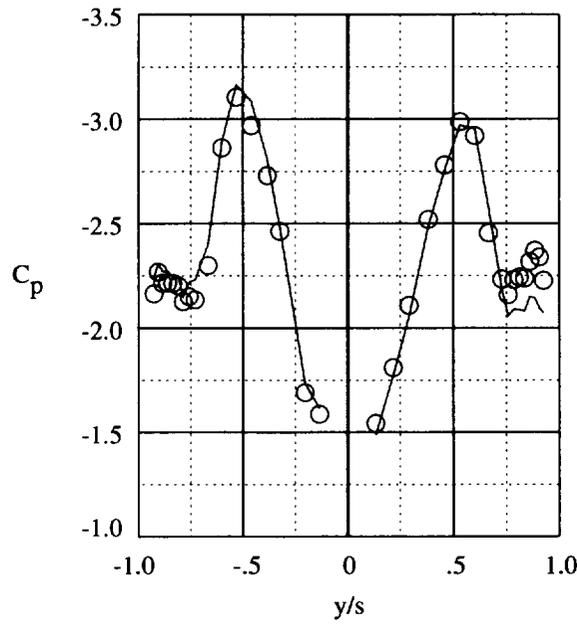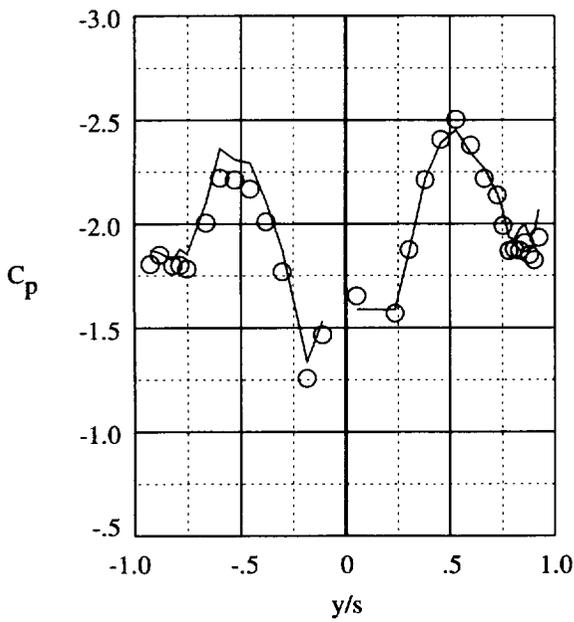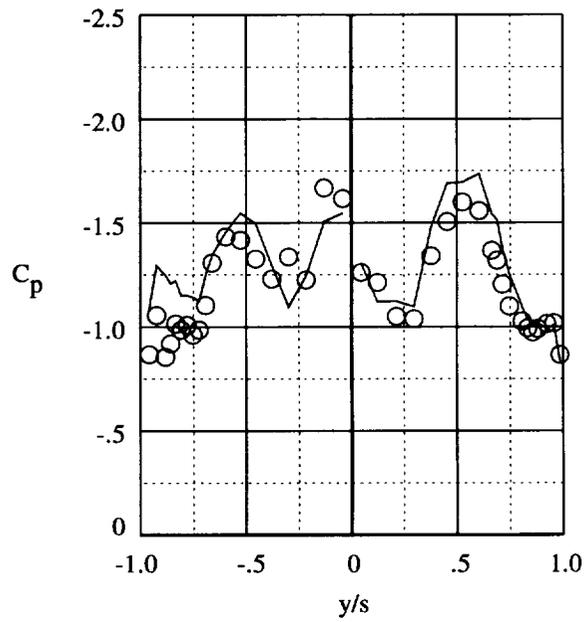
FS 296

FS 357

(d) $\alpha = 40°$; $\beta = -4°$.

Figure 13. Continued.

Test	M_∞	α, deg	β, deg	$Re_{\bar{c}}$	Grit	Interpolated
——— Flight	0.24	39.4	-8.1	9.56×10^6	No grit	No
◦ Flight	0.30	39.5	-8.6	8.46×10^6	No grit	No

FS 253
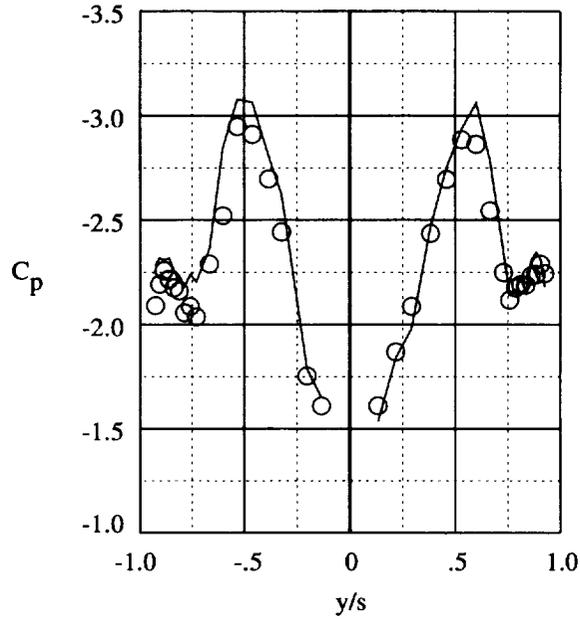
FS 296
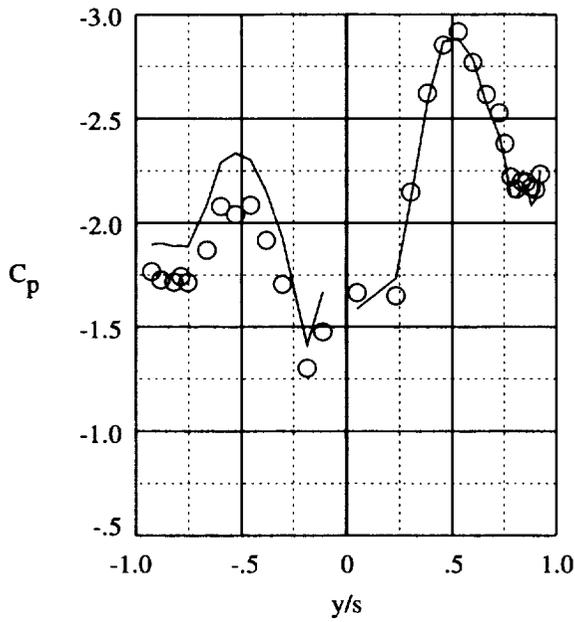
FS 357
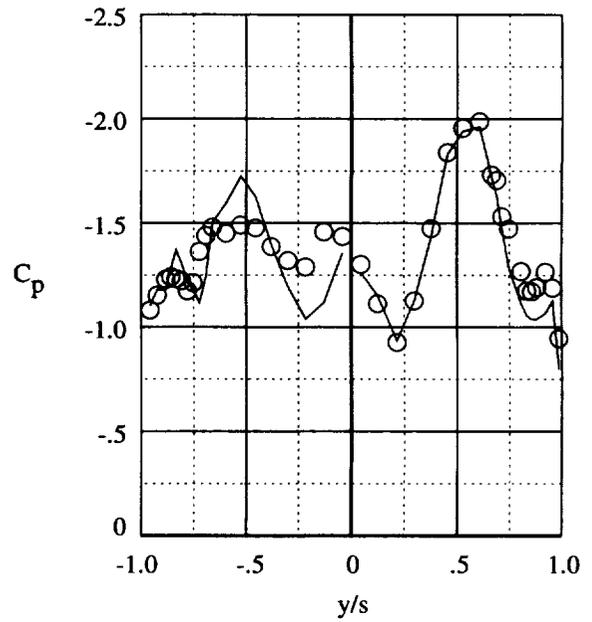
(e) $\alpha = 40°$; $\beta = -8°$.

Figure 13. Concluded.

135°   180°
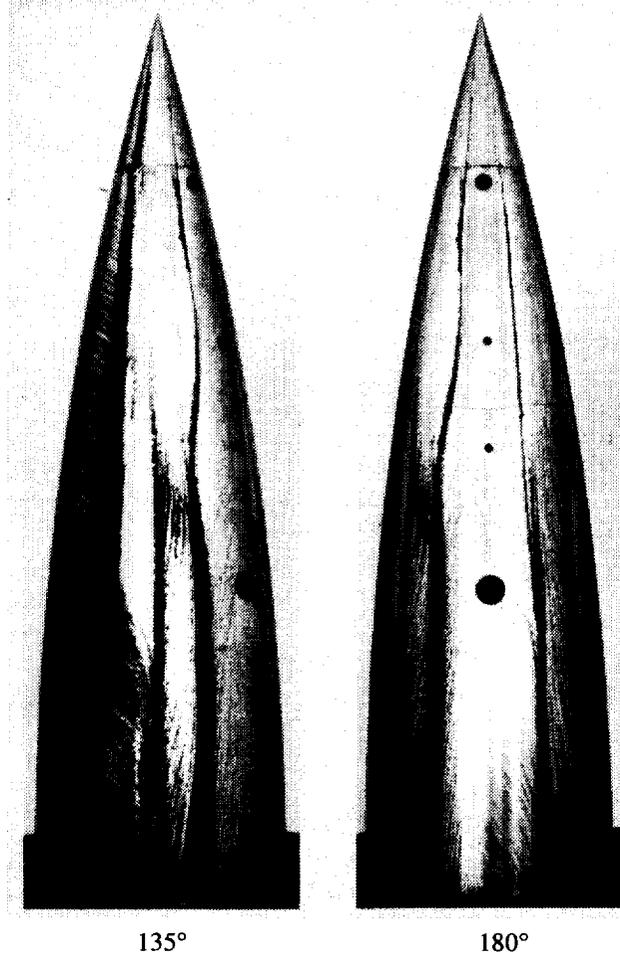
Figure 14. Oil flow photographs about 3.5-diameter tangent-ogive of Keener (ref. 14); $\alpha = 40°$; $Re_D = 0.8 \times 10^6$; 180° is leeward view; 135° is rear quarter view.

LP   TRP   TP
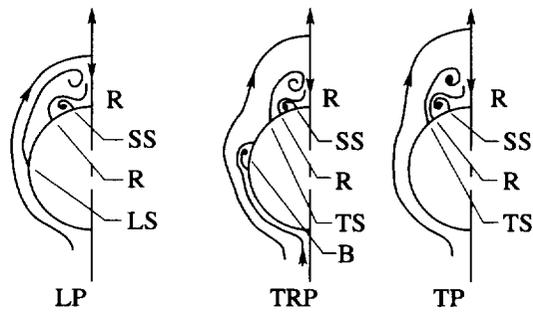
Figure 15. Keener's sketches of cross-flow patterns, same conditions as in figure 14.
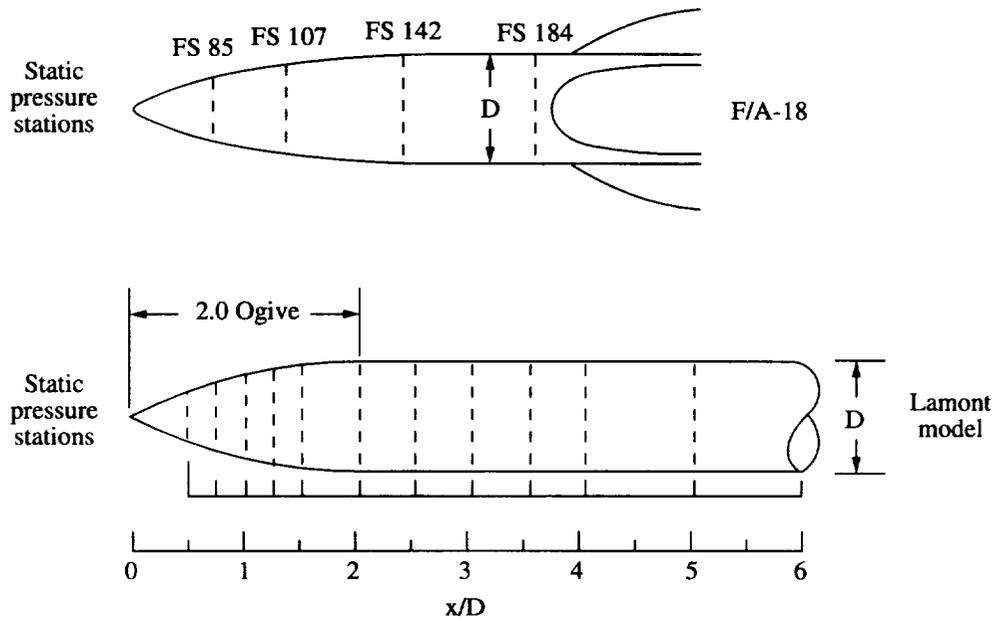
Figure 16. Similarity in planform between F/A-18 forebody and 2.0-diameter tangent-ogive-cylinder model used by Lamont (ref. 2).
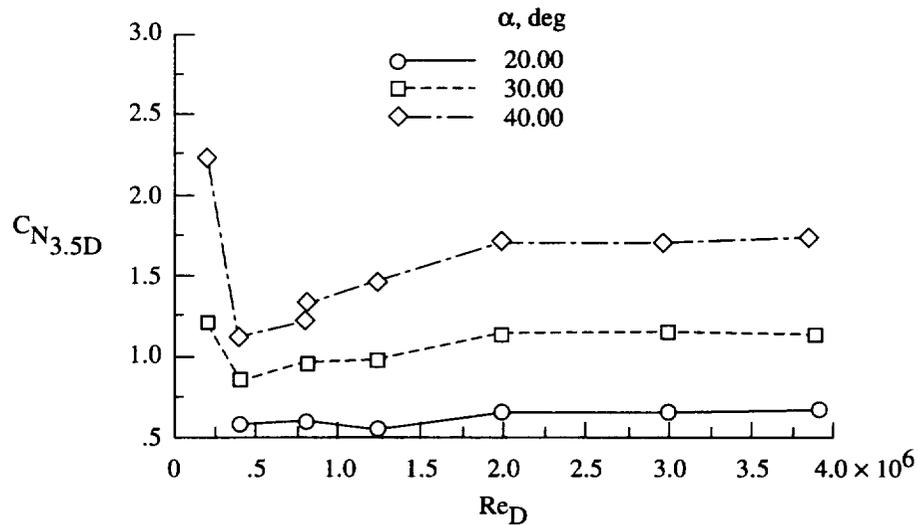
Figure 17. Influence of α and Re_D on integrated forebody normal force calculated for the first 3.5 diameters of Lamont's 2.0-diameter tangent-ogive-cylinder model.

M∞	α, deg	Re_D
——————— 0.11	20.0	0.40×10^6
‐ ‐ ‐ ‐ ‐ ‐ ‐ 0.28	20.0	2.99×10^6
o 0.28	20.0	3.90×10^6

Lamont station 0.75, similar to F/A-18 FS 85

Lamont station 1.25, similar to F/A-18 FS 107

Lamont station 2.50, similar to F/A-18 FS 142

Lamont station 4.00, similar to F/A-18 FS 184
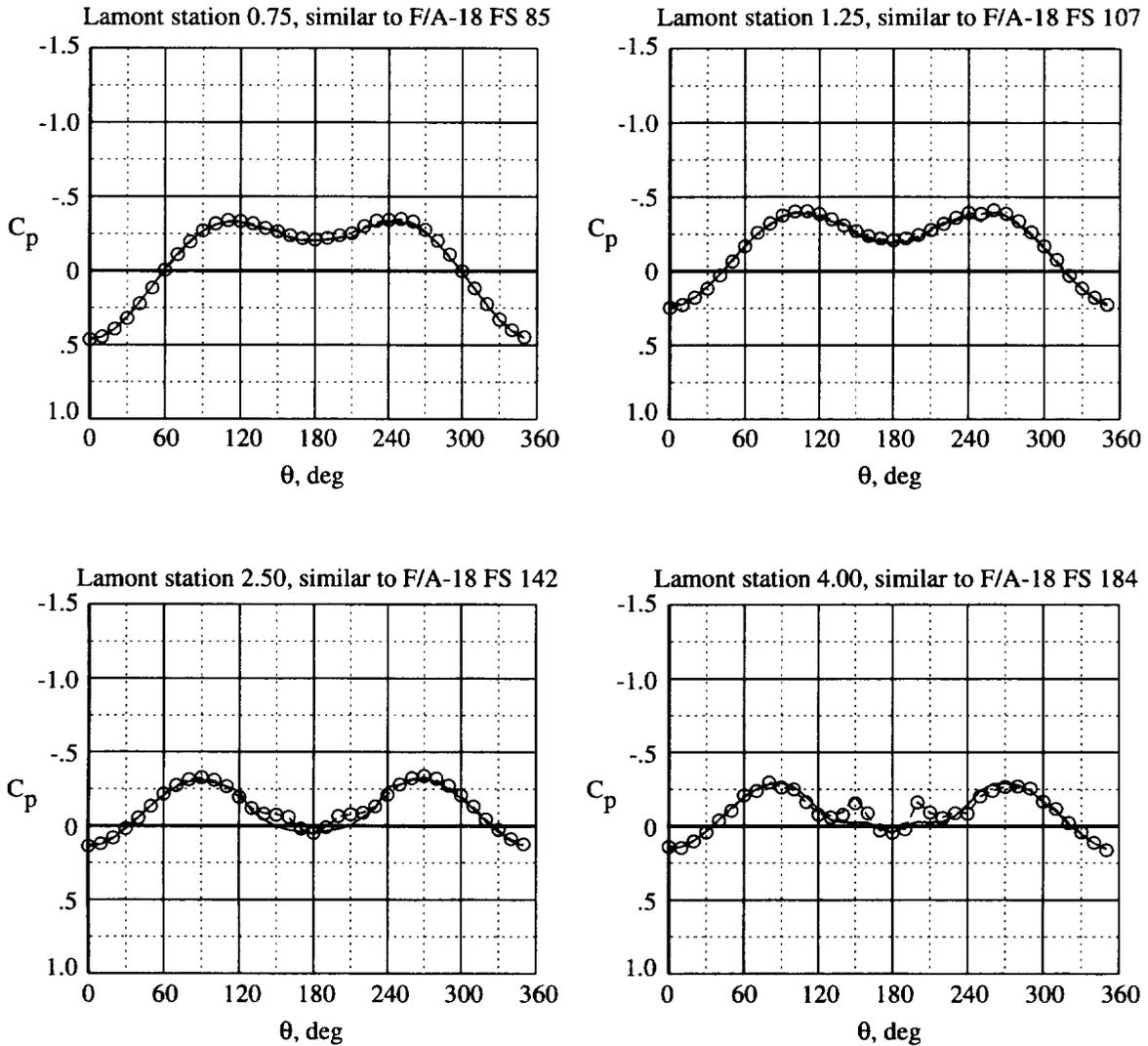
(a) α = 20°.

Figure 18. Reynolds number effects measured by Lamont (ref. 2) with 2.0-diameter tangent-ogive-cylinder.

47

M_∞	α, deg	Re_D
0.11	30.0	0.40×10^6
0.28	30.0	2.99×10^6
0.28	30.0	3.89×10^6

Lamont station 0.75, similar to F/A-18 FS 85

Lamont station 1.25, similar to F/A-18 FS 107

Lamont station 2.50, similar to F/A-18 FS 142

Lamont station 4.00, similar to F/A-18 FS 184
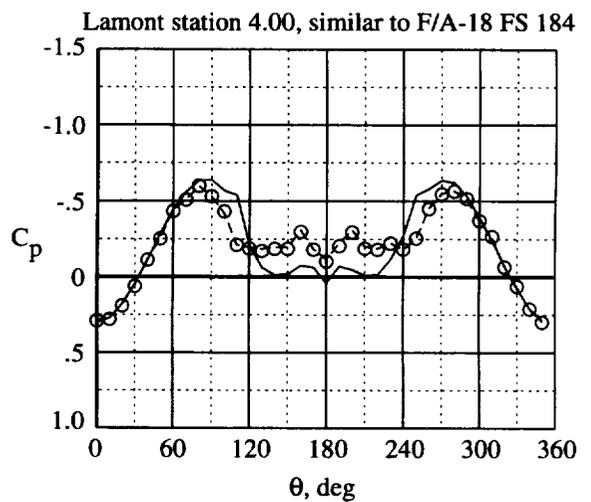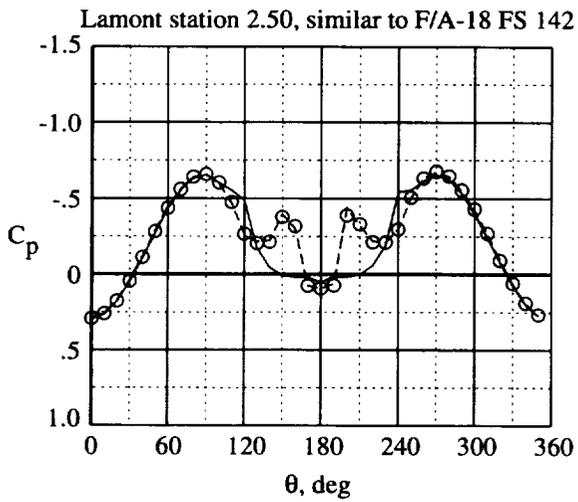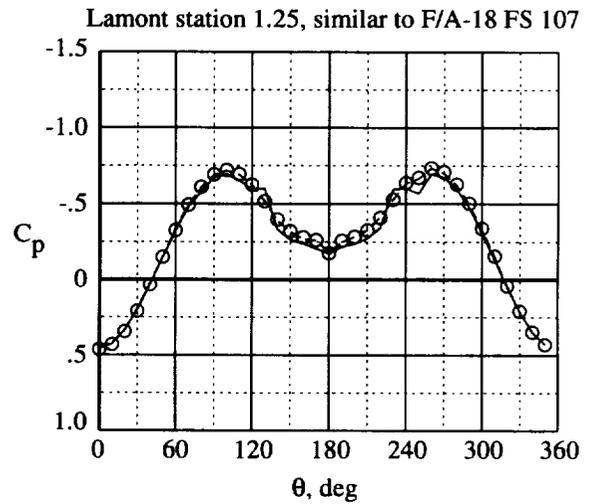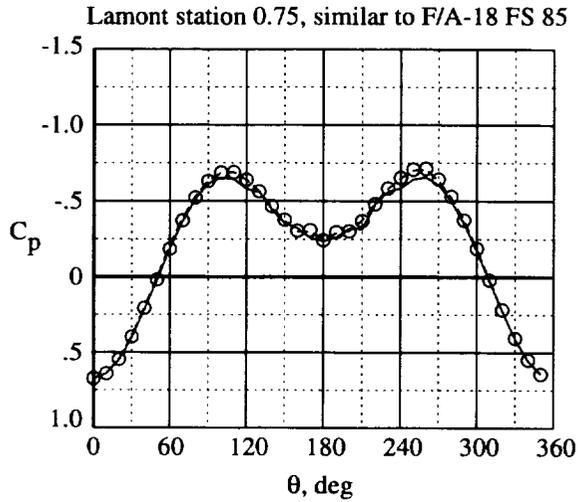
(b) $\alpha = 30°$.

Figure 18. Continued.

48

	M_∞	α, deg	Re_D
———	0.11	40.0	0.40×10^6
- - - - - -	0.28	40.0	2.97×10^6
o	0.27	40.0	3.84×10^6

Lamont station 0.75, similar to F/A-18 FS 85

Lamont station 1.25, similar to F/A-18 FS 107

Lamont station 2.50, similar to F/A-18 FS 142

Lamont station 4.00, similar to F/A-18 FS 184
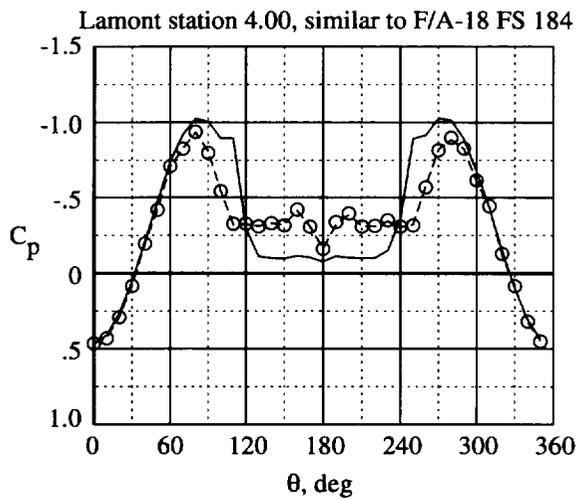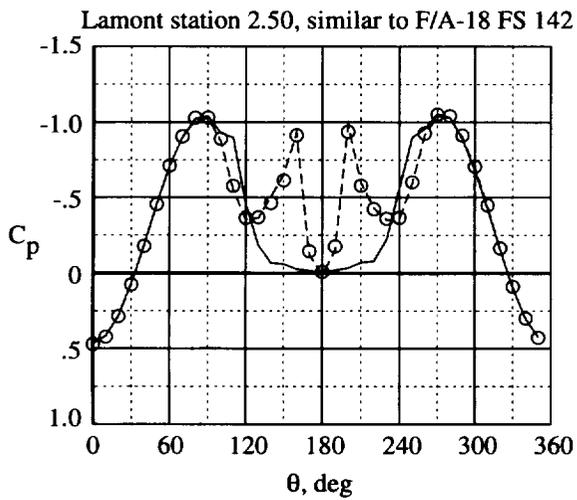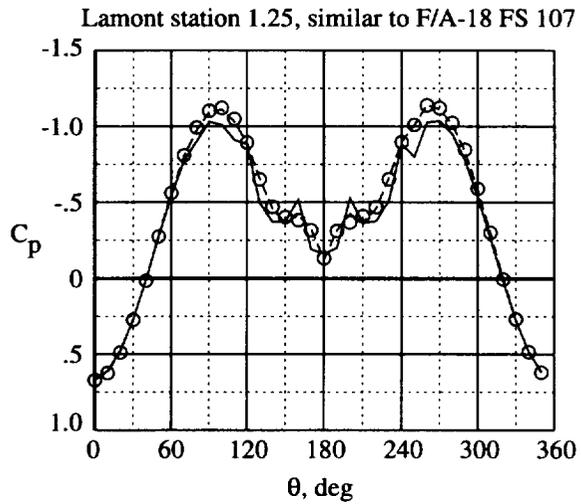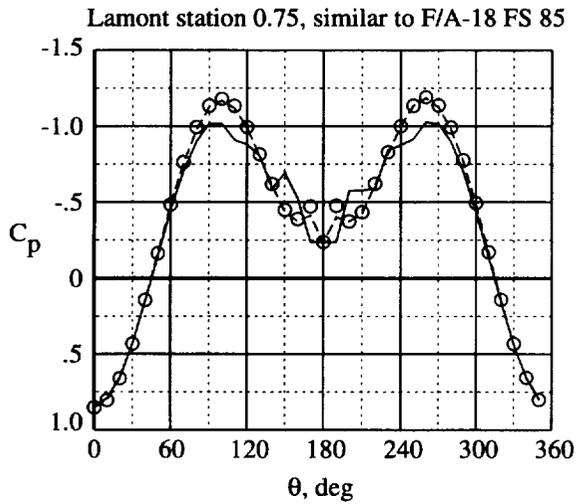
(c) $\alpha = 40°$.

Figure 18. Concluded.
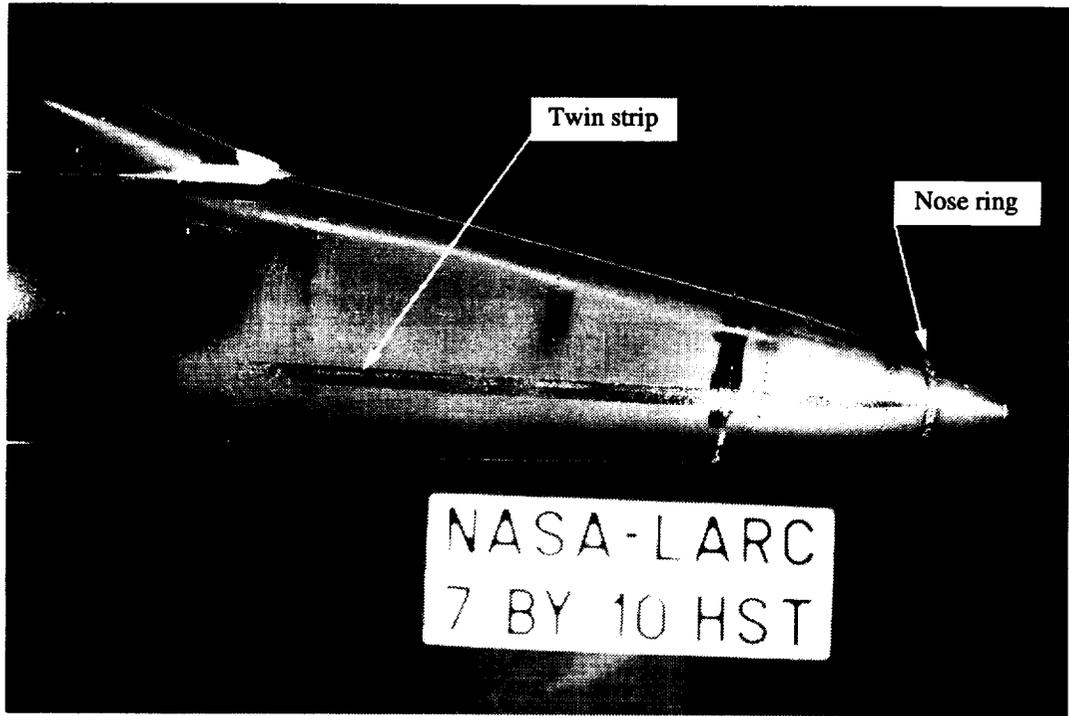
(a) Photograph of baseline, high-α gritting pattern.

Pressure stations
FS 184

FS 142

FS 107

FS 85   FS 70
         (inactive)

0.25 in.

0.13 in.

Longitudinal strip, No. 180 grit

Nose ring, No. 90 grit
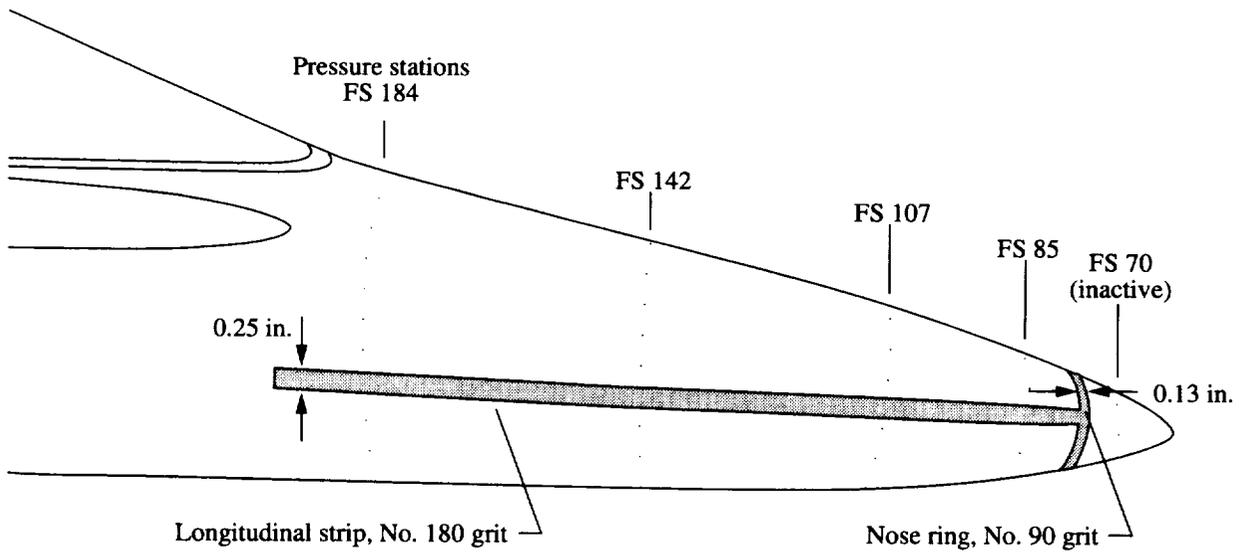
(b) Schematic of baseline, high-α gritting pattern.

Figure 19. Gritting patterns used with 0.06-scale model.
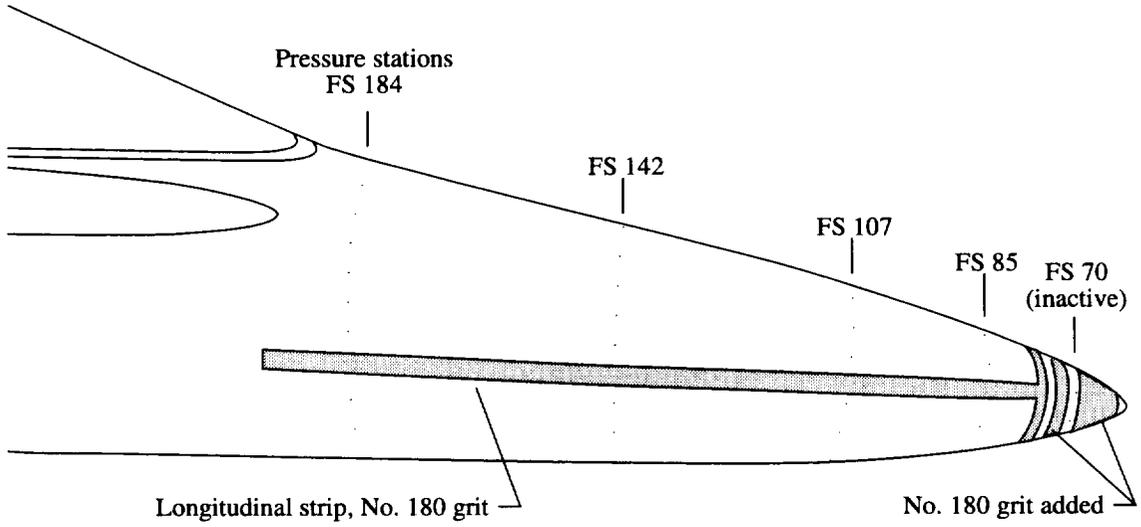
(c) Schematic of baseline plus frontal grit pattern.
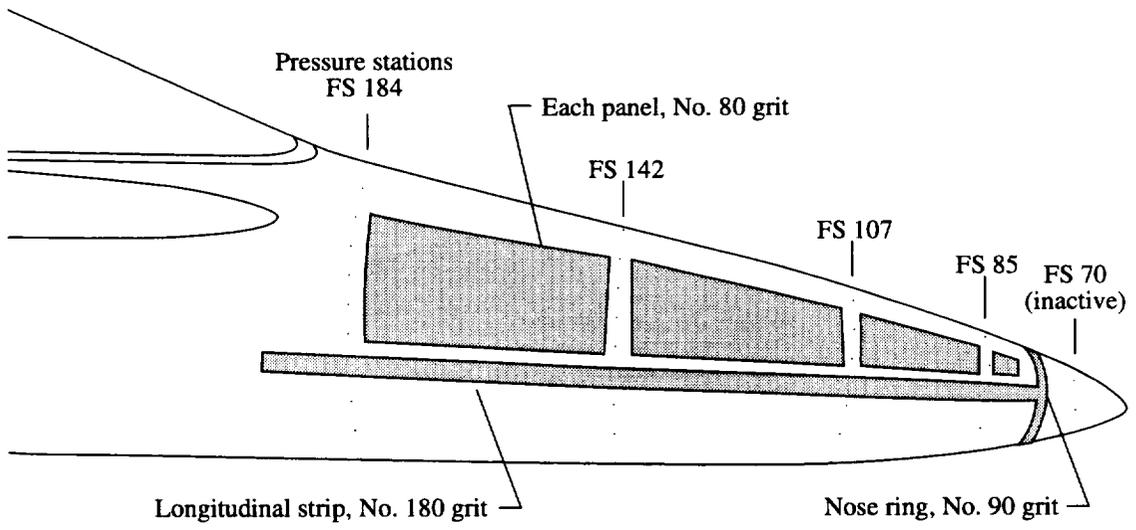
(d) Schematic of baseline plus side panels of grit pattern.

Figure 19. Continued.

51
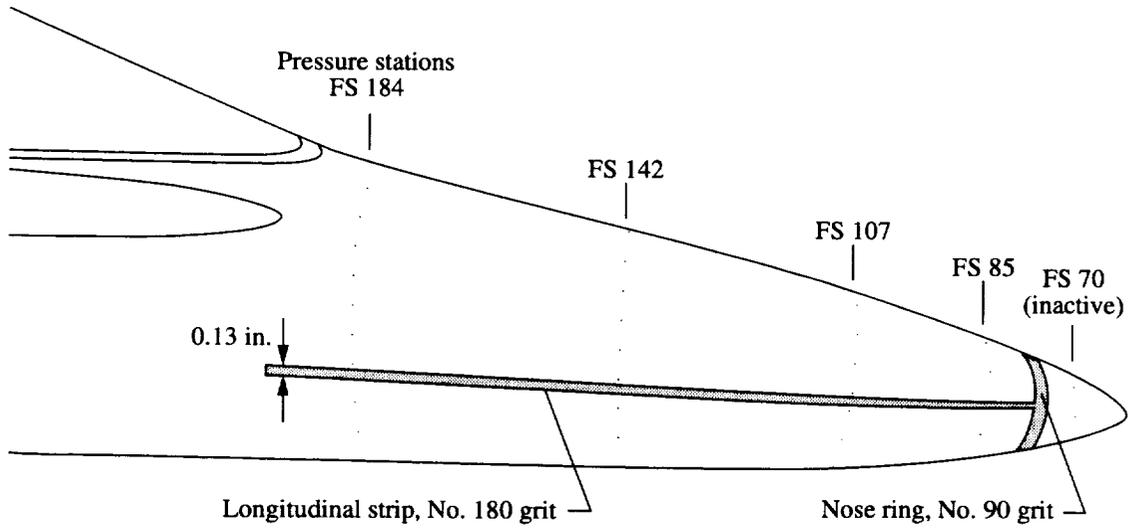
(e) Schematic of baseline with narrower strips pattern.
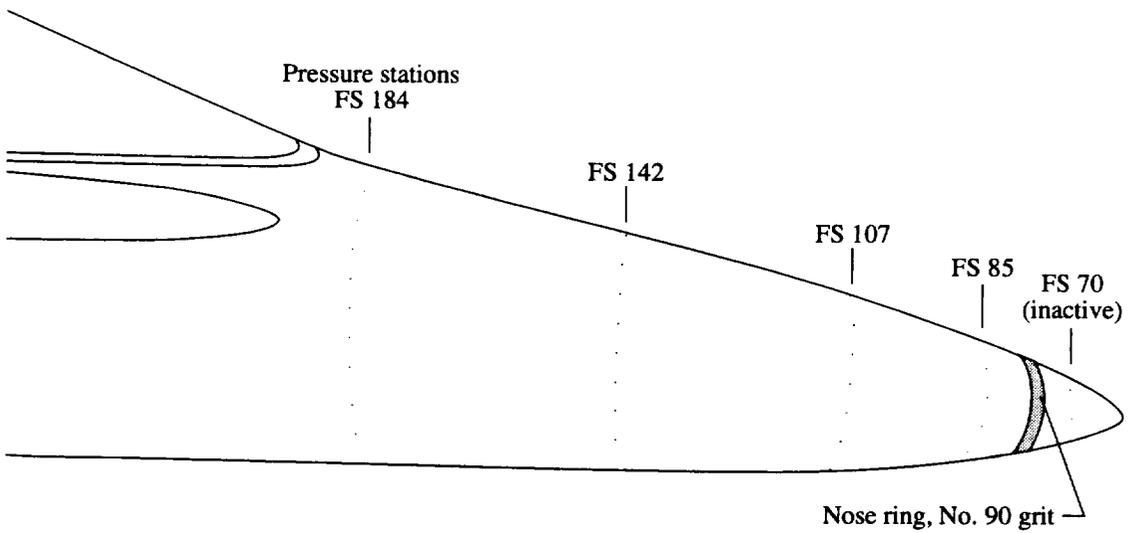
(f) Schematic of nose ring only.

Figure 19. Concluded.
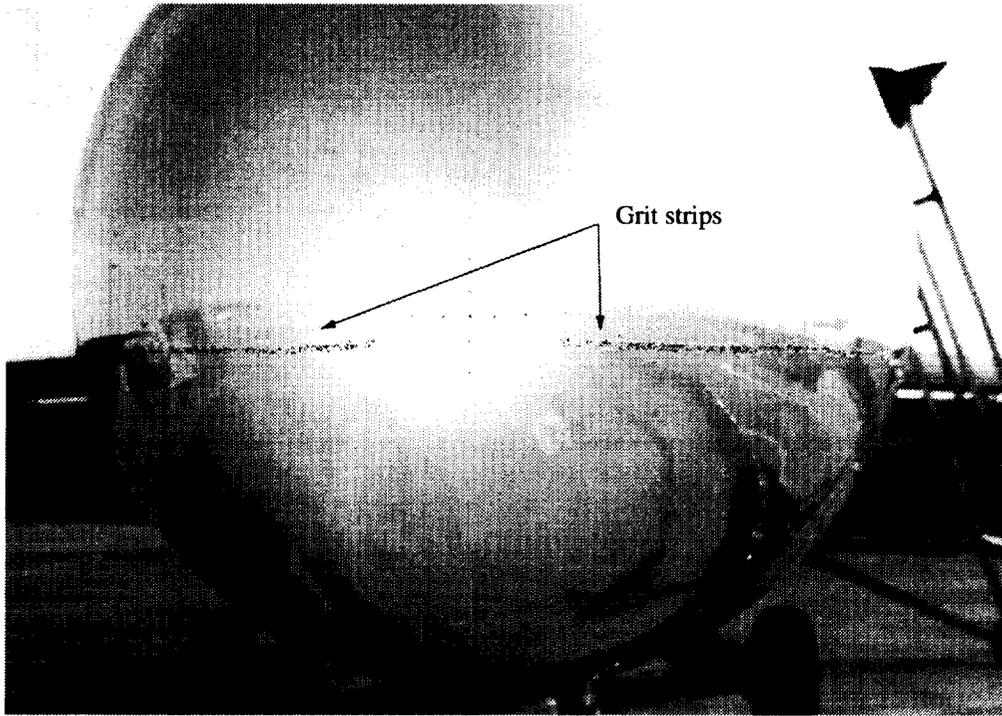
(a) Close-up photograph of gritting pattern at nose.

Pressure stations
FS 184

FS 142

FS 107

FS 85

FS 70

Longitudinal strip, No. 36 grit
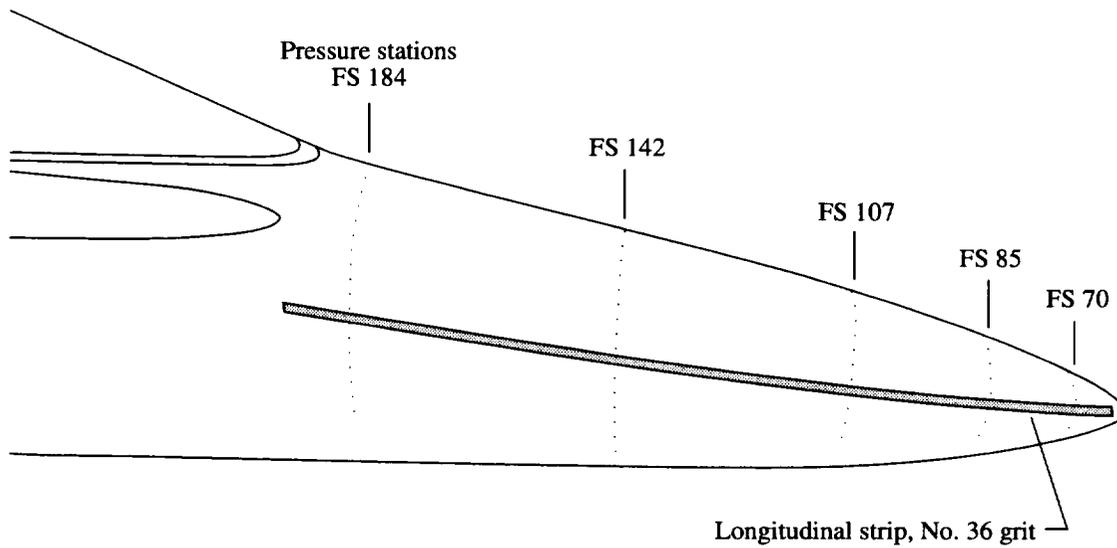
(b) Schematic of forebody gritting.

Figure 20. Gritting pattern used with the HARV.

Test	M_∞	α, deg	β, deg	$Re_{\bar{c}}$	Grit	Interpolated
————	Flight	0.24	35.1	-0.5	8.88×10^6	No grit	No
o	Flight	0.26	35.0	-0.1	10.40×10^6	Twin strips	No

(a) $\alpha = 35°$; $\beta = 0°$.

Figure 21. Comparing grit-free and gritted-flight forebody pressure data.

54

Test	M_∞	α, deg	β, deg	$Re_{\bar{c}}$	Grit	Interpolated
————	Flight	0.23	44.9	-0.2	9.31×10^6	No grit	No
o	Flight	0.26	44.7	0.0	9.43×10^6	Twin strips	No
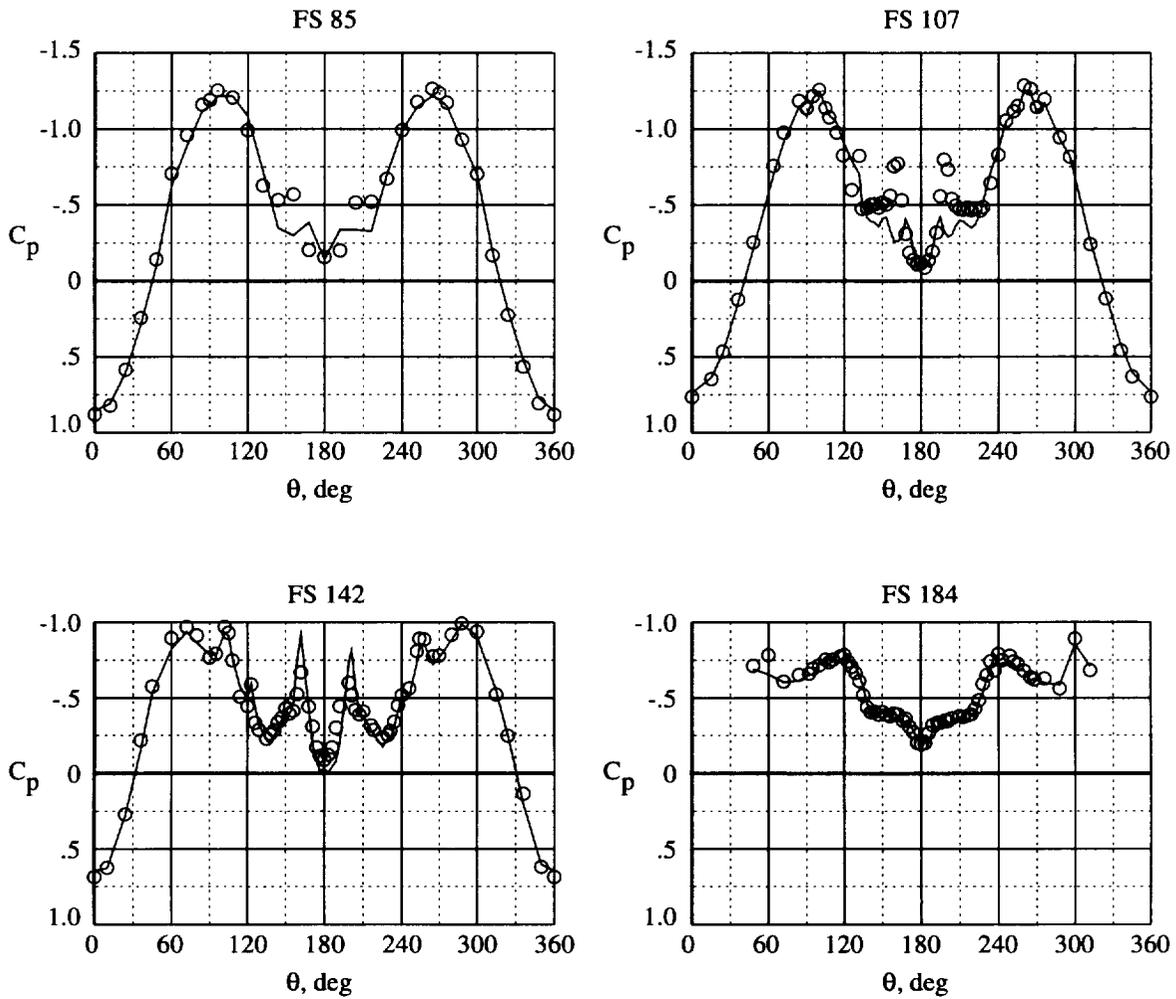
(b) $\alpha = 45°$; $\beta = 0°$.

Figure 21. Continued.

	Test	M_∞	α, deg	β, deg	$Re_{\bar{c}}$	Grit	Interpolated
———	Flight	0.23	45.1	3.8	9.19×10^6	No grit	No
o	Flight	0.26	44.7	4.0	9.80×10^6	Twin strips	No

FS 85

FS 107

FS 142

FS 184
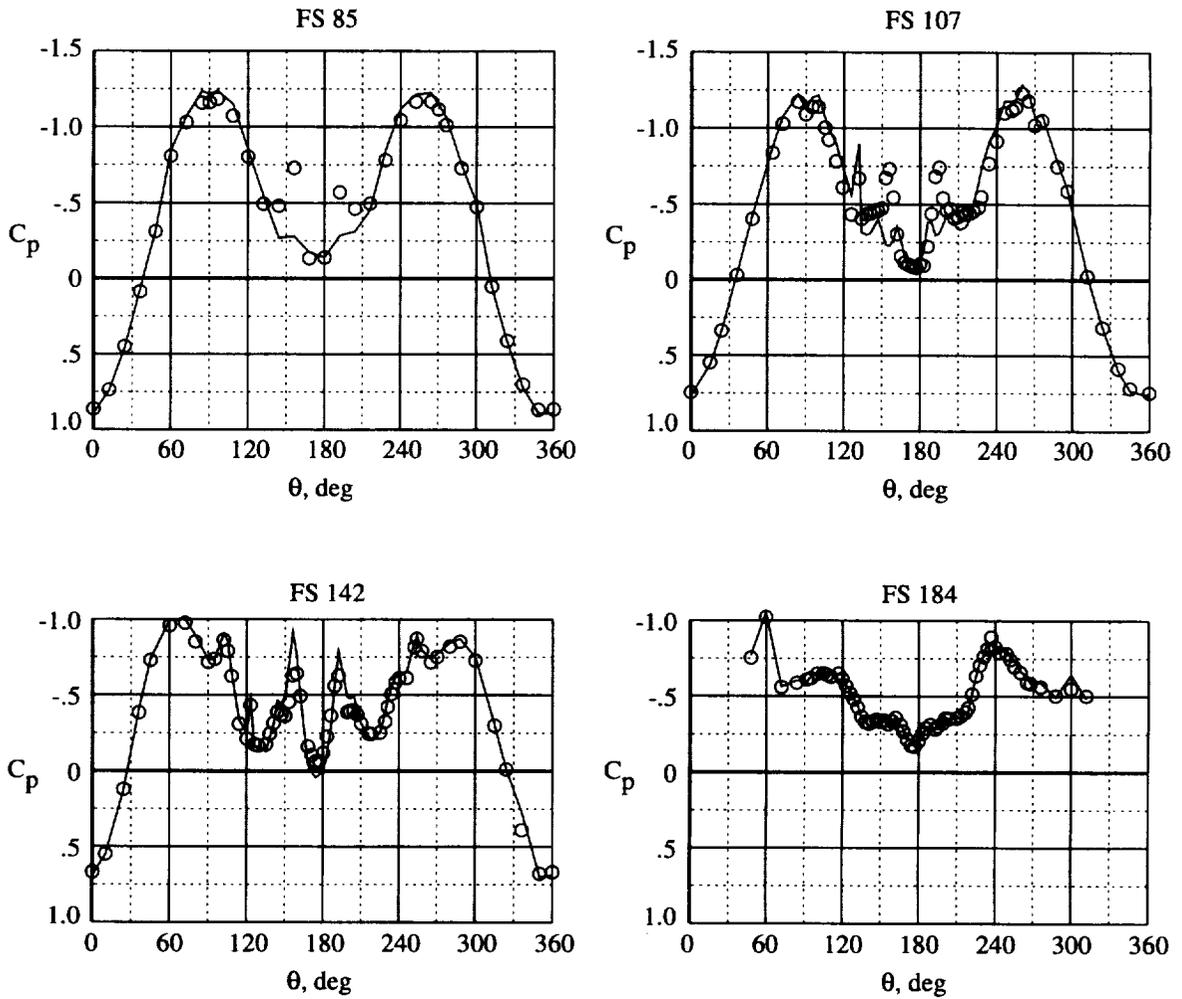
(c) $\alpha = 45°$; $\beta = 4°$.

Figure 21. Concluded.

Test	M_∞	α, deg	β, deg	$Re_{\bar{c}}$	Grit	Interpolated
Flight	0.24	35.1	-0.5	8.88×10^6	No grit	No
○ Flight	0.26	35.0	-0.1	10.40×10^6	Twin strips	No

FS 253

FS 296

FS 357

(a) $\alpha = 35°$; $\beta = 0°$.
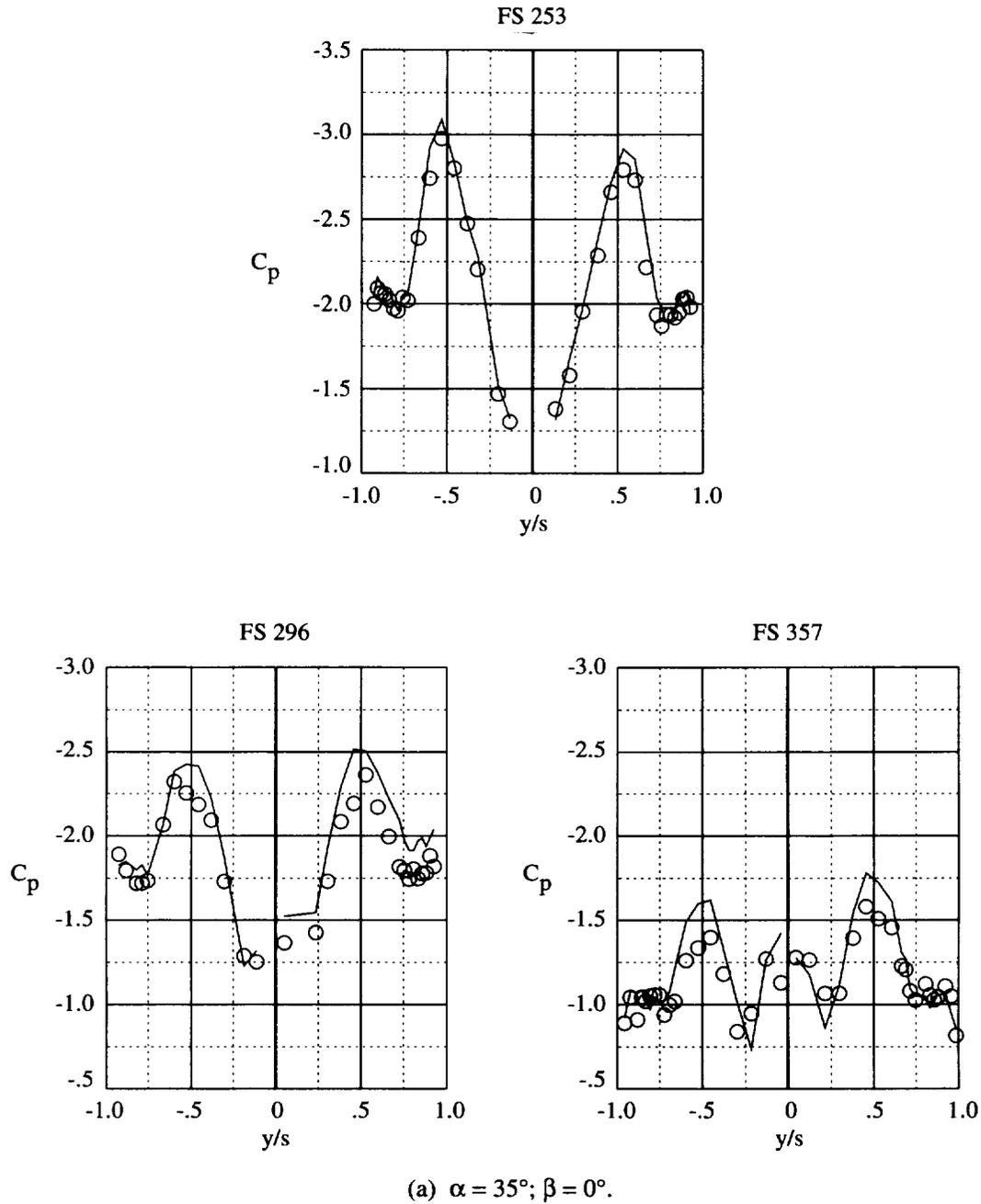
Figure 22. Comparing grit-free and gritted-flight LEX pressure data.

	Test	M_∞	α, deg	β, deg	$Re_{\bar{c}}$	Grit	Interpolated
———	Flight	0.23	44.9	-0.2	9.31×10^6	No grit	No
O	Flight	0.26	44.7	0.0	9.43×10^6	Twin strips	No

FS 253

FS 296

FS 357
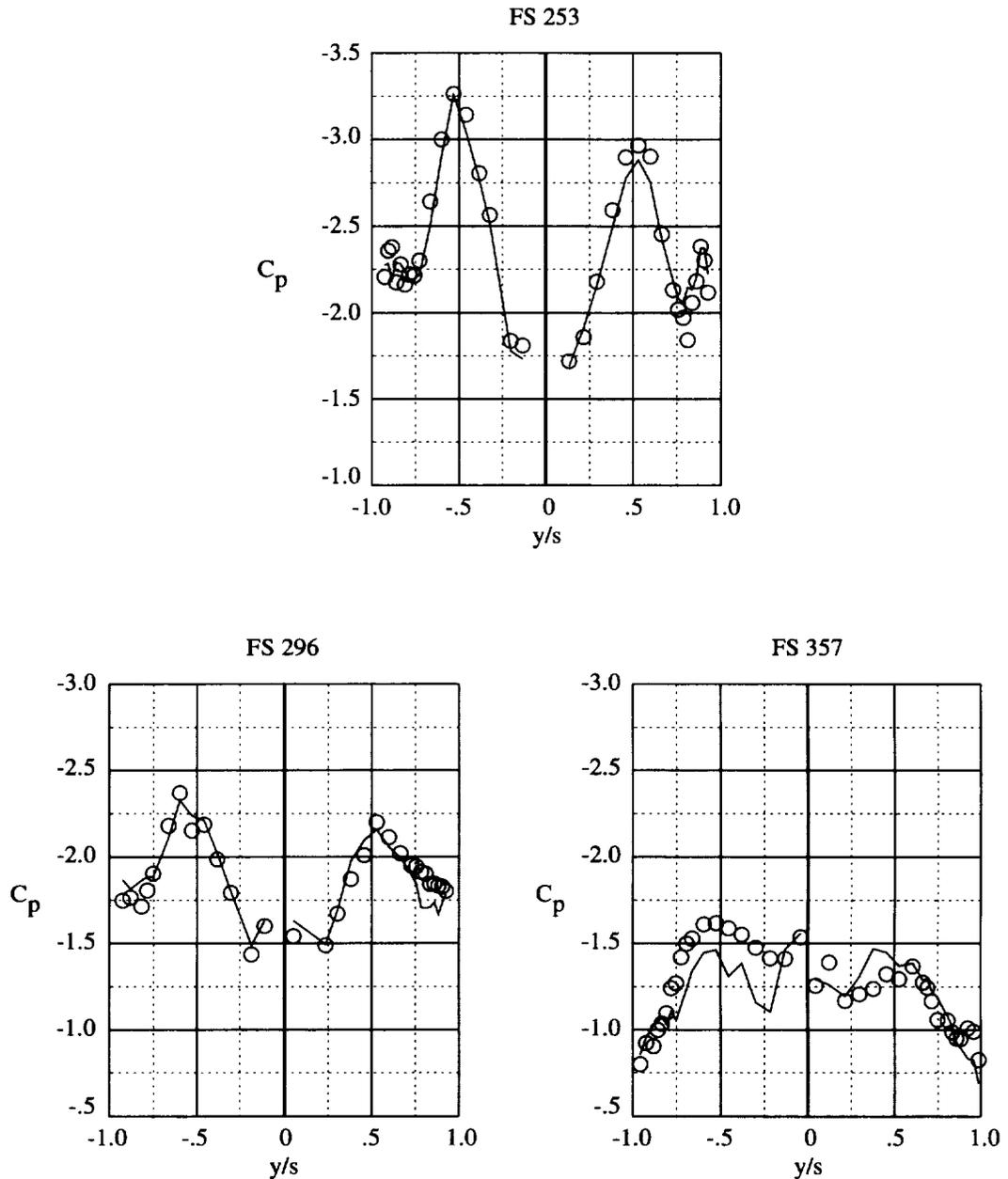
(b) $\alpha = 45°$; $\beta = 0°$.

Figure 22. Continued.

	Test	M_∞	α, deg	β, deg	$Re_{\bar{c}}$	Grit	Interpolated
————	Flight	0.23	45.1	3.8	9.19×10^6	No grit	No
O	Flight	0.26	44.7	4.0	9.80×10^6	Twin strips	No

FS 253

FS 296

FS 357
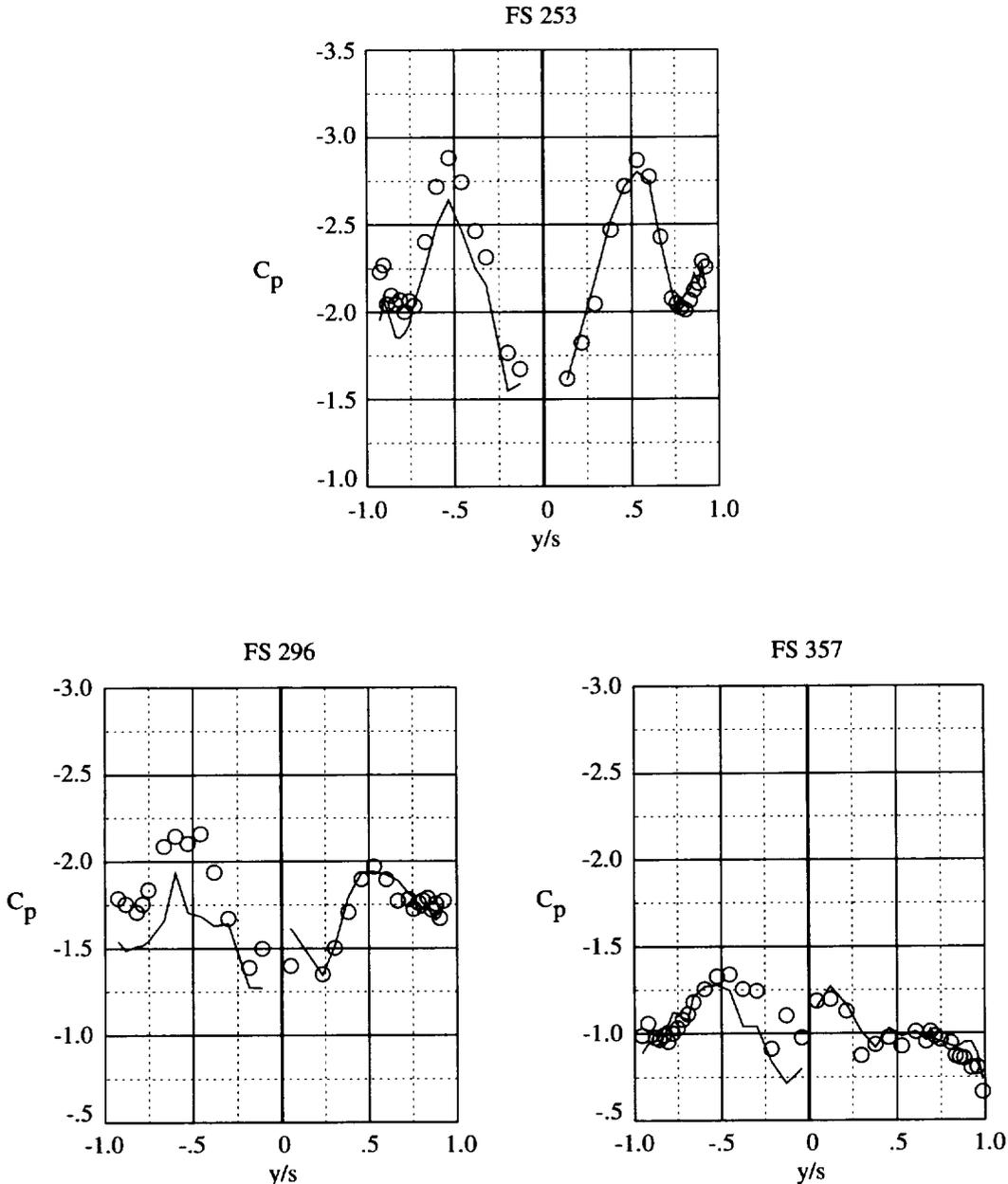
(c) $\alpha = 45°$; $\beta = 4°$.

Figure 22. Concluded.

Test	M_∞	α, deg	β, deg	$Re_{\bar{c}}$	Grit	Interpolated
————	7×10	0.30	20.0	0.1	1.41×10^6	Baseline	Yes
– – – – –	7×10	0.30	20.0	0.0	1.36×10^6	Nose ring	Yes
o	Flight	0.30	20.0	-0.3	12.70×10^6	No grit	No
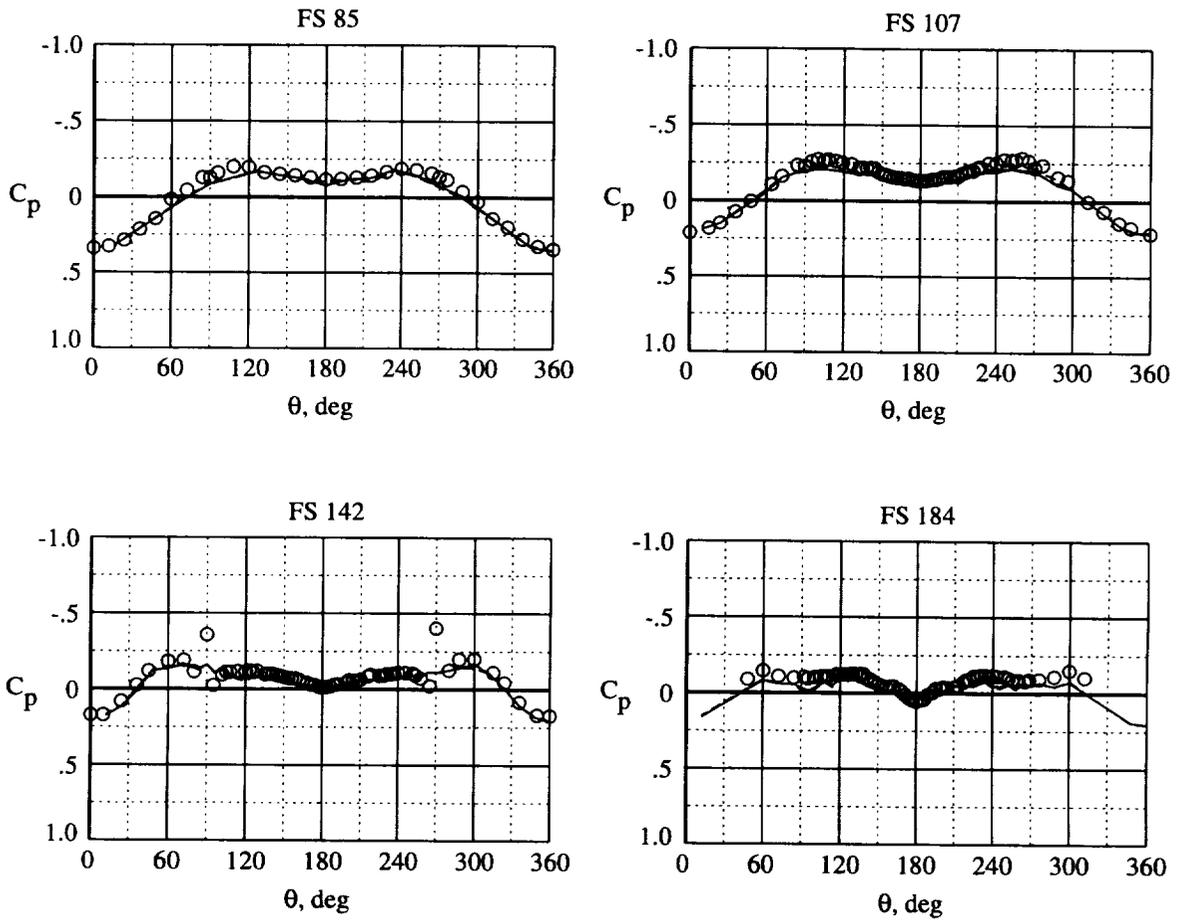
(a) $\alpha = 20°$; $\beta = 0°$.

Figure 23. Comparing tunnel forebody pressure data with either baseline grit pattern or nose-ring-only pattern to flight data without grit.

	Test	M_∞	α, deg	β, deg	$Re_{\bar{c}}$	Grit	Interpolated
———————	7 × 10	0.30	30.0	0.1	1.40×10^6	Baseline	Yes
- - - - - - -	7 × 10	0.30	30.0	0.0	1.37×10^6	Nose ring	Yes
o	Flight	0.27	30.2	0.2	10.30×10^6	No grit	No

FS 85

FS 107

FS 142

FS 184

(b) $\alpha = 30°$; $\beta = 0°$.

Figure 23. Continued.

61

Test	M_∞	α, deg	β, deg	$Re_{\bar{c}}$	Grit	Interpolated
———————	7 × 10	0.30	35.0	0.1	1.39×10^6	Baseline	Yes
– – – – – – –	7 × 10	0.30	35.0	0.0	1.37×10^6	Nose ring	Yes
○	Flight	0.24	35.1	-0.5	8.88×10^6	No grit	No

(c) $\alpha = 35°$; $\beta = 0°$.

Figure 23. Continued.

62

Test	M_∞	α, deg	β, deg	$Re_{\bar{c}}$	Grit	Interpolated
————	7 × 10	0.30	40.0	0.1	1.39×10^6	Baseline	Yes
– – – – –	7 × 10	0.30	40.0	0.0	1.36×10^6	Nose ring	Yes
○	Flight	0.25	39.7	-0.3	9.57×10^6	No grit	No
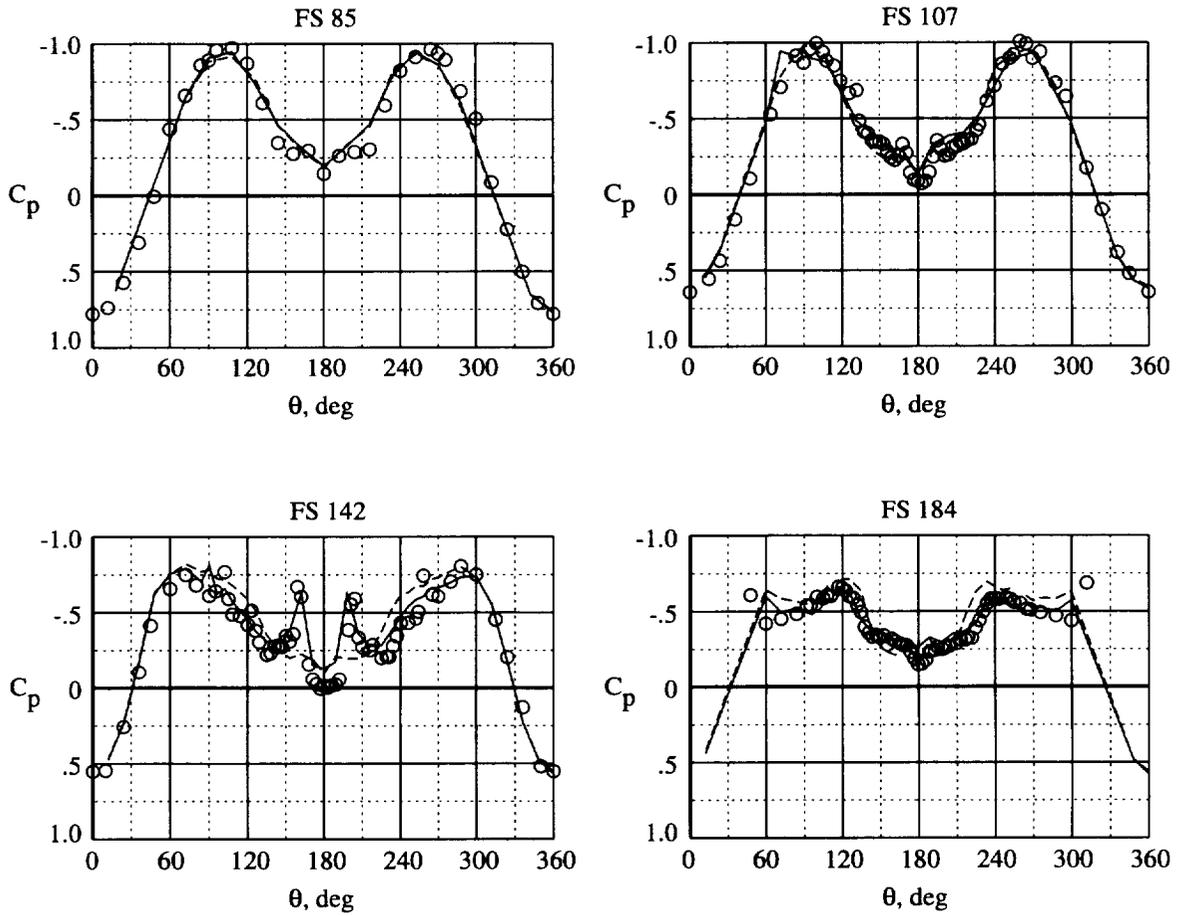
(d) $\alpha = 40°$; $\beta = 0°$.

Figure 23. Continued.

Test	M_∞	α, deg	β, deg	$Re_{\bar{c}}$	Grit	Interpolated
————	7 × 10	0.30	40.0	4.0	1.39×10^6	Baseline	Yes
- - - - -	7 × 10	0.30	40.0	4.0	1.36×10^6	Nose ring	Yes
○	Flight	0.22	39.9	3.9	8.23×10^6	No grit	No

FS 85

FS 107

FS 142

FS 184
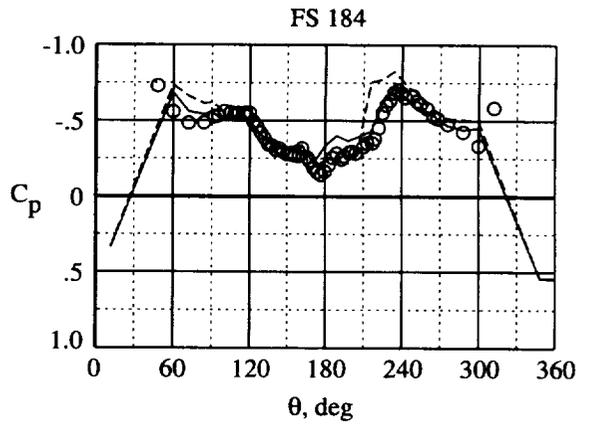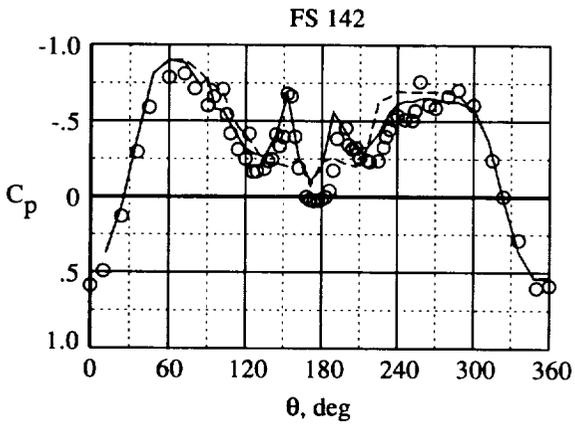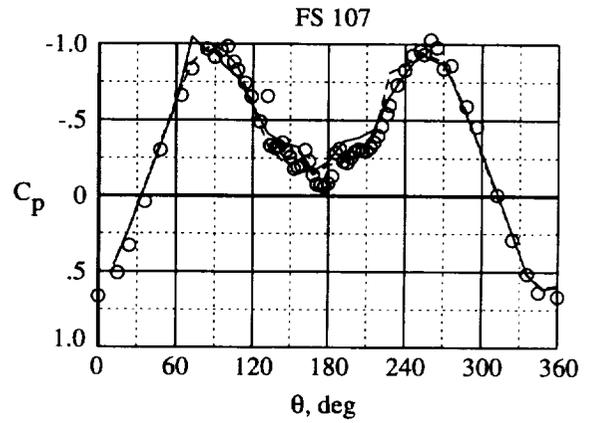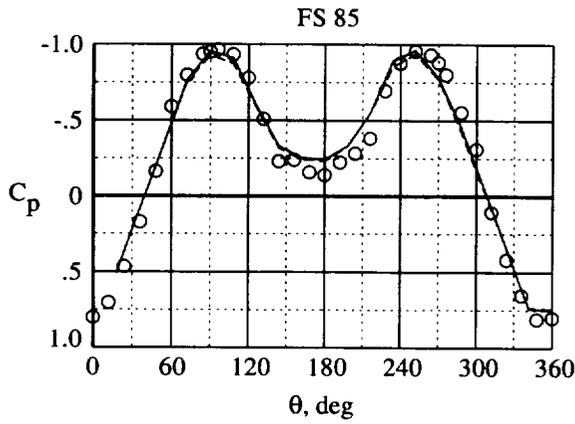
(e) $\alpha = 40°$; $\beta = 4°$.

Figure 23. Continued.

64

Test	M_∞	α, deg	β, deg	$Re_{\bar{c}}$	Grit	Interpolated
————	7 × 10	0.30	40.0	8.0	1.39×10^6	Baseline	Yes
——-——-	7 × 10	0.30	40.0	8.0	1.36×10^6	Nose ring	Yes
o	Flight	0.26	40.4	7.5	9.97×10^6	No grit	No

(f) $\alpha = 40°$; $\beta = 8°$.

Figure 23. Concluded.

Test	M_∞	α, deg	β, deg	$Re_{\bar{c}}$	Grit	Interpolated
——————— 7×10	0.30	20.0	0.1	1.41×10^6	Baseline	Yes
- - - - - - - - 7×10	0.30	20.0	0.0	1.36×10^6	Nose ring	Yes
O Flight	0.30	20.0	-0.3	12.70×10^6	No grit	No

FS 253

FS 296

FS 357
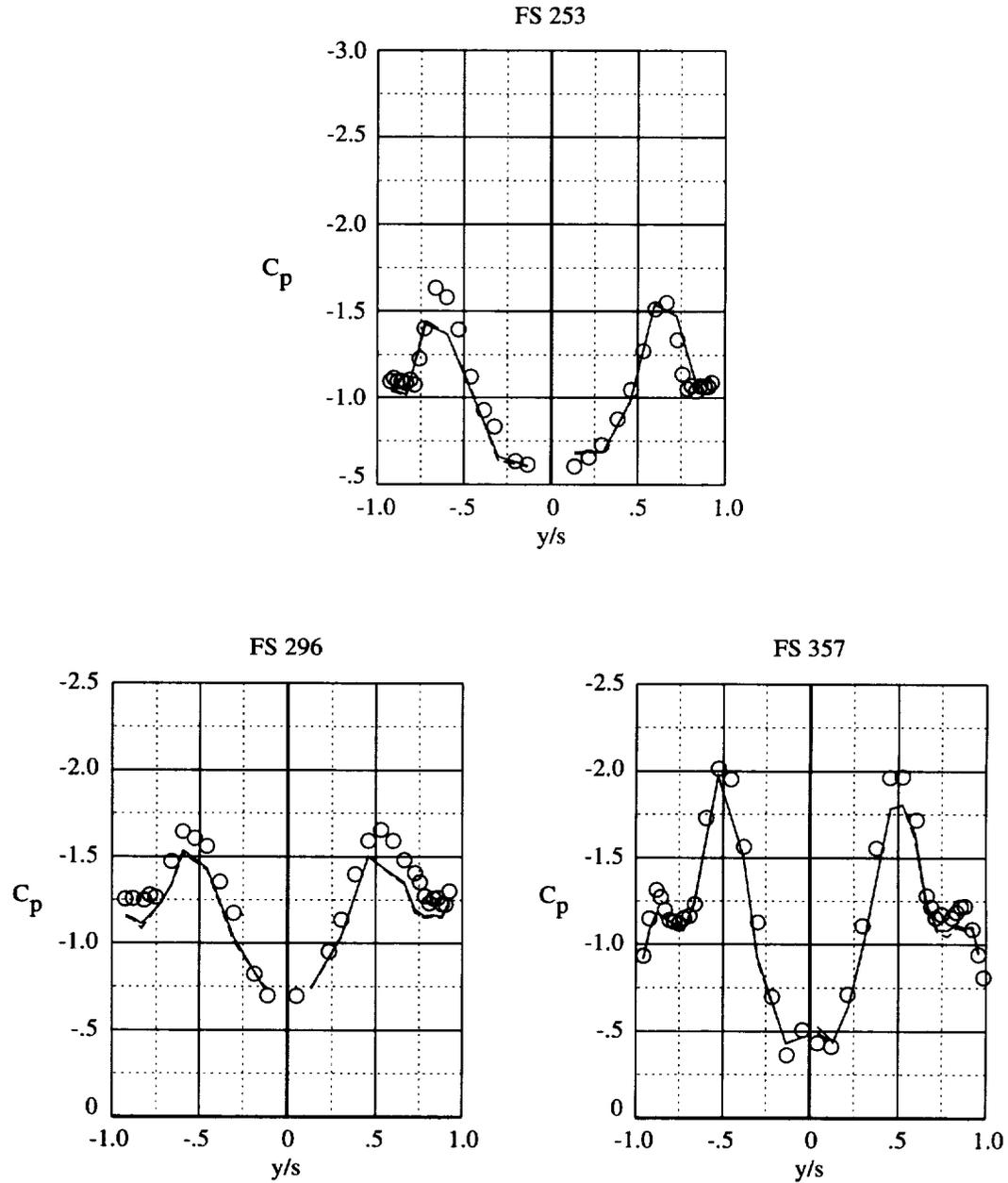
(a) $\alpha = 20°$; $\beta = 0°$.

Figure 24. Comparing tunnel LEX pressure data with either baseline grit pattern or nose-ring-only pattern to flight data without grit.

66

	Test	M_∞	α, deg	β, deg	$Re_{\bar{c}}$	Grit	Interpolated
———	7 × 10	0.30	30.0	0.1	1.40×10^6	Baseline	Yes
---------	7 × 10	0.30	30.0	0.0	1.37×10^6	Nose ring	Yes
O	Flight	0.27	30.2	0.2	10.30×10^6	No grit	No

FS 253

FS 296

FS 357

(b) $\alpha = 30°$; $\beta = 0°$.

Figure 24. Continued.

67

	Test	M_∞	α, deg	β, deg	$Re_{\bar{c}}$	Grit	Interpolated
————	7 × 10	0.30	35.0	0.1	1.39×10^6	Baseline	Yes
- - - - - - -	7 × 10	0.30	35.0	0.0	1.37×10^6	Nose ring	Yes
○	Flight	0.24	35.1	-0.5	8.88×10^6	No grit	No

FS 253

FS 296

FS 357

(c) $\alpha = 35°$; $\beta = 0°$.

Figure 24. Continued.

	Test	M_∞	α, deg	β, deg	$Re_{\overline{c}}$	Grit	Interpolated
————	7 × 10	0.30	40.0	0.1	1.39×10^6	Baseline	Yes
- - - - - - -	7 × 10	0.30	40.0	0.0	1.36×10^6	Nose ring	Yes
O	Flight	0.25	39.7	-0.3	9.57×10^6	No grit	No

FS 253
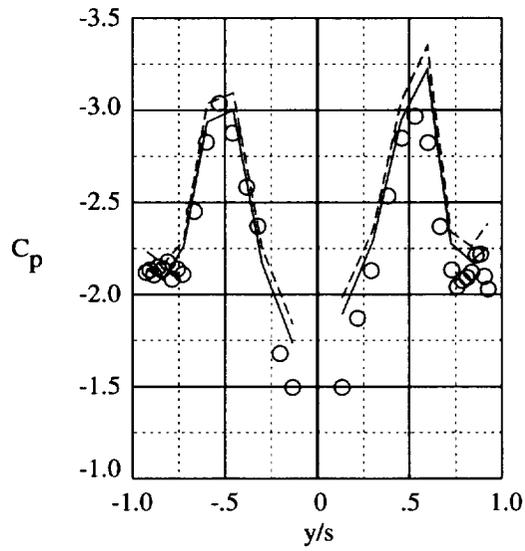
FS 296
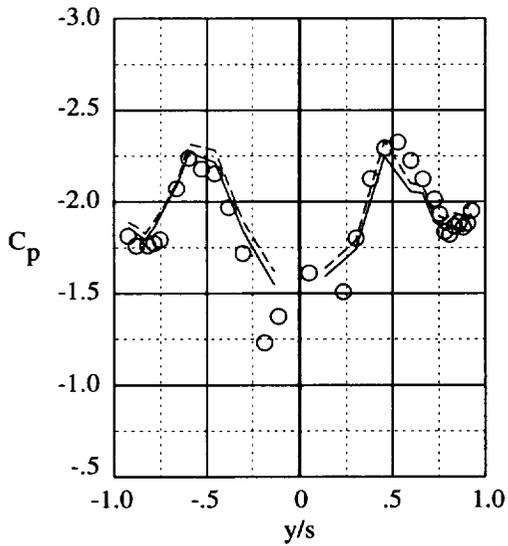
FS 357

(d) $\alpha = 40°$; $\beta = 0°$.

Figure 24. Continued.

Test	M_∞	α, deg	β, deg	$Re_{\bar{c}}$	Grit	Interpolated
———————	7 × 10	0.30	40.0	4.0	1.39×10^6	Baseline	Yes
- - - - - - - -	7 × 10	0.30	40.0	4.0	1.36×10^6	Nose ring	Yes
O	Flight	0.22	39.9	3.9	8.23×10^6	No grit	No

FS 253

FS 296

FS 357
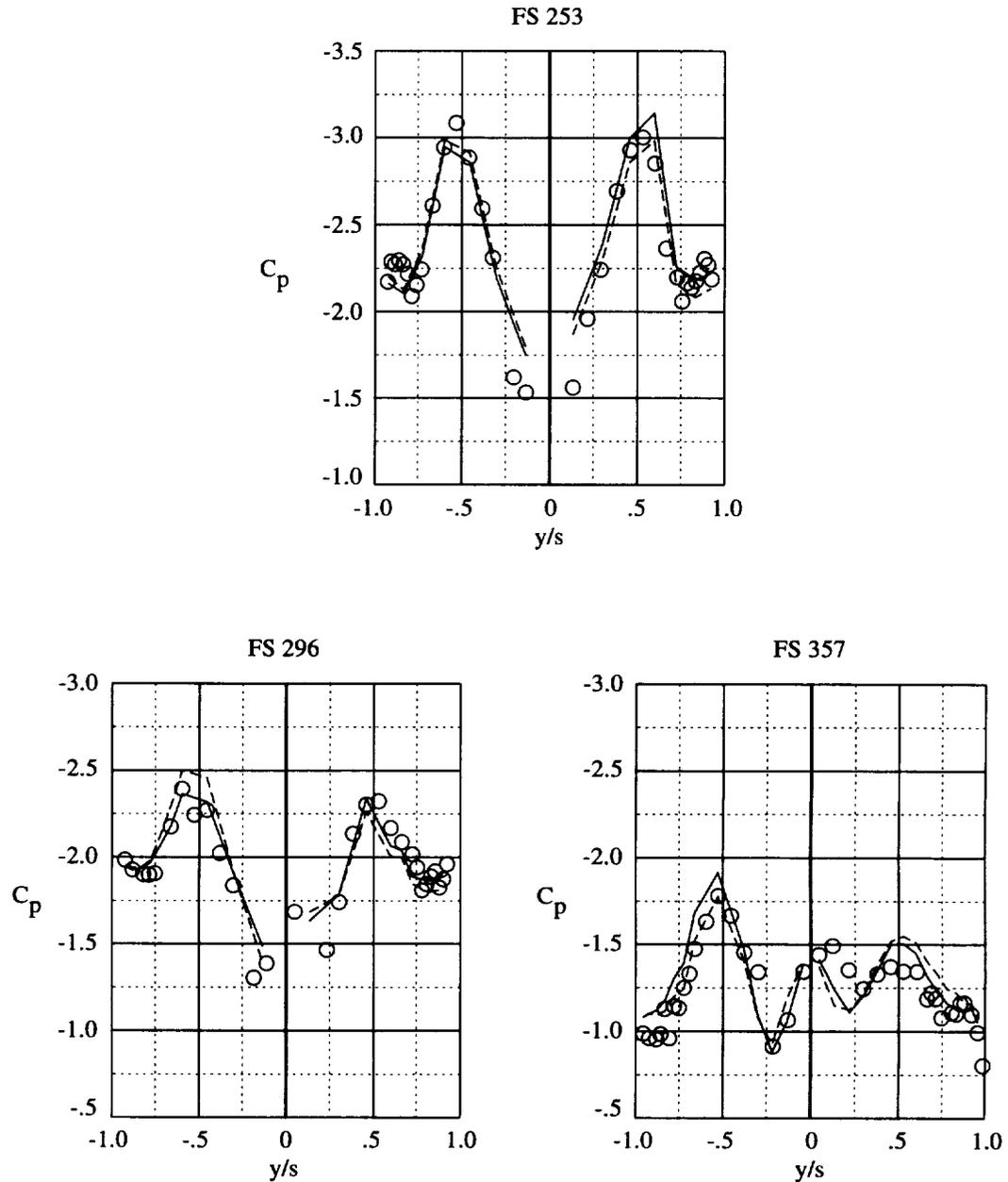
(e) $\alpha = 40°$; $\beta = 4°$.

Figure 24. Continued.

Test	M_∞	α, deg	β, deg	$Re_{\bar{c}}$	Grit	Interpolated
———— 7 × 10	0.30	40.0	8.0	1.39×10^6	Baseline	Yes
-------- 7 × 10	0.30	40.0	8.0	1.36×10^6	Nose ring	Yes
○ Flight	0.26	40.4	7.5	9.97×10^6	No grit	No

FS 253

FS 296

FS 357
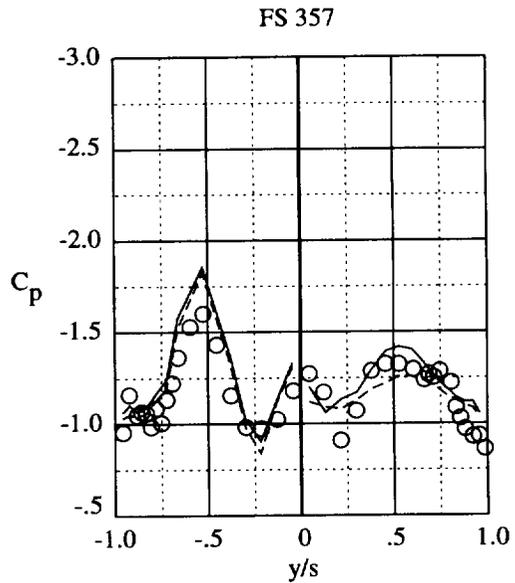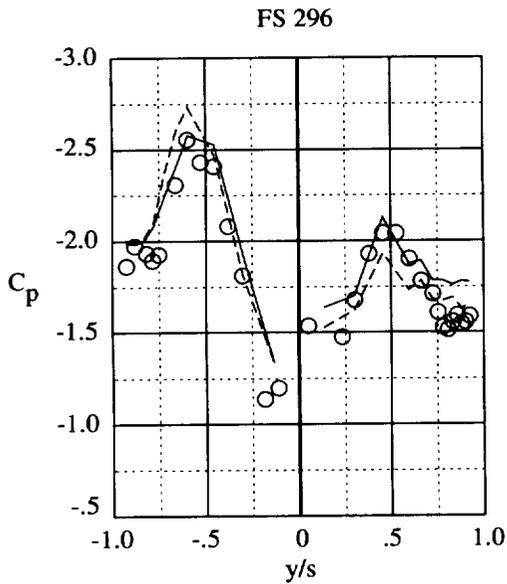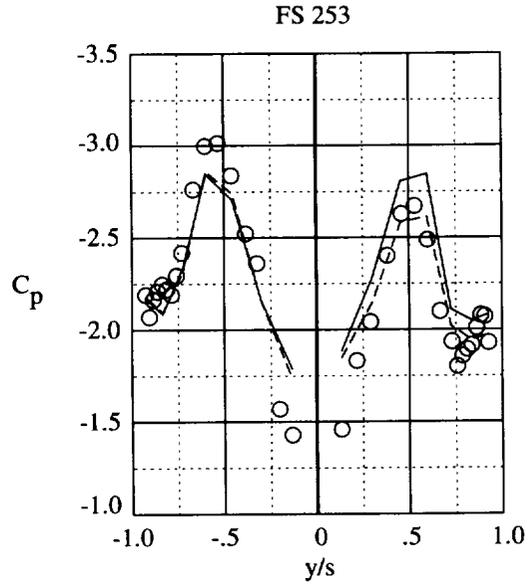
(f) $\alpha = 40°$; $\beta = 8°$.

Figure 24. Concluded.

71
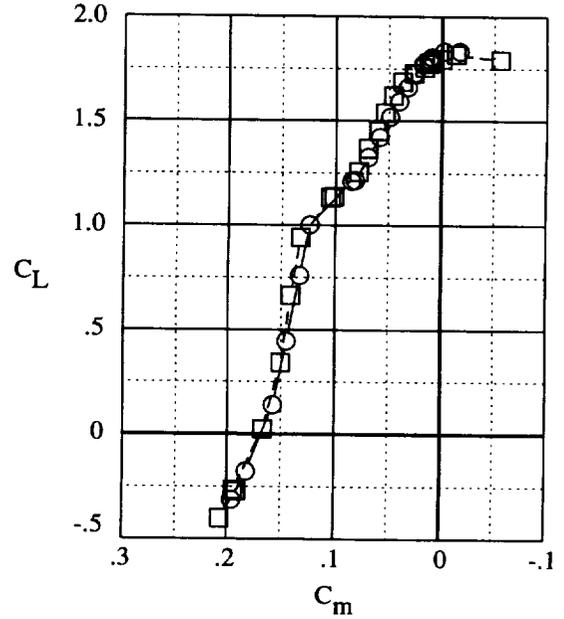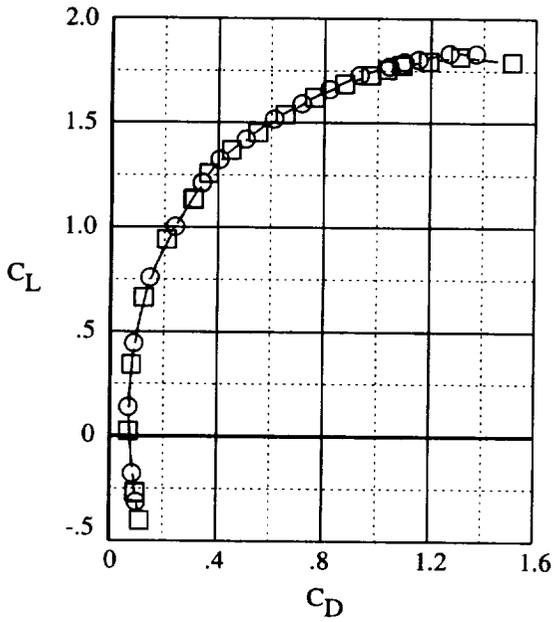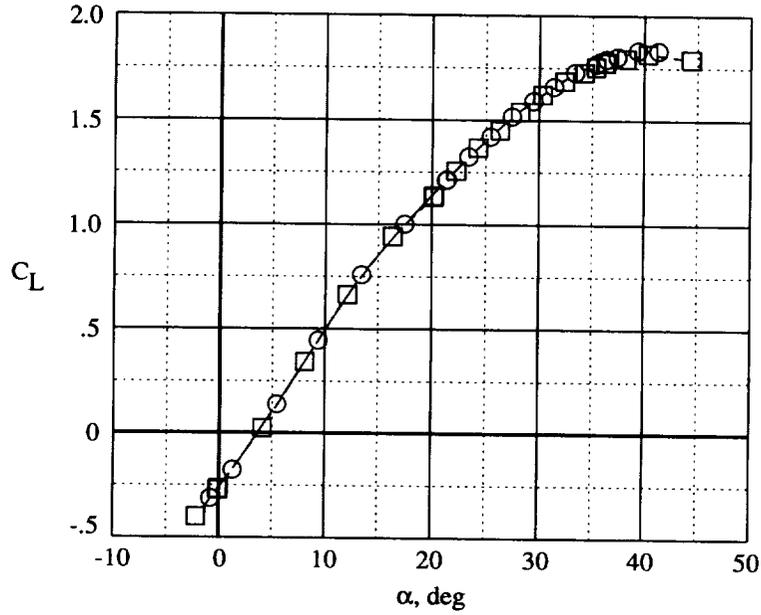
Figure 25. Baseline grit pattern compared to nose-ring-only pattern. Longitudinal properties.

Test	M_∞	α, deg	$Re_{\bar{c}}$	Grit	Interpolated
7 × 10	0.302	30.0	1.37×10^6	Baseline	Yes
7 × 10	0.302	30.0	1.37×10^6	Nose ring	Yes
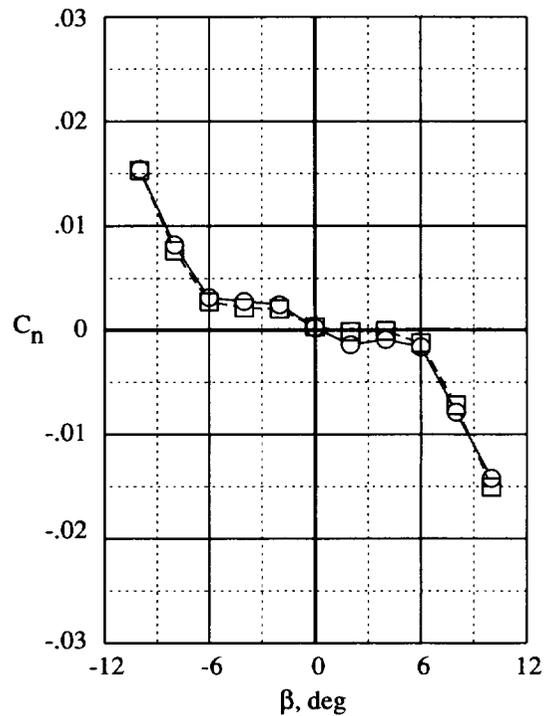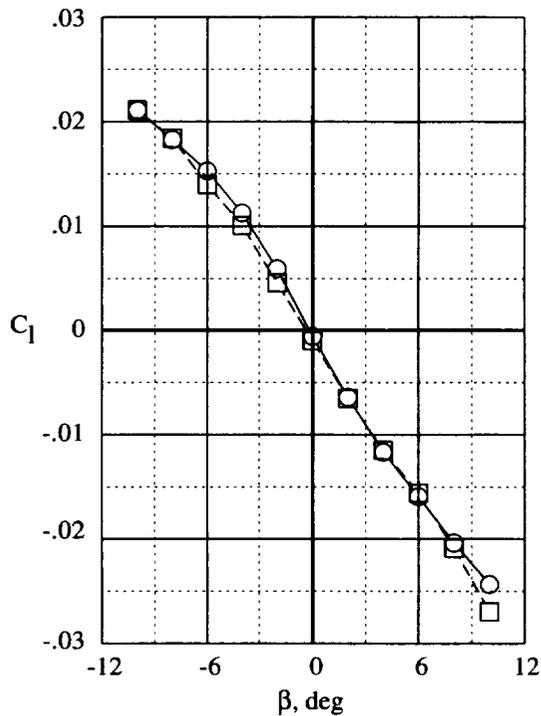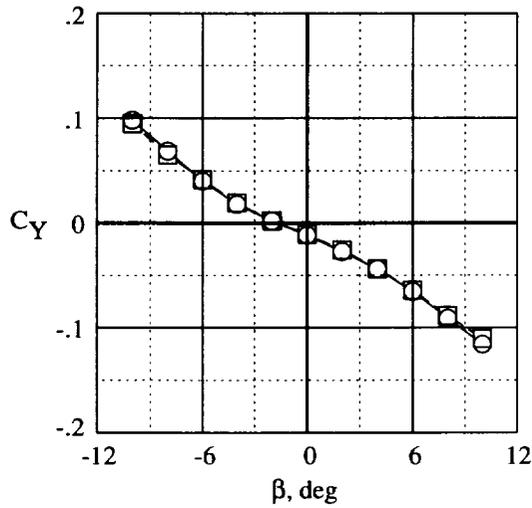
(a) $\alpha = 30°$.

Figure 26. Baseline grit pattern compared to nose-ring-only pattern. Lateral-directional properties.

	Test	M_∞	α, deg	$Re_{\bar{c}}$	Grit	Interpolated
O————	7 × 10	0.303	35.0	1.38×10^6	Baseline	Yes
□ — — — —	7 × 10	0.302	35.0	1.38×10^6	Nose ring	Yes

C_Y

β, deg

C_l

β, deg

C_n

β, deg
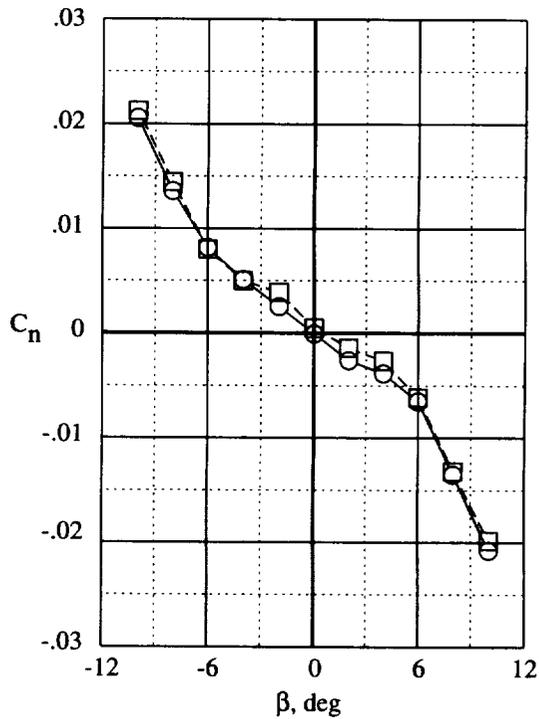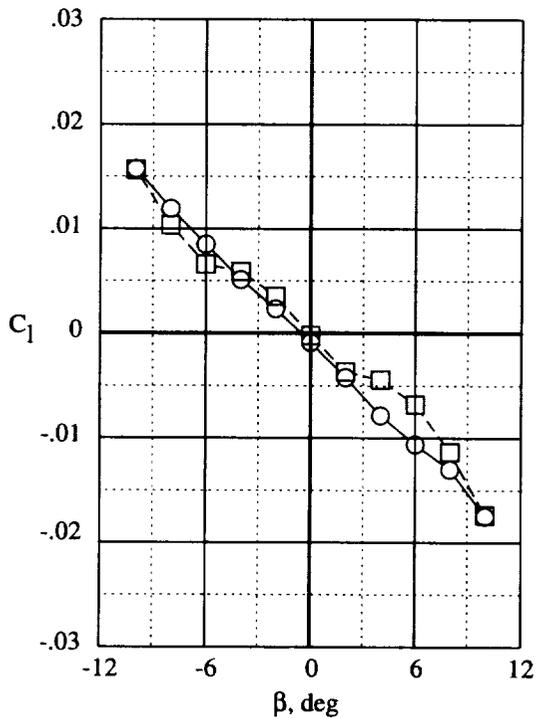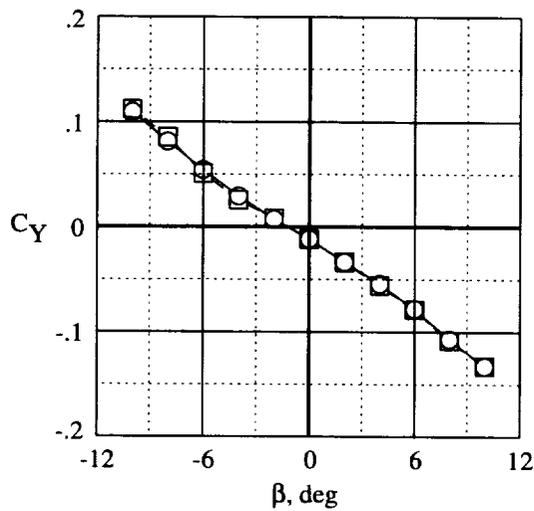
(b) $\alpha = 35°$.

Figure 26. Continued.

	Test	M_∞	α, deg	$Re_{\bar{c}}$	Grit	Interpolated
○———	7 × 10	0.303	40.0	1.39×10^6	Baseline	Yes
□- - - - -	7 × 10	0.303	40.0	1.36×10^6	Nose ring	Yes
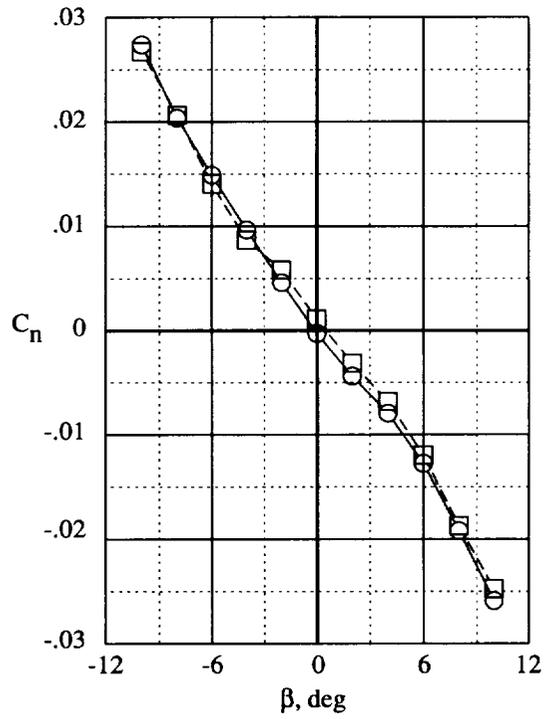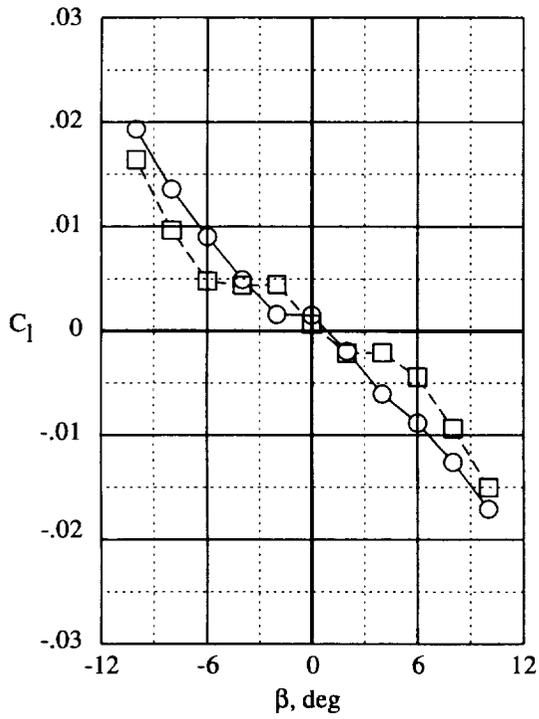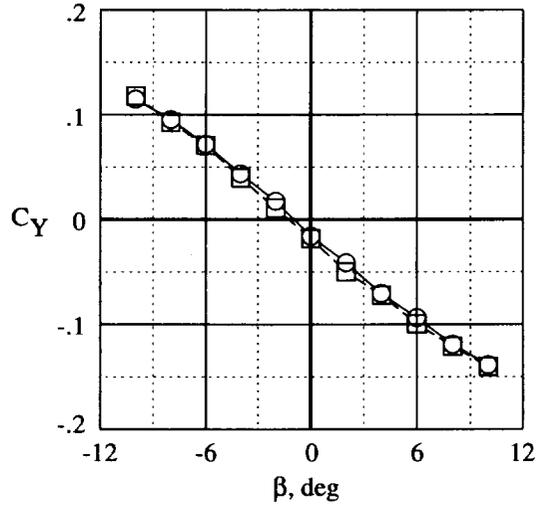
(c) $\alpha = 40°$.

Figure 26. Concluded.

Test	M_∞	α, deg	β, deg	$Re_{\bar{c}}$	Grit	Interpolated
————	7×10	0.30	20.0	0.1	1.39×10^6	Baseline + frontal	Yes
- - - - - - -	7×10	0.30	20.0	0.1	1.41×10^6	Baseline	Yes
O	Flight	0.30	20.0	-0.3	12.70×10^6	No grit	No
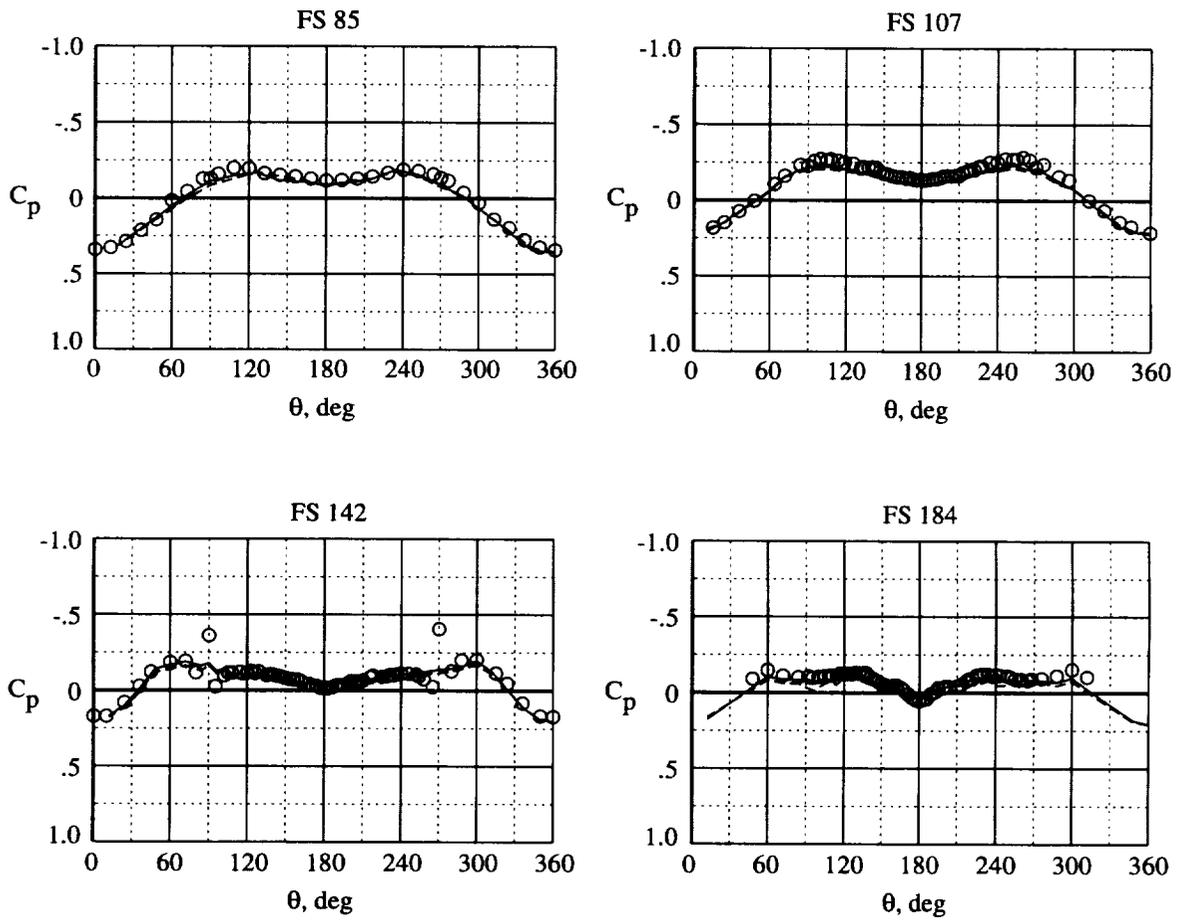
(a) $\alpha = 20°$; $\beta = 0°$.

Figure 27. Comparing tunnel forebody pressure data with baseline grit pattern plus frontal grit to baseline grit pattern and flight data without grit.

	Test	M_∞	α, deg	β, deg	$Re_{\bar{c}}$	Grit	Interpolated
————	7×10	0.30	30.0	0.2	1.38×10^6	Baseline + frontal	Yes
--------	7×10	0.30	30.0	0.1	1.40×10^6	Baseline	Yes
O	Flight	0.27	30.2	0.2	10.30×10^6	No grit	No

(b) $\alpha = 30°$; $\beta = 0°$.

Figure 27. Continued.

77

Test	M_∞	α, deg	β, deg	$Re_{\bar{c}}$	Grit	Interpolated
7 × 10	0.30	35.0	0.2	1.38×10^6	Baseline + frontal	Yes
7 × 10	0.30	35.0	0.1	1.39×10^6	Baseline	Yes
Flight	0.24	35.1	-0.5	8.88×10^6	No grit	No

(c) $\alpha = 35°$; $\beta = 0°$.

Figure 27. Continued.

78

	Test	M_∞	α, deg	β, deg	$Re_{\bar{c}}$	Grit	Interpolated
————	7 × 10	0.30	40.0	0.2	1.38×10^6	Baseline + frontal	Yes
-------	7 × 10	0.30	40.0	0.1	1.39×10^6	Baseline	Yes
o	Flight	0.25	39.7	-0.3	9.57×10^6	No grit	No

(d) $\alpha = 40°$; $\beta = 0°$.

Figure 27. Continued.

79

	Test	M_∞	α, deg	β, deg	$Re_{\bar{c}}$	Grit	Interpolated
————	7×10	0.30	40.0	4.0	1.38×10^6	Baseline + frontal	Yes
- - - - - - -	7×10	0.30	40.0	4.0	1.39×10^6	Baseline	Yes
O	Flight	0.22	39.9	3.9	8.23×10^6	No grit	No

FS 85

FS 107

FS 142

FS 184

(e) $\alpha = 40°$; $\beta = 4°$.

Figure 27. Continued.

	Test	M_∞	α, deg	β, deg	$Re_{\bar{c}}$	Grit	Interpolated
———————	7×10	0.30	40.0	8.0	1.38×10^6	Baseline + frontal	Yes
- - - - - - -	7×10	0.30	40.0	8.0	1.39×10^6	Baseline	Yes
$\circ$	Flight	0.26	40.4	7.5	9.97×10^6	No grit	No

FS 85

FS 107

FS 142

FS 184
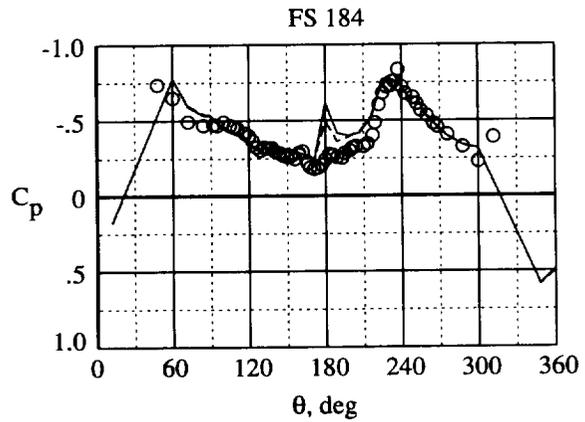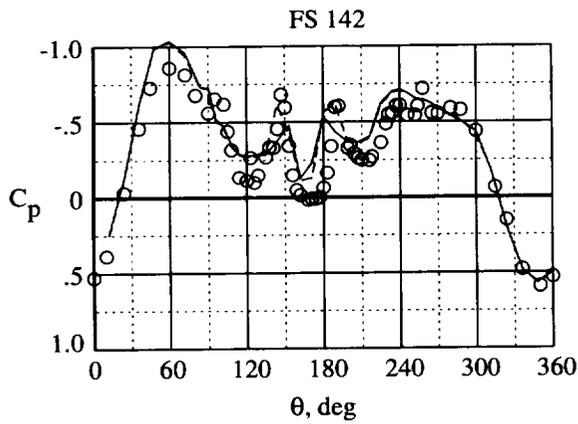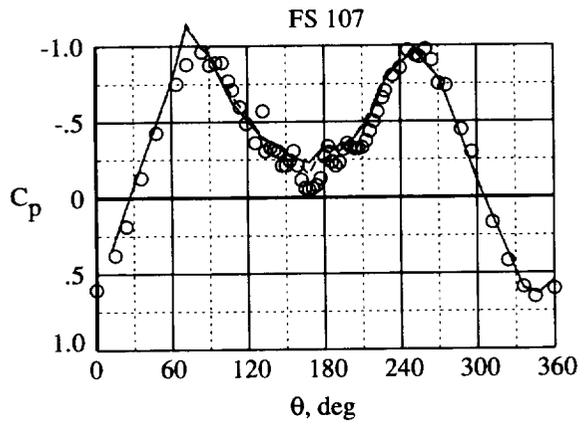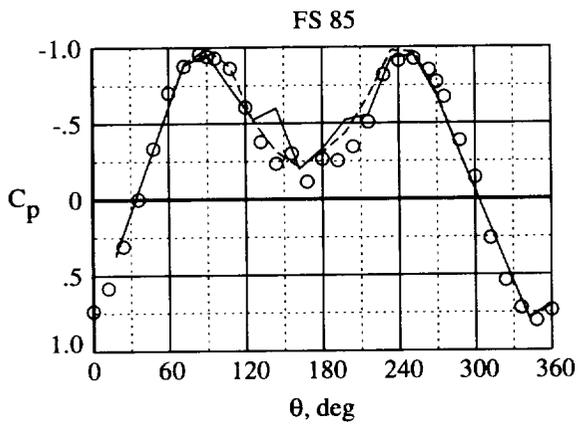
(f) $\alpha = 40°$; $\beta = 8°$.

Figure 27. Concluded.

Test	M_∞	α, deg	β, deg	$Re_{\bar{c}}$	Grit	Interpolated
——— 7 × 10	0.30	20.0	0.1	1.39×10^6	Baseline + frontal	Yes
----- 7 × 10	0.30	20.0	0.1	1.41×10^6	Baseline	Yes
○ Flight	0.30	20.0	-0.3	12.70×10^6	No grit	No

FS 253

FS 296

FS 357

(a) $\alpha = 20°$; $\beta = 0°$.
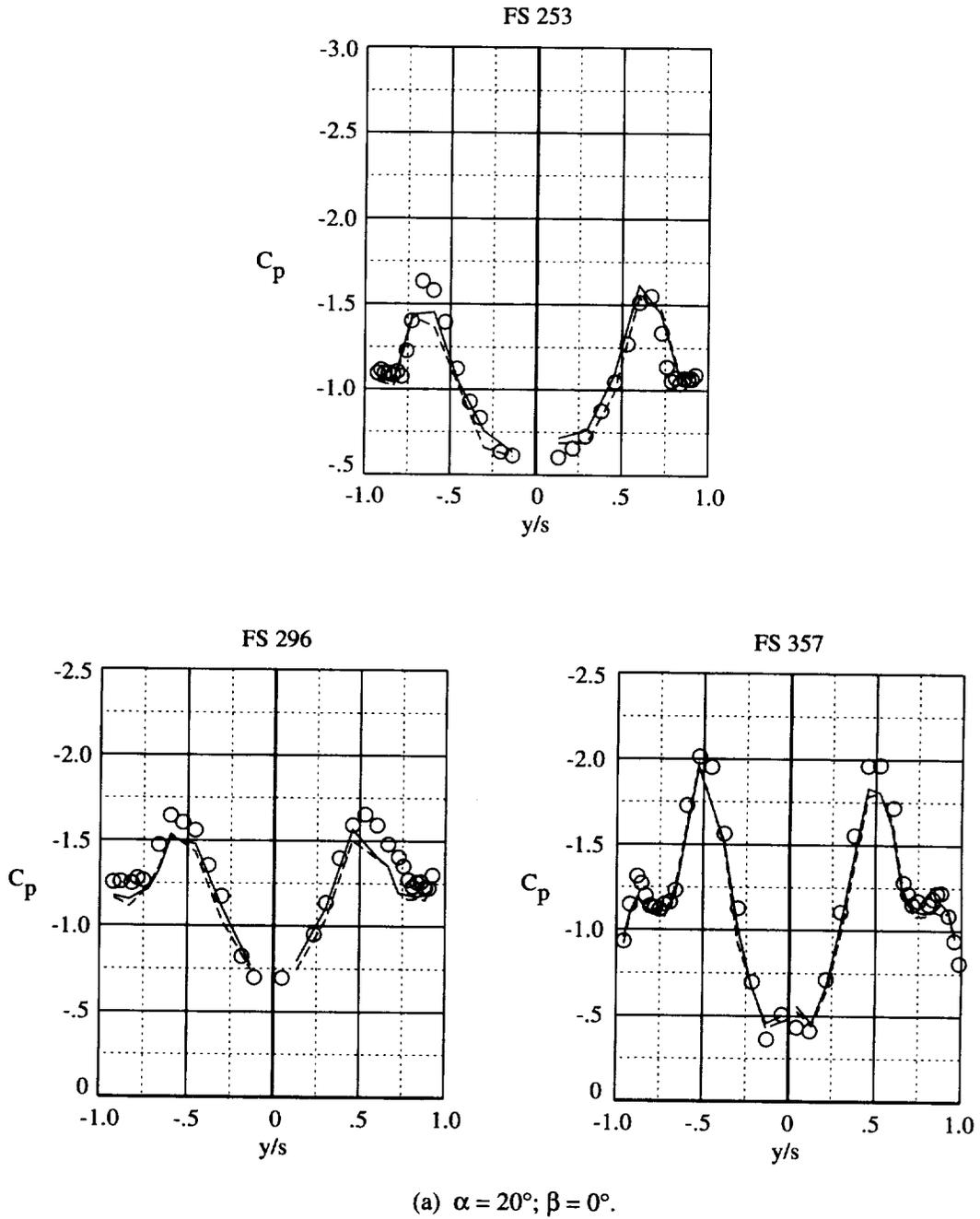
Figure 28. Comparing tunnel LEX pressure data with baseline grit pattern plus frontal grit to baseline data and flight data without grit.

	Test	M_∞	α, deg	β, deg	$Re_{\bar{c}}$	Grit	Interpolated
————	7 × 10	0.30	30.0	0.2	1.38×10^6	Baseline + frontal	Yes
– – – – –	7 × 10	0.30	30.0	0.1	1.40×10^6	Baseline	Yes
O	Flight	0.27	30.2	0.2	10.30×10^6	No grit	No

(b) $\alpha = 30°$; $\beta = 0°$.

Figure 28. Continued.

	Test	M_∞	α, deg	β, deg	$Re_{\bar{c}}$	Grit	Interpolated
————	7 × 10	0.30	35.0	0.2	1.38×10^6	Baseline + frontal	Yes
– – – –	7 × 10	0.30	35.0	0.1	1.39×10^6	Baseline	Yes
○	Flight	0.24	35.1	-0.5	8.88×10^6	No grit	No

(c) $\alpha = 35°$; $\beta = 0°$.

Figure 28. Continued.

	Test	M_∞	α, deg	β, deg	$Re_{\bar{c}}$	Grit	Interpolated
———————	7 × 10	0.30	40.0	0.2	1.38×10^6	Baseline + frontal	Yes
--------	7 × 10	0.30	40.0	0.1	1.39×10^6	Baseline	Yes
O	Flight	0.25	39.7	-0.3	9.57×10^6	No grit	No

FS 253

FS 296

FS 357

(d) $\alpha = 40°$; $\beta = 0°$.

Figure 28. Continued.

	Test	M_∞	α, deg	β, deg	$Re_{\bar{c}}$	Grit	Interpolated
————	7 × 10	0.30	40.0	4.0	1.38×10^6	Baseline + frontal	Yes
– – – – –	7 × 10	0.30	40.0	4.0	1.39×10^6	Baseline	Yes
○	Flight	0.22	39.9	3.9	8.23×10^6	No grit	No

FS 253

FS 296

FS 357

(e) $\alpha = 40°$; $\beta = 4°$.

Figure 28. Continued.

86

	Test	M_∞	α, deg	β, deg	$Re_{\bar{c}}$	Grit	Interpolated
——————	7 × 10	0.30	40.0	8.0	1.38×10^6	Baseline + frontal	Yes
- - - - - - - -	7 × 10	0.30	40.0	8.0	1.39×10^6	Baseline	Yes
O	Flight	0.26	40.4	7.5	9.97×10^6	No grit	No

FS 253

FS 296

FS 357

(f) $\alpha = 40°$; $\beta = 8°$.

Figure 28. Concluded.

Test	M_∞	$Re_{\bar{c}}$	Grit	Interpolated
7×10	0.300	1.39×10^6	Baseline + frontal	No
7×10	0.301	1.41×10^6	Baseline	No
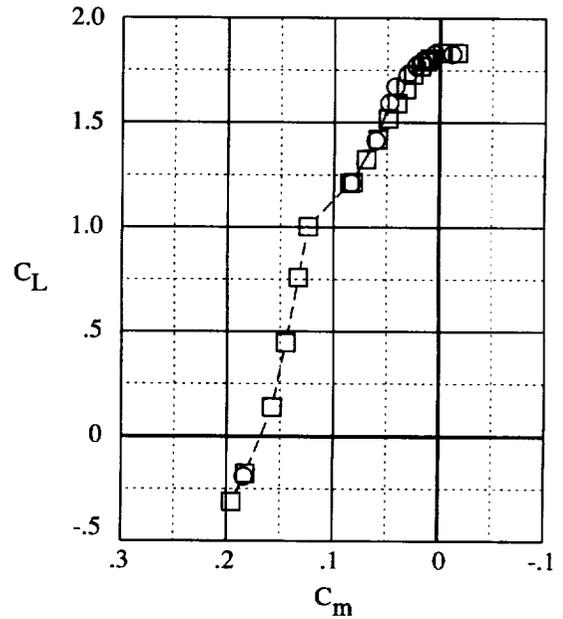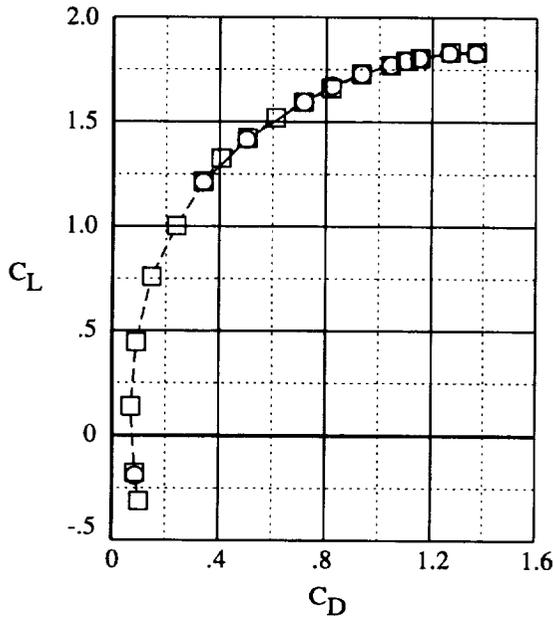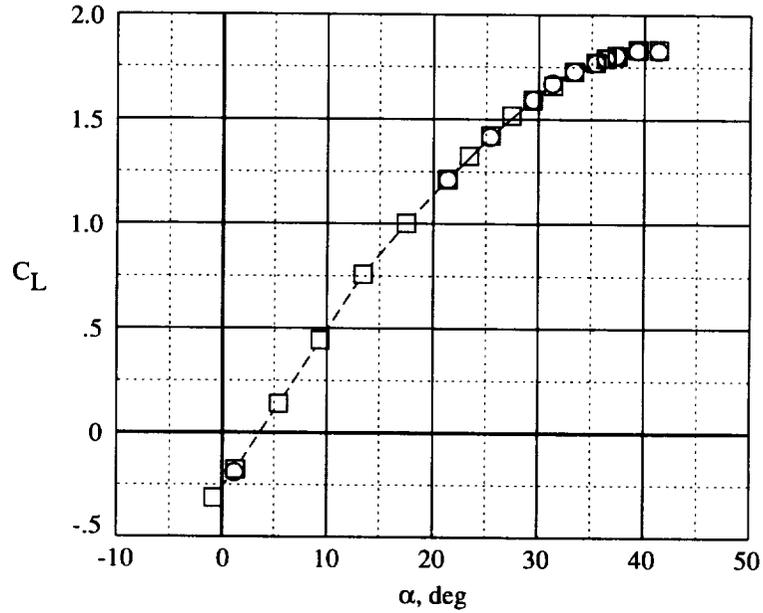
Figure 29. Baseline grit pattern plus frontal grit compared to baseline grit pattern. Longitudinal properties.
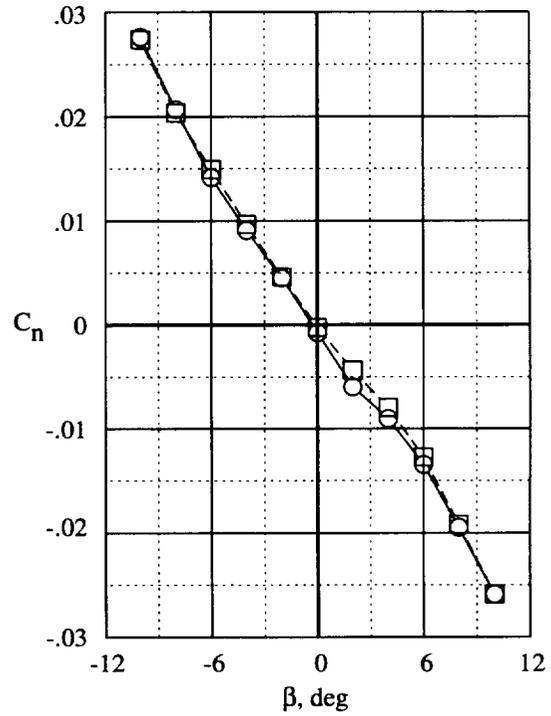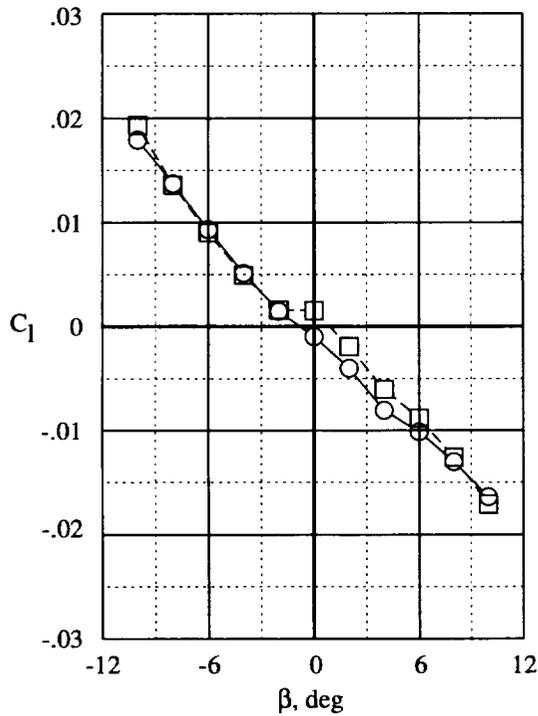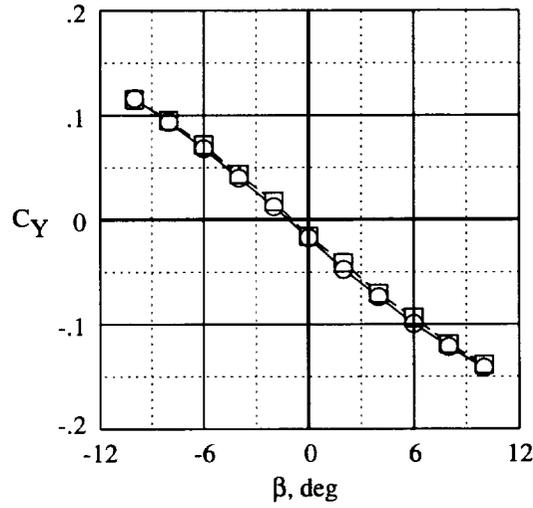
Figure 30. Baseline grit pattern plus frontal grit compared to baseline grit pattern. Lateral-directional properties. α = 40°.

Test	M_∞	α, deg	β, deg	$Re_{\bar{c}}$	Grit	Interpolated
———	7 × 10	0.30	20.0	0.2	1.37×10^6	Baseline + side	Yes
- - - - - - -	7 × 10	0.30	20.0	0.1	1.41×10^6	Baseline	Yes
O	Flight	0.30	20.0	-0.3	12.70×10^6	No grit	No

(a) $\alpha = 20°$; $\beta = 0°$.

Figure 31. Comparing tunnel forebody pressure data with baseline grit pattern plus side grit to baseline grit pattern and flight data without grit.

	Test	M_∞	α, deg	β, deg	$Re_{\bar{c}}$	Grit	Interpolated
——————	7 × 10	0.30	30.0	0.2	1.37×10^6	Baseline + side	Yes
- - - - - - -	7 × 10	0.30	30.0	0.1	1.40×10^6	Baseline	Yes
○	Flight	0.27	30.2	0.2	10.30×10^6	No grit	No

FS 85

FS 107

FS 142

FS 184

(b) $\alpha = 30°$; $\beta = 0°$.

Figure 31. Continued.

Test	M_∞	α, deg	β, deg	$Re_{\bar{c}}$	Grit	Interpolated
———	7 × 10	0.30	35.0	0.3	1.36×10^6	Baseline + side	Yes
- - - - -	7 × 10	0.30	35.0	0.1	1.39×10^6	Baseline	Yes
○	Flight	0.24	35.1	-0.5	8.88×10^6	No grit	No

FS 85

FS 107

FS 142

FS 184

(c) $\alpha = 35°$; $\beta = 0°$.

Figure 31. Continued.

Test	M_∞	α, deg	β, deg	$Re_{\bar{c}}$	Grit	Interpolated
————	7×10	0.30	40.0	0.3	1.37×10^6	Baseline + side	Yes
-------	7×10	0.30	40.0	0.1	1.39×10^6	Baseline	Yes
O	Flight	0.25	39.7	-0.3	9.57×10^6	No grit	No

FS 85

FS 107

FS 142

FS 184

(d) $\alpha = 40°$; $\beta = 0°$.

Figure 31. Continued.

	Test	M_∞	α, deg	β, deg	$Re_{\bar{c}}$	Grit	Interpolated
————	7 × 10	0.30	40.0	4.0	1.38×10^6	Baseline + side	Yes
- - - - - -	7 × 10	0.30	40.0	4.0	1.39×10^6	Baseline	Yes
○	Flight	0.22	39.9	3.9	8.23×10^6	No grit	No

FS 85

FS 107

FS 142

FS 184

(e) $\alpha = 40°$; $\beta = 4°$.

Figure 31. Continued.

	Test	M_∞	α, deg	β, deg	$Re_{\bar{c}}$	Grit	Interpolated
——————	7×10	0.30	40.0	8.0	1.37×10^6	Baseline + side	Yes
- - - - - - -	7×10	0.30	40.0	8.0	1.39×10^6	Baseline	Yes
o	Flight	0.26	40.4	7.5	9.97×10^6	No grit	No

FS 85

FS 107

FS 142

FS 184

(f) $\alpha = 40°$; $\beta = 8°$.

Figure 31. Concluded.

	Test	M_∞	α, deg	β, deg	$Re_{\bar{c}}$	Grit	Interpolated
———	7×10	0.30	20.0	0.2	1.37×10^6	Baseline + side	Yes
‑‑‑‑‑‑‑	7×10	0.30	20.0	0.1	1.41×10^6	Baseline	Yes
O	Flight	0.30	20.0	-0.3	12.70×10^6	No grit	No
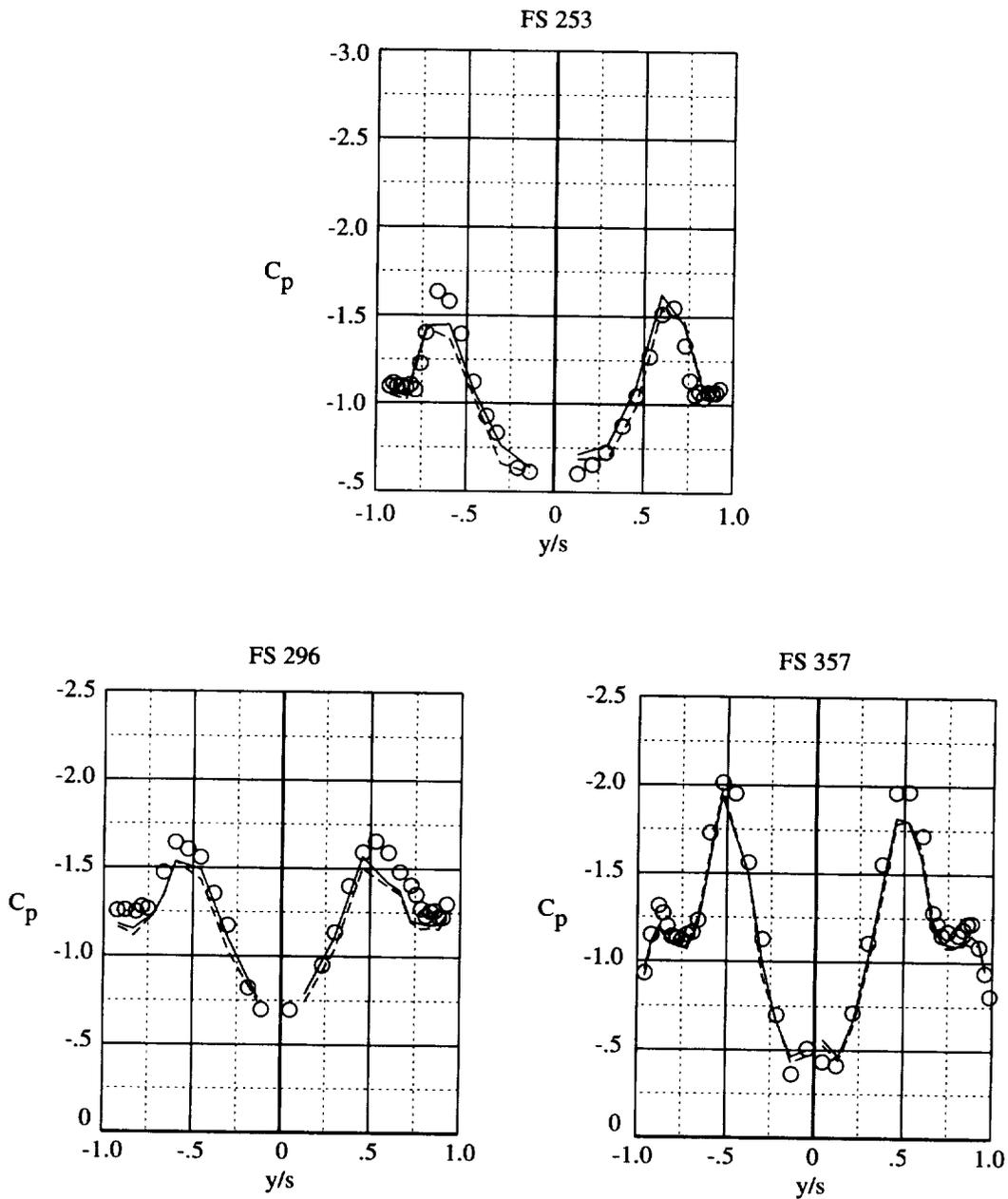
(a) $\alpha = 20°$; $\beta = 0°$.

Figure 32. Comparing tunnel LEX pressure data with baseline grit pattern plus side grit to baseline grit pattern and flight data without grit.

	Test	M_∞	α, deg	β, deg	$Re_{\bar{c}}$	Grit	Interpolated
———————	7 × 10	0.30	30.0	0.2	1.37×10^6	Baseline + side	Yes
- - - - - - - - -	7 × 10	0.30	30.0	0.1	1.40×10^6	Baseline	Yes
O	Flight	0.27	30.2	0.2	10.30×10^6	No grit	No

FS 253

FS 296

FS 357

(b) $\alpha = 30°$; $\beta = 0°$.

Figure 32. Continued.

Test	M_∞	α, deg	β, deg	$Re_{\bar{c}}$	Grit	Interpolated
———————	7 × 10	0.30	35.0	0.3	1.36×10^6	Baseline + side	Yes
– – – – – – –	7 × 10	0.30	35.0	0.1	1.39×10^6	Baseline	Yes
O	Flight	0.24	35.1	-0.5	8.88×10^6	No grit	No

FS 253

FS 296

FS 357

(c) $\alpha = 35°$; $\beta = 0°$.

Figure 32. Continued.

	Test	M_{∞}	α, deg	β, deg	$Re_{\bar{c}}$	Grit	Interpolated
————	7×10	0.30	40.0	0.3	1.37×10^6	Baseline + side	Yes
- - - - - - -	7×10	0.30	40.0	0.1	1.39×10^6	Baseline	Yes
O	Flight	0.25	39.7	-0.3	9.57×10^6	No grit	No

FS 253

FS 296

FS 357

(d) $\alpha = 40°$; $\beta = 0°$.

Figure 32. Continued.

	Test	M_∞	α, deg	β, deg	$Re_{\bar{c}}$	Grit	Interpolated
————	7×10	0.30	40.0	4.0	1.38×10^6	Baseline + side	Yes
--------	7×10	0.30	40.0	4.0	1.39×10^6	Baseline	Yes
O	Flight	0.22	39.9	3.9	8.23×10^6	No grit	No

FS 253

FS 296

FS 357

(e) $\alpha = 40°$; $\beta = 4°$.

Figure 32. Continued.

100

	Test	M_∞	α, deg	β, deg	$Re_{\bar{c}}$	Grit	Interpolated
———————	7 × 10	0.30	40.0	8.0	1.37×10^6	Baseline + side	Yes
- - - - - - - - -	7 × 10	0.30	40.0	8.0	1.39×10^6	Baseline	Yes
O	Flight	0.26	40.4	7.5	9.97×10^6	No grit	No

FS 253

FS 296

FS 357

(f) $\alpha = 40°$; $\beta = 8°$.

Figure 32. Concluded.

Test	M_∞	$Re_{\bar{c}}$	Grit	Interpolated
7×10	0.301	1.37×10^6	Baseline + side	No
7×10	0.301	1.41×10^6	Baseline	No
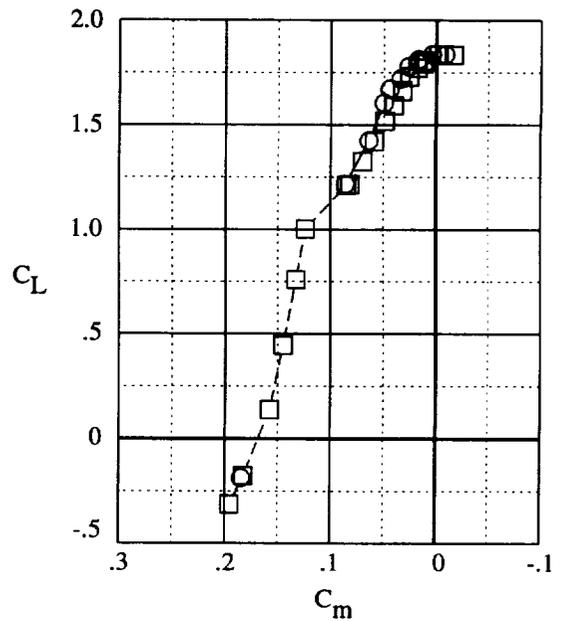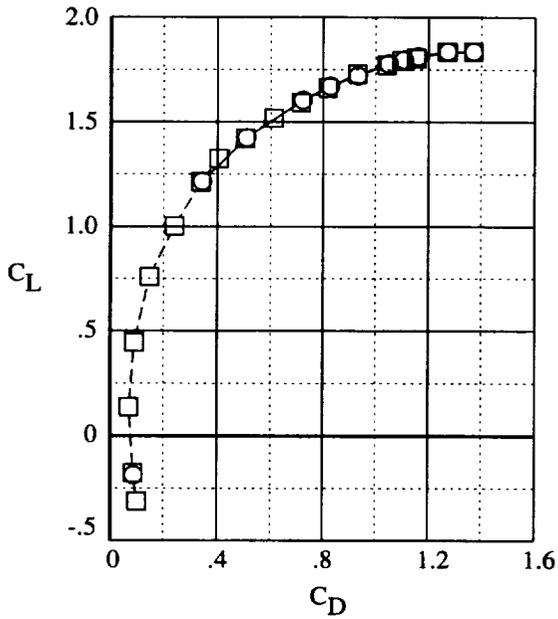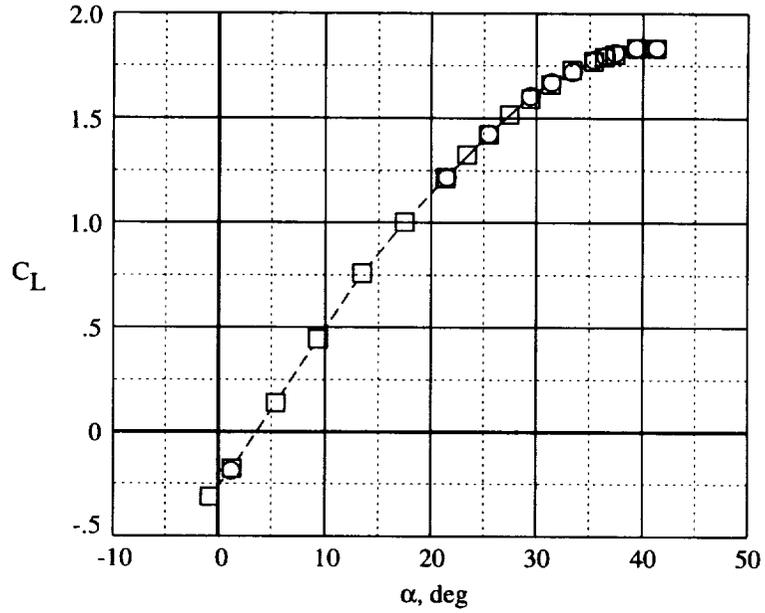
Figure 33. Baseline grit pattern plus side grit compared to baseline grit pattern. Longitudinal properties.

	Test	M_∞	α, deg	$Re_{\bar{c}}$	Grit	Interpolated
○———	7×10	0.303	40.0	1.37×10^6	Baseline + side	Yes
□-----	7×10	0.303	40.0	1.39×10^6	Baseline	Yes
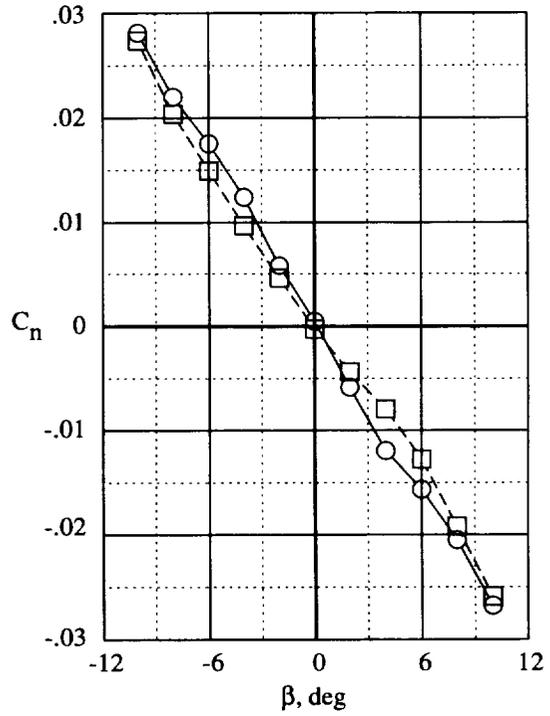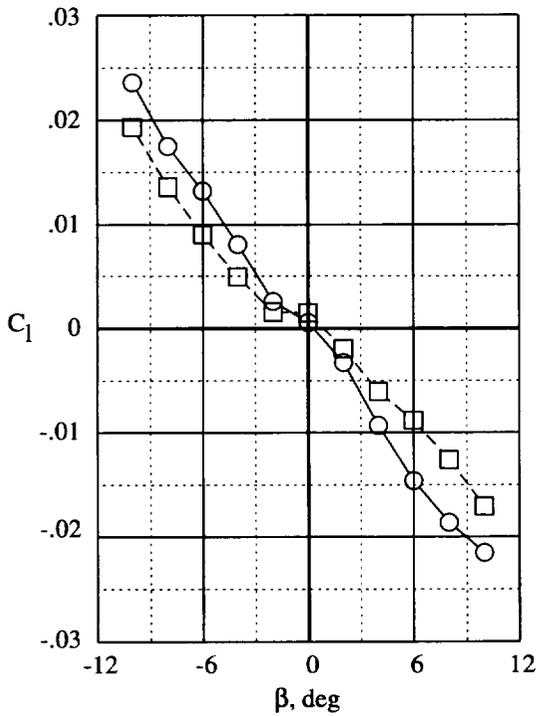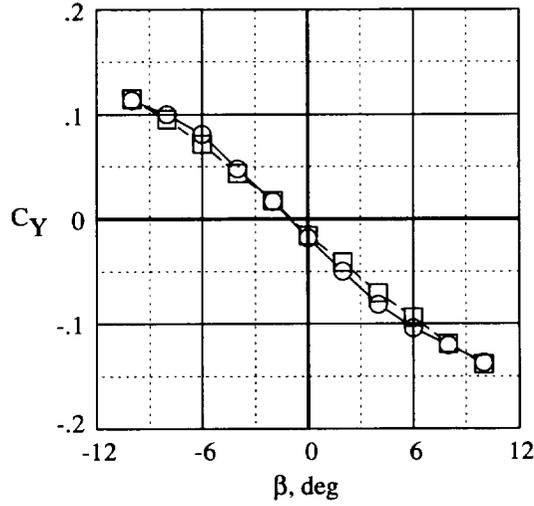
Figure 34. Baseline grit pattern plus side grit compared to baseline grit pattern. Lateral-directional properties. $\alpha = 40°$.

Test	M_∞	α, deg	β, deg	$Re_{\bar{c}}$	Grit	Interpolated
———	7 × 10	0.30	20.0	0.2	1.37×10^6	Baseline w/narrower strips	Yes
- - - - -	7 × 10	0.30	20.0	0.1	1.41×10^6	Baseline	Yes
○	Flight	0.30	20.0	-0.3	12.70×10^6	No grit	No

(a) $\alpha = 20°$; $\beta = 0°$.

Figure 35. Comparing tunnel forebody pressure data with baseline grit pattern modified with narrower twin strips to baseline grit pattern and flight data without grit.

	Test	M_∞	α, deg	β, deg	$Re_{\bar{c}}$	Grit	Interpolated
———	7 × 10	0.30	30.0	0.3	1.37×10^6	Baseline w/narrower strips	Yes
- - - - - -	7 × 10	0.30	30.0	0.1	1.40×10^6	Baseline	Yes
○	Flight	0.27	30.2	0.2	10.30×10^6	No grit	No

(b) $\alpha = 30°$; $\beta = 0°$.

Figure 35. Continued.

	Test	M_∞	α, deg	β, deg	$Re_{\bar{c}}$	Grit	Interpolated
———	7 × 10	0.30	30.0	0.3	1.37×10^6	Baseline w/narrower strips	Yes
- - - - - -	7 × 10	0.30	30.0	0.1	1.40×10^6	Baseline	Yes
○	Flight	0.27	30.2	0.2	10.30×10^6	No grit	No

FS 85   FS 107   FS 142   FS 184

(b) $\alpha = 30°$; $\beta = 0°$.

Figure 35. Continued.

	Test	M_∞	α, deg	β, deg	$Re_{\bar{c}}$	Grit	Interpolated
———	7 × 10	0.30	35.0	0.3	1.36×10^6	Baseline w/narrower strips	Yes
- - - - -	7 × 10	0.30	35.0	0.1	1.39×10^6	Baseline	Yes
O	Flight	0.24	35.1	-0.5	8.88×10^6	No grit	No

(c) $\alpha = 35°$; $\beta = 0°$.

Figure 35. Continued.

106

Test	M_∞	α, deg	β, deg	$Re_{\bar{c}}$	Grit	Interpolated
————	7×10	0.30	40.0	0.4	1.35×10^6	Baseline w/narrower strips	Yes
--------	7×10	0.30	40.0	0.1	1.39×10^6	Baseline	Yes
○	Flight	0.25	39.7	-0.3	9.57×10^6	No grit	No

(d) $\alpha = 40°$; $\beta = 0°$.

Figure 35. Continued.

Test	M_∞	α, deg	β, deg	$Re_{\bar{c}}$	Grit	Interpolated
7 × 10	0.30	40.0	4.0	1.34×10^6	Baseline w/narrower strips	Yes
7 × 10	0.30	40.0	4.0	1.39×10^6	Baseline	Yes
Flight	0.22	39.9	3.9	8.23×10^6	No grit	No

(e) α = 40°; β = 4°.

Figure 35. Continued.

108

Test	M_∞	α, deg	β, deg	$Re_{\bar{c}}$	Grit	Interpolated
——— 7 × 10	0.30	40.0	8.0	1.33×10^6	Baseline w/narrower strips	Yes
– – – – – 7 × 10	0.30	40.0	8.0	1.39×10^6	Baseline	Yes
○ Flight	0.26	40.4	7.5	9.97×10^6	No grit	No

FS 85

FS 107

FS 142

FS 184

(f) $\alpha = 40°$; $\beta = 8°$.

Figure 35. Concluded.

Test	M_∞	α, deg	β, deg	$Re_{\bar{c}}$	Grit	Interpolated
——————	7×10	0.30	20.0	0.2	1.37×10^6	Baseline w/narrower strips	Yes
————————	7×10	0.30	20.0	0.1	1.41×10^6	Baseline	Yes
O	Flight	0.30	20.0	-0.3	12.70×10^6	No grit	No

FS 253

FS 296 FS 357

(a) $\alpha = 20°$; $\beta = 0°$.

Figure 36. Comparing tunnel LEX pressure data with baseline grit pattern modified with narrower twin strips to baseline grit pattern and flight data without grit.

110

	Test	M_∞	α, deg	β, deg	$Re_{\bar{c}}$	Grit	Interpolated
————	7 × 10	0.30	30.0	0.3	1.37×10^6	Baseline w/narrower strips	Yes
– – – – –	7 × 10	0.30	30.0	0.1	1.40×10^6	Baseline	Yes
O	Flight	0.27	30.2	0.2	10.30×10^6	No grit	No

FS 253

FS 296

FS 357

(b) $\alpha = 30°$; $\beta = 0°$.

Figure 36. Continued.

111

	Test	M_∞	α, deg	β, deg	$Re_{\bar{c}}$	Grit	Interpolated
———	7×10	0.30	35.0	0.3	1.36×10^6	Baseline w/narrower strips	Yes
– – – – –	7×10	0.30	35.0	0.1	1.39×10^6	Baseline	Yes
O	Flight	0.24	35.1	-0.5	8.88×10^6	No grit	No

FS 253

FS 296

FS 357

(c) $\alpha = 35°$; $\beta = 0°$.

Figure 36. Continued.

Test	M_∞	α, deg	β, deg	$Re_{\bar{c}}$	Grit	Interpolated
——— 7×10	0.30	40.0	0.4	1.35×10^6	Baseline w/narrower strips	Yes
- - - - - - 7×10	0.30	40.0	0.1	1.39×10^6	Baseline	Yes
O Flight	0.25	39.7	-0.3	9.57×10^6	No grit	No

FS 253

FS 296

FS 357

(d) $\alpha = 40°$; $\beta = 0°$.

Figure 36. Continued.

	Test	M_∞	α, deg	β, deg	$Re_{\bar{c}}$	Grit	Interpolated
———————	7 × 10	0.30	40.0	4.0	1.34×10^6	Baseline w/narrower strips	Yes
– – – – – – –	7 × 10	0.30	40.0	4.0	1.39×10^6	Baseline	Yes
○	Flight	0.22	39.9	3.9	8.23×10^6	No grit	No

FS 253

FS 296

FS 357

(e) $\alpha = 40°$; $\beta = 4°$.

Figure 36. Continued.

114

	Test	M_∞	α, deg	β, deg	$Re_{\bar{c}}$	Grit	Interpolated
————	7 × 10	0.30	40.0	8.0	1.33×10^6	Baseline w/narrower strips	Yes
- - - - - - -	7 × 10	0.30	40.0	8.0	1.39×10^6	Baseline	Yes
O	Flight	0.26	40.4	7.5	9.97×10^6	No grit	No

FS 253

FS 296

FS 357

(f) $\alpha = 40°$; $\beta = 8°$.

Figure 36. Concluded.

115

|	Test	M_∞	$Re_{\bar{c}}$	Grit	Interpolated
o———	7×10	0.301	1.38×10^6	Baseline w/narrower strips	No
□------	7×10	0.301	1.41×10^6	Baseline	No
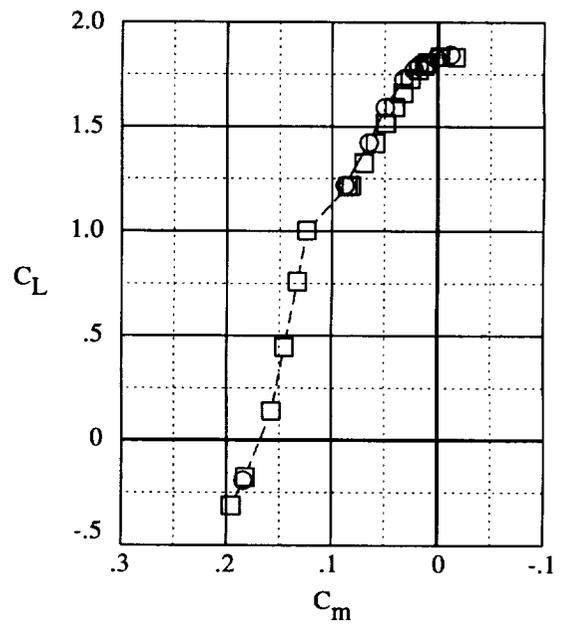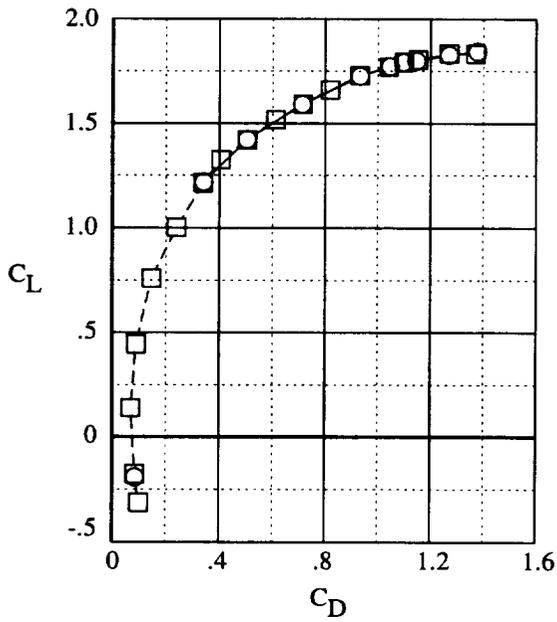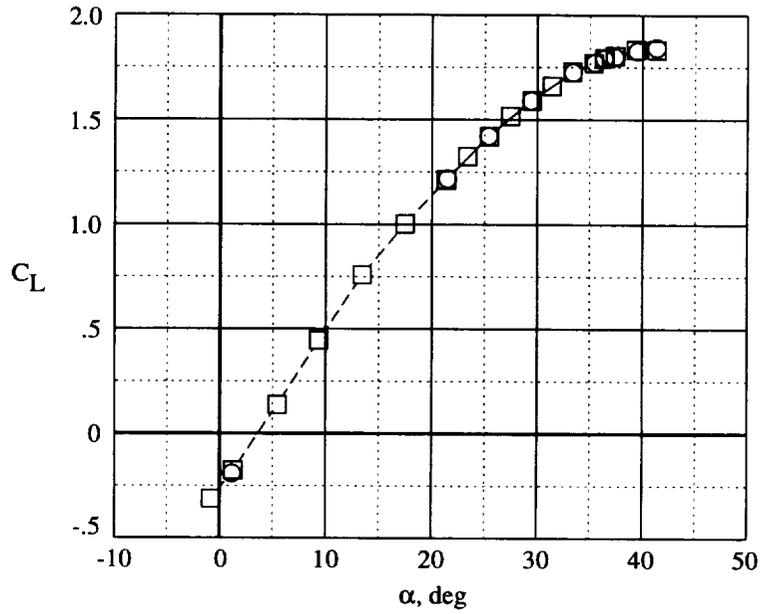
Figure 37. Baseline grit pattern modified with narrower twin strips compared to baseline grit pattern. Longitudinal properties.

|	Test	M_∞	α, deg	$Re_{\bar{c}}$	Grit	Interpolated
○———	7 × 10	0.303	40.0	1.33×10^6	Baseline w/narrower strips	Yes
□-----	7 × 10	0.303	40.0	1.39×10^6	Baseline	Yes
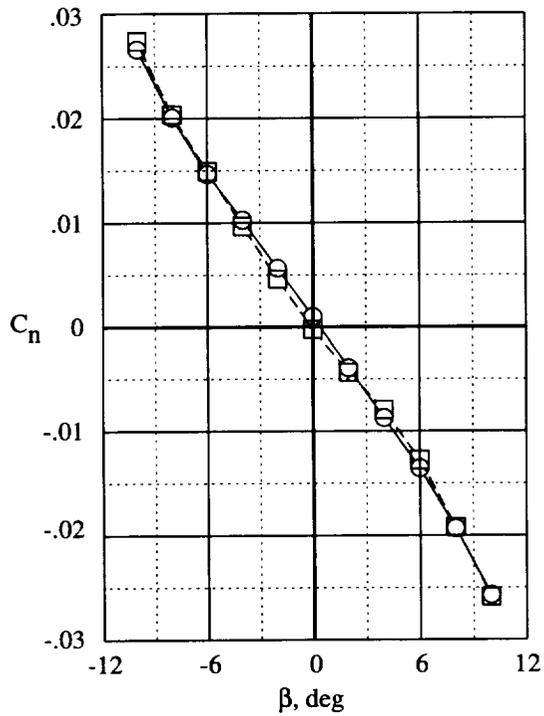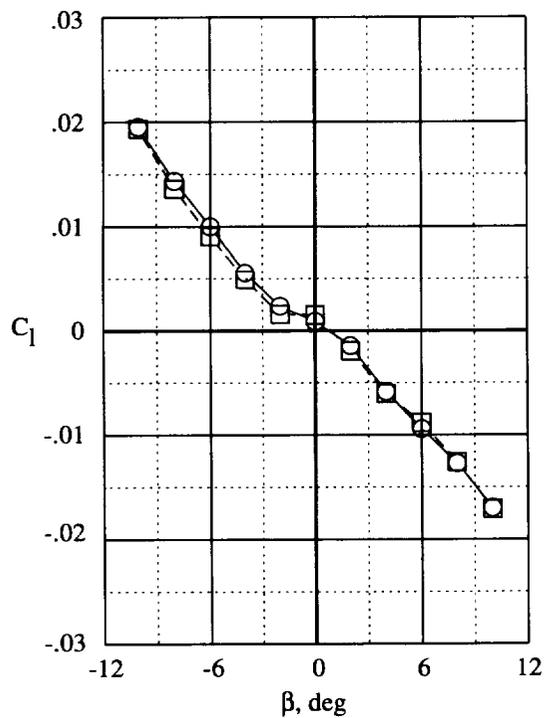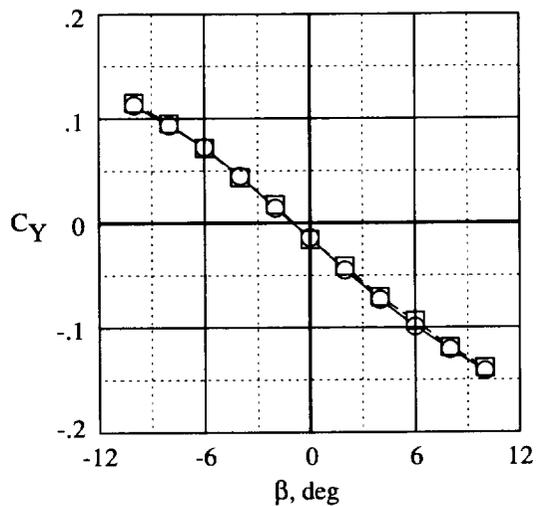
Figure 38. Baseline grit pattern modified with narrower twin strips compared to baseline grit pattern. Lateral-directional properties. $\alpha = 40°$.
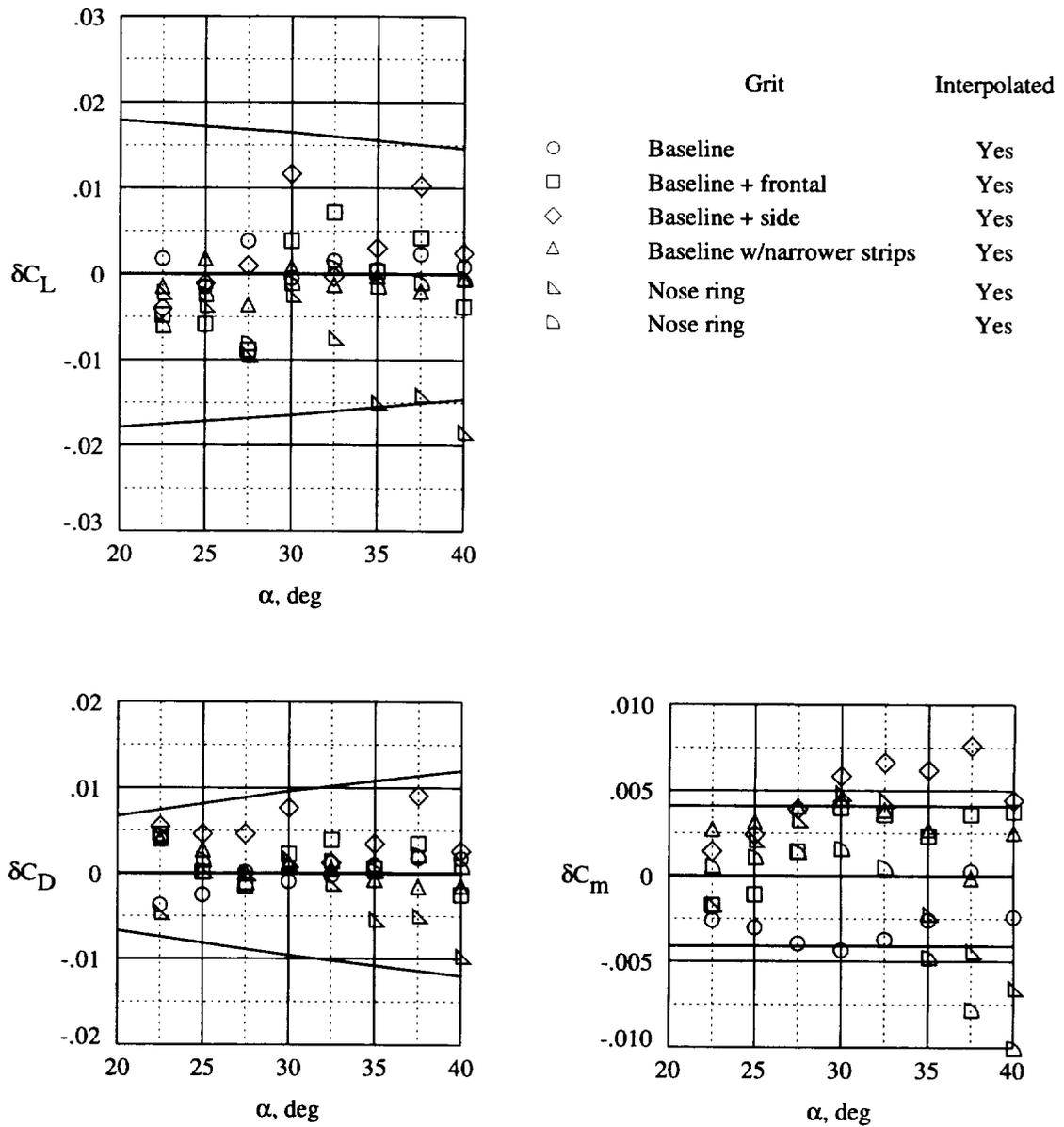
Figure 39. Differential longitudinal properties.
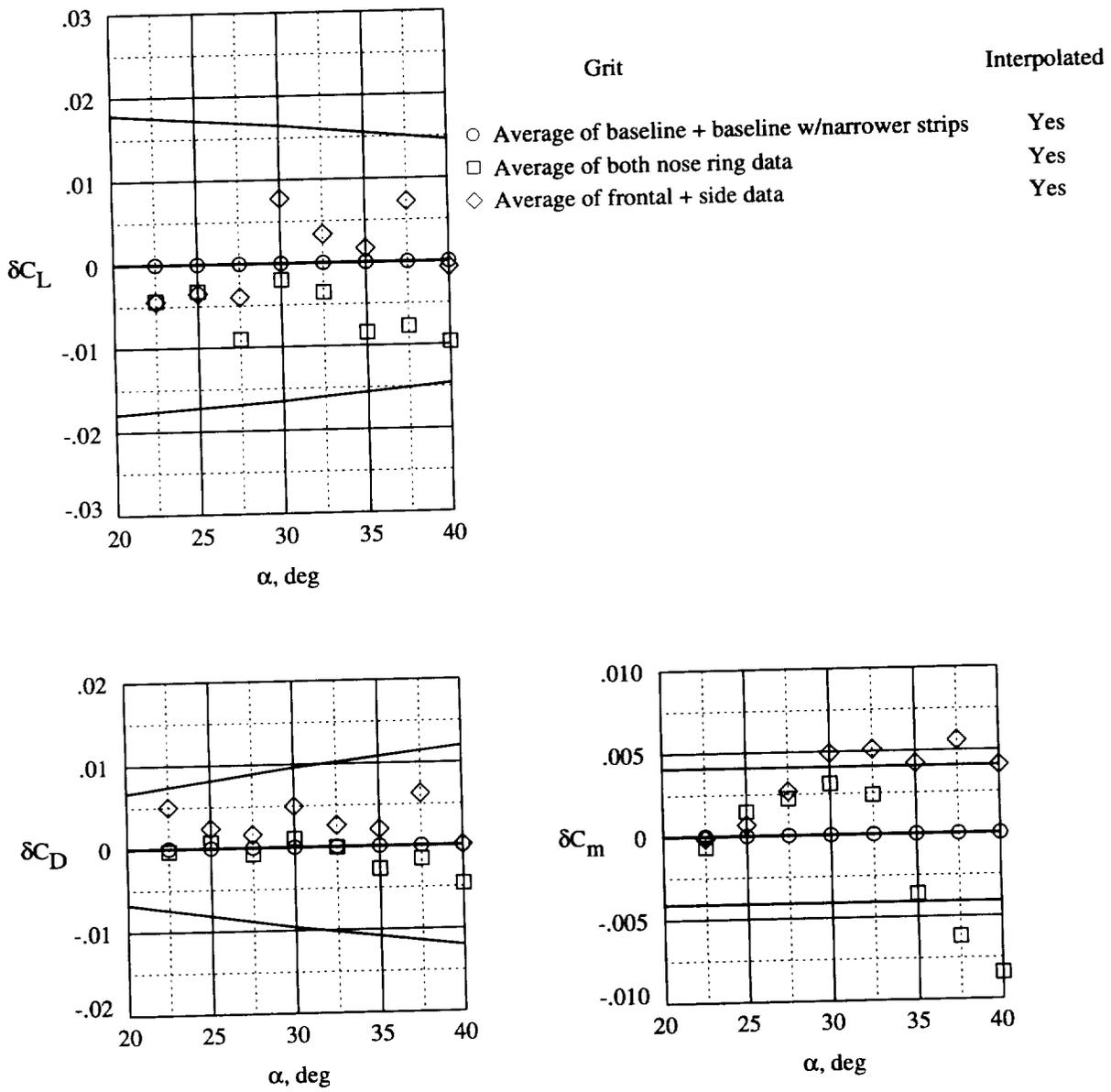
Figure 40. Averaged differential longitudinal properties.

REPORT DOCUMENTATION PAGE

Form Approved
OMB No. 07704-0188

1. AGENCY USE ONLY *(Leave blank)*	2. REPORT DATE May 1998	3. REPORT TYPE AND DATES COVERED Technical Publication

4. TITLE AND SUBTITLE

Evaluation of Gritting Strategies for High Angle of Attack Using Wind Tunnel and Flight Test Data for the F/A-18

5. FUNDING NUMBERS

WU 505-68-30-03

6. AUTHOR(S)

Robert M. Hall, Gary E. Erickson, Charles H. Fox, Jr., Daniel W. Banks, and David F. Fisher

7. PERFORMING ORGANIZATION NAME(S) AND ADDRESS(ES)

NASA Langley Research Center
Hampton, VA 23681-2199

8. PERFORMING ORGANIZATION REPORT NUMBER

L-17562

9. SPONSORING/MONITORING AGENCY NAME(S) AND ADDRESS(ES)

National Aeronautics and Space Administration
Washington, DC 20546-0001

10. SPONSORING/MONITORING AGENCY REPORT NUMBER

NASA/TP-1998-207670

11. SUPPLEMENTARY NOTES

Robert M. Hall, Gary E. Erickson, and Charles H. Fox, Jr.: Langley Research Center, Hampton, Virginia. Daniel W. Banks and David F. Fisher: Dryden Flight Research Center, Edwards, California.

12a. DISTRIBUTION/AVAILABILITY STATEMENT

Unclassified–Unlimited
Subject Category 02   Distribution: Standard
Availability: NASA CASI (301) 621-0390

12b. DISTRIBUTION CODE

13. ABSTRACT *(Maximum 200 words)*

A subsonic study of high-angle-of-attack gritting strategies was undertaken with a 0.06-scale model of the F/A-18, which was assumed to be typical of airplanes with smooth-sided forebodies. This study was conducted in the Langley 7- by 10-Foot High-Speed Tunnel and was intended to more accurately simulate flight boundary layer characteristics on the model in the wind tunnel than would be possible by using classical, low-angle-of-attack gritting on the fuselage. Six-component force and moment data were taken with an internally mounted strain-gauge balance, while pressure data were acquired by using electronically scanned pressure transducers. Data were taken at zero sideslip over an angle-of-attack range from 0° to 40° and, at selected angles of attack, over sideslip angles from −10° to 10°. Free-stream Mach number was fixed at 0.30, which resulted in a Reynolds number, based on mean aerodynamic chord, of 1.4×10^6. Pressure data measured over the forebody and leading-edge extensions are compared to similar pressure data taken by a related NASA flight research program by using a specially instrumented F/A-18, the High-Alpha Research Vehicle (HARV). Preliminary guidelines for high-angle-of-attack gritting strategies are given.

14. SUBJECT TERMS

High-angle-of-attack gritting; F/A-18; Experimental data

15. NUMBER OF PAGES

124

16. PRICE CODE

A06

17. SECURITY CLASSIFICATION OF REPORT Unclassified	18. SECURITY CLASSIFICATION OF THIS PAGE Unclassified	19. SECURITY CLASSIFICATION OF ABSTRACT Unclassified	20. LIMITATION OF ABSTRACT

NSN 7540-01-280-5500

Standard Form 298 (Rev. 2-89)
Prescribed by ANSI Std. Z39-18
298-102